PORE ENVIRONMENT ENGINEERING STUDIES IN METAL-ORGANIC FRAMEWORKS

A Dissertation

by

CHRISTINA T. LOLLAR

Submitted to the Office of Graduate and Professional Studies of
Texas A&M University
in partial fulfillment of the requirements for the degree of

DOCTOR OF PHILOSOPHY

Chair of Committee,	Hong-Cai Zhou
Committee Members,	Marcetta Darensbourg
	Michael Nippe
	Jodie Lutkenhaus
Head of Department,	Simon North

August 2020

Major Subject: Chemistry

ABSTRACT

The research detailed herein focuses on pore engineering within metal-organic frameworks. Pore size, shape, and chemical properties are key determinants to potential applicability and as such, methods that enable targeted acquisition of these properties warrant thorough exploration. The selection of tetratopic ligands in these studies serve to provide an extra modicum of stability that serves to minimize any structural integrity concerns when evaluating results. Additionally, the efforts in each project rely on the utilization of the post-synthetic modification toolbox. Post-synthetic modifications are valuable methods for tuning pre-existing metal-organic framework structures under milder conditions than those required by solvothermal synthesis - the most common technique for synthesizing these materials.

Initially, a foundation is established in which metal-organic frameworks are defined, and their properties discussed. A brief overview of the most common characterization techniques for MOFs is presented to allow for a more critical discussion of the subsequent findings. This is then concluded with a concise summary of current and proposed applications for metal-organic frameworks.

Conditions for post-synthetic linker insertions are explored through the installation of secondary linkers into the open sites of a Zr-based metal-organic framework's pores. It is discovered that seemingly trivial differences in linker size and shape may result in noteworthy thermodynamic barriers to insertion and that the success or failure of linker insertion into flexible metal-organic frameworks is indeed controllable through reasonable adjustments to temperatures of insertion.

Next, iron-based metal-organic frameworks with minor differences in linker symmetry are constructed, resulting in intriguing differences in pore size and ligand conformation. In order to make these unique structures more practical, post synthetic metal exchange from iron to chromium was utilized in order to strengthen the structure.

Following this, the pores of an iron-based metal-organic framework are loaded with urea, thiourea, and commercial fertilizers in order to interrogate their utility as slow-release fertilizers. Successful internalization is verified via powder xray diffraction and thermogravimetric analysis.

Finally, a synopsis of the discussed research on pore engineering in metal-organic frameworks well as an opinion on the future directions and outlook of these and related materials is provided.

DEDICATION

To Manuel Jorge Enriquez, my Papa, my brave hero who let me mow the lawn right next to him with my toy mower and to Sharon Kay Enriquez, my Mimi, whose heart and curious mind inspire me each and every day. Thank you both for teaching me courage - Mimi for helping me defeat the clown in Super Bomberman and Papa for helping me tackle the big slide before kindergarten. You both have done so much to prime me for success and though I'll certainly fail every now and again, I'll always strive to make you proud.

ACKNOWLEDGEMENTS

Dr. Jiandong Pang deserves more thanks than I could possibly give. Thank you for your friendship, your patience, and for guiding me through the weird world of MOF synthesis, MOF characterization, and weaving a story from results. I could not have grown so much without your assistance.

I am grateful to Dr. Hong-Cai Zhou for his guidance, his optimism, and for believing in me especially as my own confidence wanes. Thank you to my lab mates past and present – you have all become family to me – including the jubilation and the small annoyances we gift each other. For their emotional, intellectual, and experimental aid I would like to express my gratitude particularly towards Gregory Day, Elizabeth Ann Joseph, Jialuo (Carol) Li, Hannah Drake, Dr. Peng Zhang, Kunyu Wang, Zhifeng (Sean) Xiao, and Zac Perry. Thank you to Carol for SEM/TEM; to Gregory Day and Hannah Drake for collaboration in developing the 'marsbox' project; to Zhifeng (Sean) Xiao for advice in solving SCXRD structures; and to Kunyu Wang for humoring some of my unfinished projects with simulation data.

To my committee: Dr. Marcetta Darensbourg, Dr. Michael Nippe, and Dr. Jodie Lutkenhaus. I'm adding this section in after I've passed my defense so that you didn't think I was simply saying these things so you'd pass me. I selected each of you for my committee because you all had some virtue or ethic that I could look up to. I would like to thank you all for pushing me out of complacency. My prelim was a low moment but from it I learned how to hold myself accountable for my own mistakes rather than blaming

circumstances. This may have been my greatest personal triumph in grad school, and I want to thank you all for your instruction and guidance.

For my sanity I need to thank my fiancé Anish Patel. It's as if the universe knew I would need you to survive and thrive. I'm eternally grateful to the family-in-law I've gained who shower and drown me in love. Gita (mummy), Girish (daddy), Vijita, and Suchita Patel and Amit Bijlani – your acceptance, advice, and fun spirit are invaluable and I'm so fortunate that you are all now forced into my life.

Thank you to Ancestry.com and John McElwee (if only all strangers were like you) for helping me to find my biological father. In the process I have again gained a new family! Conrad, Seneca, Jasmine, Jacob, Isabelle, and Daniel: I love you!

I also would like to thank my core family. MyKayla, you've grown up into such a compassionate, responsible young lady and I'm so proud of you. Your heart is enormous, and I'm enlivened watching you bloom every day. You're going to help so many people. You stink still though. Mimi and papa, you will forever be my reason for everything I do and every choice I make. I'm so eager for all the fun we can have now that my PhD journey is finished (when the pandemic is over of course).

CONTRIBUTORS AND FUNDING SOURCES

Contributors

This work was supervised by a dissertation committee consisting of Professor Hong-Cai "Joe" Zhou (Advisor), Professor Marcetta Darensbourg of the Department of Chemistry, Professor Michael Nippe of the Department of Chemistry, and Professor Jodie Lutkenhaus of the Department of Chemical Engineering.

The nitrogen adsorption data and the SCXRD data in Chapter 2 were collected and solved with the assistance of Dr. Jiandong Pang and were published in 2019. In Chapter 3, methane adsorption data and topology images were provided by Dr. Jiandong Pang. Dr. Pang also assisted with solving of crystal structures. Jialuo (Carol) Li collected SEM images and EDS mapping. Dr. Jin-sheng Qin helped to prepare preformed iron clusters. The CO_2 isotherm in chapter 4 was collected by Gregory Day. Concept development and discussions involved Gregory Day, Hannah Drake, Eric Imhoff, and Dylan Richards.

All other work conducted for the dissertation was completed by the student independently.

Funding Sources

This material is based upon work supported by the National Science Foundation Graduate Research Fellowship under Grant No. DGE: 1252521 and the Welch Foundation (A-0030). Additionally, this work was supported as part of the Center for Gas Separations, an Energy Frontier Research Center funded by the U.S. Department of Energy, Office of Science, Basic Energy Sciences under Award # DE-SC0001015. This research used

resources of the Advanced Light Source, which is a DOE Office of Science User Facility under contract no. DE-AC02-05CH11231.

NOMENCLATURE

MOF	Metal-Organic Framework
BET	Brunauer-Emmett-Teller
PPN	Porous Polymer Network
POP	Porous Organic Polymer
COF	Covalent Organic Framework
ZIF	Zeolitic Imidazolate Framework
PCN	Porous Coordination Network
UiO	University of Oslo
HKUST	Hong Kong University of Science and Technology
MIL	Matérial Institut Lavoisier
DUT	Dresden University of Technology
IUPAC	International Union of Pure and Applied Chemistry
EPR	Electron Paramagnetic Resonance
SCXRD	Single-Crystal X-Ray Diffraction
PXRD	Powder X-Ray Diffraction
TGA	Thermal Gravimetric Analysis
NMR	Nuclear Magnetic Resonance
SEM	Scanning Electron Microscopy
RF	Radio Frequency
OMS	Open Metal Sites
SBU	Secondary Building Unit

PSM	Post-Synthetic Modification
AIM	Atomic Layer Deposition in MOFs
PSLI	Post-Synthetic Ligand Insertion
TPCB	3,3′,5,5′-tetra(phenyl-4-carboxylic acid
TPDC	2′,5′-dimethylterphenyl-4,4″-dicarboxylate
EDDB	4,4′-(ethyne-1,2-diyl)dibenzoic acid
DMF	Dimethylformamide
CCDC	Cambridge Crystallographic Data Center
IRMOF	Isoreticular Metal-Organic Framework
HSAB	Hard-Soft Acid-Base
HOMO	Highest Occupied Molecular Orbital
LUMO	Lowest Unoccupied Molecular Orbital
CBTB	4,4′,4″,4‴-(9H-carbazole-1,3,6,8-tetrayl)tetrabenzoate
EDS	Energy Dispersive X-ray Spectroscopy
NLDFT	Non-Local Density Functional Theory
SRF	Slow-Release Fertilizer
OPA-MOF	Oxalate-Phosphate-Amine Metal-Organic Framework
BDC	Benzene-1,4-dicarboxylate
EDTA	Ethylenediaminetetraacetic acid
ABTC	3,3',5,5'-azobenzenetetracarboxylic acid
LISA	Light-Induced Swing Adsorption

TABLE OF CONTENTS

Page

ABSTRACT ii

DEDICATION..... iv

ACKNOWLEDGEMENTS v

CONTRIBUTORS AND FUNDING SOURCES..... vii

NOMENCLATURE ix

TABLE OF CONTENTS xi

LIST OF FIGURES xiii

LIST OF TABLES xviii

CHAPTER I AN INTRODUCTION TO METAL-ORGANIC FRAMEWORKS.... 1

I.1 Definitions and Properties of Metal-Organic Frameworks..... 1
I.2 Characterization of Metal-Organic Frameworks..... 4
I.3 Applications of Metal-Organic Frameworks..... 10

CHAPTER II THERMODYNAMICALLY CONTROLLED LINKER

INSTALLATION INTO FLEXIBLE ZIRCONIUM MOFS..... 15

II.1 Introduction..... 15
II.2 Experimental Section..... 17
II.3 Results and Discussion..... 39

CHAPTER III NOVEL CONSEQUENCES OF LINKER SYMMETRY

REDUCTION IN IRON-BASED MOFS..... 51

III.1 Introduction..... 51
III.2 Experimental Section..... 53
III.3 Results and Discussion..... 71

CHAPTER IV LOADING STUDIES OF UREA, THIOUREA, AND

COMMERCIAL FERTILIZER INTO AN IRON-BASED MOF..... 83

IV.1 Introduction..... 83
IV.2 Experimental Section..... 88
IV.3 Results and Discussion..... 96

CHAPTER V SUMMARY AND FUTURE OUTLOOK..... 101

REFERENCES..... 103

LIST OF FIGURES

		Page
Figure 1	A highlight of various components and resulting MOF structural diversity. Blue polyhedral are representative of the geometry around metal centers while red spheres represent oxygen and black spheres represent carbon. Adapted with permission from [1]. Copyright 2003 Springer Nature……	2
Figure 2	Schematic outlining the four main methods found in this dissertation to investigate and characterize metal-organic frameworks…..…….	5
Figure 3	The structures of ligands 4,4'-dihydroxybiphenyl-3,3',5,5'-tetra(phenyl-4-carboxylic acid) (4,4'- OH-H4TPCB) and 3,3',5,5'-tetra(ethyl-4-carboxyphenyl)-4,4'-dimethoxy- biphenyl (4,4'-OMe-H4TPCB)..…….	18
Figure 4	The synthetic scheme used to obtain 3,3',5,5'-tetrabromo-4,4'-biphenol……	19
Figure 5	The synthetic scheme used to obtain 3,3',5,5'-tetra(ethyl-4-carboxyphenyl)-4,4'-dihydroxybiphenyl…….	20
Figure 6	The synthetic scheme used to obtain 4,4'-dihydroxybiphenyl-3,3',5,5'-tetra(phenyl-4-carboxylic acid) (4,4'-OH-H4TPCB)……..	21
Figure 7	The synthetic scheme used to obtain 3,3',5,5'-tetrabromo-4,4'-dimethoxy-1,1'-biphenyl……..……	22
Figure 8	The synthetic scheme used to obtain 3,3',5,5'-tetra(ethyl-4-carboxyphenyl)-4,4'-dimethoxy-biphenyl……	23
Figure 9	The synthetic scheme used to obtain 4,4'-dimethoxybiphenyl-3,3',5,5'-tetra(phenyl-4-carboxylic acid) (4,4'-OMe-H4TPCB)……	24
Figure 10	The structures of ligands 4,4'-dihydroxybiphenyl-3,3',5,5'-tetra(phenyl-4-carboxylic acid (TPDC) and 4,4'-dimethoxybiphenyl-3,3',5,5'-tetra(phenyl-4-carboxylic acid) (EDDB)……..…	25
Figure 11	Powder x-ray diffraction comparison of (a) dry, unmodified PCN-606-OH, activated PCN-606-OH-EDDB, and the simulated pattern of PCN-606-OH-EDDB (b) dry, unmodified PCN-606-OH, activated PCN-606-OH-TPDC, and the simulated pattern of PCN-606-OH-TPDC, (c) dry, unmodified PCN-606-OH, activated PCN-606-OMe-EDDB, and the simulated pattern of PCN-606-OMe-EDDB, and (d)	

dry, unmodified PCN-606-OMe, activated PCN-606-OMe-TPDC, and the simulated pattern of PCN-606-OMe-TPDC. Adapted with permission from [2]. Copyright 2019 American Chemical Society…… 35

Figure 12 Partial 1H NMR spectrum of PCN-606-OH-TPDC after digestion (top left) and PCN-606-OMe-TPDC after digestion (top right) with relevant peaks labeled. Full 1H NMR spectrum of PCN-606-OMe-TPDC after digestion (bottom left) and PCN-606-OH-EDDB after digestion (bottom right) with impurities labeled……. 36

Figure 13 Partial ^{1}H NMR spectrum of PCN-606-OH-EDDB after digestion (top left) and PCN-606-OMe-EDDB after digestion (top right) with relevant peaks labeled. Full ^{1}H NMR spectrum of PCN-606-OH-EDDB after digestion (bottom left) and PCN-606-OMe-EDDB after digestion (bottom right) with impurities labeled……..…… 37

Figure 14 N_2 sorption isotherms of (left) PCN-606-OH, PCN-606-OH-TPDC, and PCN-606-OH-EDDB, and (right) PCN-606-OMe, PCN-606-OMe-TPDC, and PCN-606-OMe-EDDB. Adapted with permission from [2]. Copyright 2019 American Chemical Society…… 39

Figure 15 Structure and topology of (a) the tetratopic carboxylate structural ligand and (b) the 8-connected Zr_6 cluster that form the parent MOF, PCN-606-R. (c) The structure and topological reduction of PCN-606-R. The structures of PCN-606-R with the differences in height along the pore in question highlighted (d) before and (e) after partial desolvation…….. 40

Figure 16 Chemical structures of (a) the primary structural ligands in PCN-606-OH (left) and PCN-606-OMe (right), (b) the secondary ligands EDDB and TPDC, and (c) PCN-606-R with axes labeled where the “a” directions corresponds to the *a*-axis, or the axis of insertion, (d) post-synthetic incorporation percentages of the primary and secondary linkers compared, and (e) a stacked column chart comparing the percent change in the *a* (green), *b* (blue), and *c* (yellow) axes lengths after ligand installation into the parent framework. Adapted with permission from [2]. Copyright 2019 American Chemical Society……... 43

Figure 17 Schematic representation of the difference in installation temperature required for the successful incorporation of EDDB and TPDC…….. 44

Figure 18 N_2 adsorption isotherms for PCN-606-R, PCN-606-R-EDDB, and PCN-606-R-EDDB where R is −OH or −OMe……... 47

Figure 19 Thermogravimetric analysis of PCN-606-OH, PCN-606-OH-TPDC (left), PCN-606-OMe, and PCN-606-OMe- TPDC (right)…….. 49

Figure 20 Synthesis of 4,4'-diamino-biphenyl-3,3',5,5'-tetra(phenyl-4-carboxylic acid (4,4’-NH2-H4TPCB)…… 55

Figure 21 Synthesis of 4,4'-dimethoxybiphenyl-3,3',5,5'-tetra(phenyl-4-carboxylic acid (4,4’-OMe-H4TPCB)……. 58

Figure 22 Synthesis of 4,4'-dicyclopentyloxybiphenyl-3,3',5,5'-tetra(phenyl-4-carboxylic acid) (4,4’-OCp-H_4TPCB)……..… 61

Figure 23 Synthesis of tetraethyl 4,4',4'',4'''-(9H-carbazole-1,3,6,8-tetrayl)tetrabenzoate (H_4CBTB)……. 63

Figure 24 Images of (a) PCN-668 and (f) PCN-668-Cr. SEM images of (b) PCN-668 and (g) PCN-668-Cr. The eds mapping of PCN-668: (c) carbon, (d) iron, (e) oxygen, and PCN-668-Cr: (h) carbon, (i) chromium, (j) oxygen……..… 70

Figure 25 The crystal structure and topology of PCN-678 and PCN-668. a) The C2 symmetry, 4-connected 4,4’-OMe-TPCB4- ligand. b) The 6-connected trigonal-prismatic [Fe3O(RCOO)6] cluster. c) The Cs symmetry, 4-connected CBTB4- ligand. d) Perspective view of PCN-678 along the c axis and the (4,6)-c topology of the microporous framework. e) Perspective view of PCN-668 along the c axis and the (4,6)-c topology of the mesoporous framework. Color scheme: black, C; red, O; blue, N; light blue, Fe. For clarity, H atoms are not shown… 72

Figure 26 (a) The enantiomeric cage-like secondary building units observed in PCN-668. (b) The ideal C_s symmetry and the C_1 symmetrical CBTB4-ligand in PCN-668. Color scheme: black, C; red, O; light blue, Fe. For clarity, H atoms are not shown……...…. 75

Figure 27 Stability tests for the microporous MOF PCN-678 and mesoporous MOFs PCN-668 and PCN-668-Cr. PXRD patterns of (a) PCN-678, (c) PCN-668, and (e) PCN-668-Cr simulated, as-synthesized, and after 24 hour exposure to water, acidic solution, and basic solution. N2 sorption isotherms for (b) PCN-678, (e) PCN-668, and (f) PCN-668-Cr as-synthesized, and after 24 hour exposure to water, acidic solution, and basic solution……...…….. 76

Figure 28 Comparison of PCN-668-Fe and PCN-668-Cr. (a) Crystal structure of PCN-668-Fe; (b) crystal structure of PCN-668-Cr. (c) SEM image of PCN-668-Fe; (d) SEM image of PCN-668-Cr……..…… 79

Figure 29 High-pressure methane uptake (total and excess) isotherms of PCN-678 (a, b), PCN-668-Fe (c, d), and PCN-668-Cr (e, f)……..... 80

Figure 30 PXRD diffraction patterns of PCN-250 with attempted fertilizer loadings compared to unmodified, dry PCN-250 and crystalline urea. Loading conditions include combining ~100 mg PCN-250 with ~ 10 mg urea (* indicates ~ 20 mg urea) while (a) soaking in water for 1 hour, (b) heating in water for 1 hour, (c) heating in water or sonicating in water for 1 hour, and (d) ground then soaked in water and heated for 1 hour or ground then heated for 1 hour…….. 92

Figure 31 PXRD diffraction patterns of PCN-250 with attempted fertilizer loadings compared to unmodified, dry PCN-250 and crystalline thiourea. Loading conditions include combining ~100 mg PCN-250 with ~ 10 mg thiourea (* indicates ~ 20 mg thiourea) while (a) soaking in water or soaking in water while heating for 1 hour or (b) ground then soaked in water and heated overnight or ground then heated overnight……..…. 93

Figure 32 PXRD diffraction patterns of PCN-250 with attempted fertilizer loadings compared to unmodified, dry PCN-250 and crystalline commercial fertilizer. Loading conditions include combining ~100 mg PCN-250 with ~ 1 mL 40% commercial fertilizer (* indicates ~ 2 mL thiourea) soaking, heating, and sonicating for 10 minutes, 1 hour, or 2 hours…….…… 93

Figure 33 Thermogravimetric analysis of PCN-250 with attempted fertilizer loadings compared to unmodified, dry PCN-250 and crystalline urea. Loading conditions include combining ~100 mg PCN-250 with ~ 10 mg urea (* indicates ~ 20 mg urea) while (a) soaking in water for 1 hour, (b) heating in water for 1 hour, (c) heating in water or sonicating in water for 1 hour, and (d) ground then soaked in water and heated for 1 hour or ground then heated for 1 hour……..… 94

Figure 34 Thermogravimetric analysis of PCN-250 with attempted fertilizer loadings compared to unmodified, dry PCN-250 and crystalline thiourea. Loading conditions include combining ~100 mg PCN-250 with ~ 10 mg thiourea (* indicates ~ 20 mg thiourea) while (a) soaking in water or soaking in water while heating for 1 hour or (b) ground

then soaked in water and heated overnight or ground then heated overnight……..…… 95

Figure 35 Thermogravimetric analysis of PCN-250 with attempted fertilizer loadings compared to unmodified, dry PCN-250 and crystalline commercial fertilizer. Loading conditions include combining ~100 mg PCN-250 with ~ 1 mL 40% commercial fertilizer (* indicates ~ 2 mL thiourea) soaking, heating, and sonicating for 10 minutes, 1 hour, or 2 hours……..…… 95

Figure 36 A simplified reaction coordinate featuring PCN-250 and crystalline fertilizer guest on the left and fertilizer-loaded PCN-250 on the right. Experiments suggest that while loading is possible through simple soaking with crystalline fertilizer, loading is much more favorable when a two step process is adopted: grinding followed by heating of the two species together……..... 99

LIST OF TABLES

		Page
Table 1	Crystal data and structure refinement for PCN-606-OH and derivatives……	30
Table 2	Crystal data and structure refinement for PCN-606-OMe and derivatives…….....	32
Table 3	Linker ratios from ^{1}H NMR Spectra of digested samples (L1 = 4,4'-OH-H_4TPCB ; L2 = 4,4'-OMe-H_4TPCB)……...	37
Table 4	Crystal data and structure refinements for PCN-648 and PCN-658……	68
Table 5	Crystal data and structure refinements for PCN-678 and PCN-668……	69
Table 6	Experimental details for fertilizer loading trials into PCN-250……...	90

CHAPTER I

AN INTRODUCTION TO METAL-ORGANIC FRAMEWORKS

I.1 Definitions and Properties of Metal-Organic Frameworks

Metal−**o**rganic **f**rameworks (**MOF**s) are a diverse class of crystalline materials composed of metal-containing nodes held together by organic linkers (spacers) to yield potential voids. Though MOFs frequently draw parallels to other porous materials, excitement has amassed for these materials in particular due to the appeal of combining advantages from metal and organic parts along with additional applicability derived from their inherent porosity and significant **B**runauer-**E**mmett-**T**eller (**BET**) surface areas. Through a discerning selection of organic and inorganic components and synthetic condition adjustments, many properties such as the internal surface area, cavity size and shape, catalytic properties, thermal properties, and mechanical properties may be manipulated. A few representative examples of size, shape, and connectivity for modifiable elements are presented in **Figure 1**. Because of this high level of tunability, MOFs have been heralded as ideal platforms for various applications including gas storage, separation, catalysis, and chemical sensing.[3-7]

In order to appreciate the utility of MOFs, it is helpful to compare their properties to those of other porous materials such as zeolites, mesoporous silica, clays, activated

carbons, **p**orous **p**olymer **n**etworks (**PPN**s), otherwise known as **p**orous **o**rganic **p**olymers

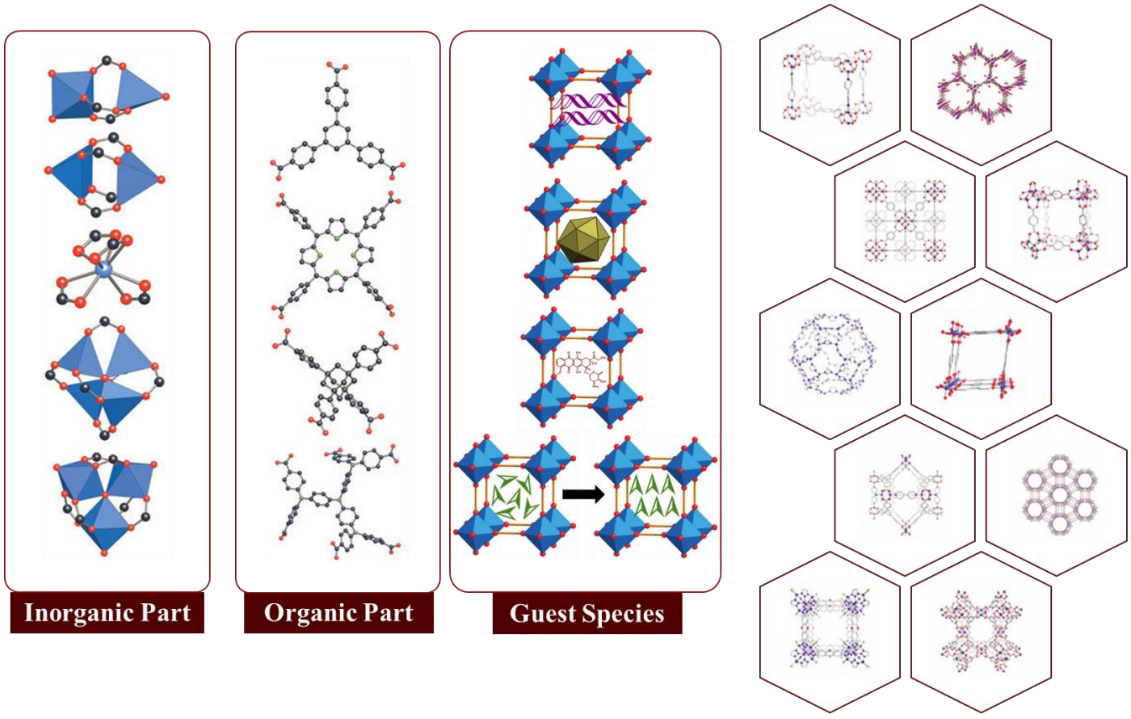

Figure 1. A highlight of various components and resulting MOF structural diversity. Blue polyhedral are representative of the geometry around metal centers while red spheres represent oxygen and black spheres represent carbon. Adapted with permission from [1]. Copyright 2003 Springer Nature.

(**POP**s), and **c**ovalent **o**rganic **f**rameworks (**COF**s).[8-11] To start, other porous materials may be challenging to confidently characterize due to their unreliable ordering. These amorphous porous materials include activated carbons, clays, some porous organic polymers, and some mesoporous silica materials. Furthermore, other porous materials possess smaller pore diameters (zeolites, activated carbons, POPs, clays, and COFs), broad or inconsistent pore size distributions (activated carbons, POPs, clays, mesoporous silica), low comparative tunability (zeolites, activated carbon, clays, and mesoporous silica), and

oftentimes much lower surface areas (zeolites, activated carbons, POPs, clays, COFs, and mesoporous silica).

Coincident with their burgeoning popularity in multiple scientific subdisciplines, MOFs have been referred to under many names and classifications.[12] MOFs have been referred to as coordination polymers, coordination networks, organic-inorganic hybrid materials, and more. Contributing to the confusion in nomenclature and classification, MOFs are named using their formula unit, structure type, or other descriptor (**MOF** for **M**etal-**O**rganic **F**ramework, **ZIF** for **Z**eolitic **I**midazole **F**ramework, **PCN** for **P**orous **C**oordination **N**etwork) but are also published under naming systems derived from their location of discovery (**U**i**O** for the **U**niversity of **O**slo, **HKUST** for the **H**ong **K**ong **U**niversity of **S**cience and **T**echnology, **MIL** for the **M**atérial **I**nstitut **L**avoisier, **DUT** for the **D**resden **U**niversity of **T**echnology) and may be numbered sequentially or by structural similarity to existing MOFs. In 2013, an IUPAC task force published their recommendations on terms for coordination compounds, net and network topologies, and topology descriptors. Although they discourages the use of some terms (particularly against using 'organic-inorganic hybrid materials' to describe MOFs), no positive recommendations were made as to the final naming of MOFs.[13]

Another type of MOF classification that is helpful to understand is generational classification which relates to how a MOF responds to guest molecule removal (often referred to as activation), commonly through solvent exchange to lower boiling point solvents, heating, and vacuum application. These guest molecules are generally solvent species which occupy the pore space within a MOF. First generation MOFs are those

which irreversibly dissociate and lose their crystallinity upon guest evacuation, insinuating that the guest molecules themselves play an essential role in keeping the structure intact. Second generation MOFs are defined as rigid frameworks with enhanced stability that maintain their structure and porosity upon activation and are essentially unaffected by guest species removal. Lastly, third generation MOFs reversibly and dynamically respond to guest molecule evacuation by alteration of their structural parameters, frequently by adjusting from open pore states to narrow pore or closed pore states. Although there has been mention in the literature of fourth generation MOFs, their definition varies and has extended to include MOFs with modifiable pore sizes through postsynthetic modifications, anisotropic MOFs, defect-containing MOFs, multivariate MOFs, and MOFs with switchable pores.[14] Therefore, the details of what defines these materials has not reached consensus and will not be discussed at length.

I.2 Characterization of Metal-Organic Frameworks

The precise characterization methods selected to analyze a MOF are often dependent upon the envisioned application. For instance, if a MOF is not intended for use in magnetic applications, **e**lectron **p**aramagnetic **r**esonance (**EPR**) spectroscopy is often omitted. Nevertheless, a handful of characterization methods have emerged as standard, including **s**ingle **c**rystal **x**-**r**ay **d**iffraction (**SCXRD**), **p**owder **x**-**r**ay **d**iffraction (**PXRD**), **t**hermogravimetric **a**nalysis (**TGA**), **n**uclear **m**agnetic **r**esonance (**NMR**), gas adsorption experiments, and **s**canning **e**lectron **m**icroscopy (**SEM**).

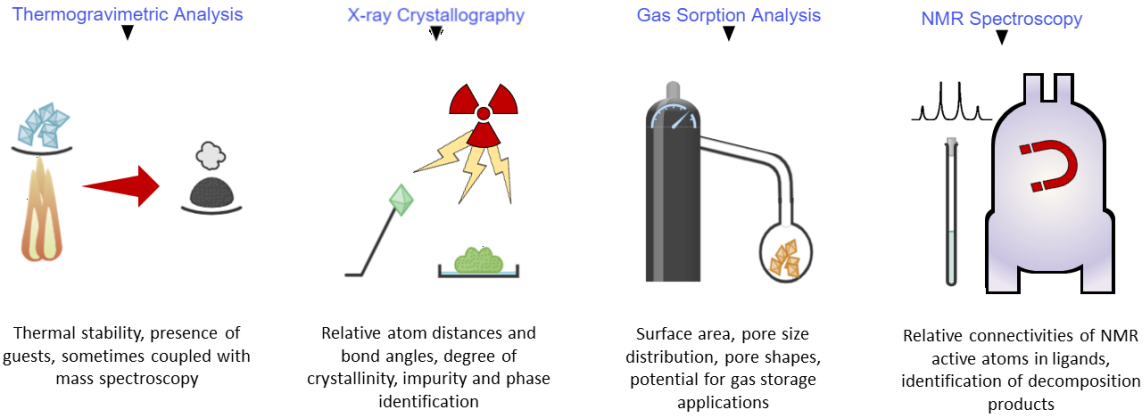

Figure 2 – Schematic outlining four common methods of investigating and characterizing metal-organic frameworks.

Gas sorption isotherms are typically acquired to describe the porosity and surface area of MOFs.[15-18] Nitrogen is the most commonly used gas to probe MOF interiors and exteriors by reason of its inertness, small size, and price. Although N_2 is sufficient for approximate pore size and surface area interpretations, the presence of a quadrupole moment in N_2 can result in the appearance of favored orientation effects in the presence of highly polar hydroxyl groups not uncommon in MOFs. In contrast, Argon gas is also frequently employed and is in fact the IUPAC-recommended probe gas for pore size and surface area analysis due to the lack of a quadrupole moment and its lower reactivity.[17] However, N_2's maintained popularity is most likely ascribed to the practicality of its much lower price point.

There are generally 6 main classifications of physisorption isotherms although the most relevant to MOF materials as described below.[18] Before gas sorption experiments, MOFs are activated to remove residual solvent molecules, often through the application of vacuum and heat though milder evacuation procedures have been developed in the case

of more sensitive frameworks. In order to overcome the difficulties associated with removing higher boiling point solvents such as DMF, a series of solvent exchanges to lower boiling point solvents are usually performed. After activation, the volume that remains is measured by means of an inert gas that is adsorbed to a negligible extent, often helium, and referred to as the dead volume or dead space for later comparison with the adsorption data. After reevacuation, a known amount of probe gas is dosed into the sample container (typically at 77 K for N_2 or 87 K for Ar). As the probe gas adsorbs onto and into the MOF, the pressure drops slightly until an equilibrium is established. This process is repeated at various pressure intervals until data for the entire desired pressure range is established. Typically, the resulting isotherm is plotted as the amount adsorbed (in units of volume, mass, or moles of adsorbate/mass of activated adsorbent) on the x-axis versus the relative equilibrium pressure (measured equilibrium pressure/saturation pressure) along the y-axis. As probe gas adsorbs to the available surfaces of the material in question, the amount adsorbed increases with increasing relative equilibrium pressure until every surface is covered by adsorbed gas. At this point, increasing relative equilibrium pressure will results in a less dramatic variation in amount adsorbed as probe molecules search for open surface. This is known as monolayer formation. If adsorption continues to asymptote, this isotherm is defined as type I and the material is likely microporous. For mesoporous materials, this leveling of the curve becomes a point of inflection whereby the amount adsorbed once again begins to rise as probe molecules fill in secondary and tertiary layers with the aid of capillary condensation until the pores are entirely filled, resulting in a type IV isotherm. For nonporous and microporous materials, completion of the monolayer is

followed by unrestricted multilayer formation and the amount adsorbed rises dependent only upon the instrument's maximum dosing pressure or the pressure limitations of the sample vessel, resulting in a type II isotherm. Desorption of probe gas materials may also be measured to further verify the presence or absence of capillary condensation, or in rarer cases, be used to observe flexibility or pore blocking phenomena.

Owing to their inherent periodic structure and crystallinity, MOF structures are most often elucidated using x-ray diffraction techniques.[15, 16] Depending upon the quality and size of the crystal available from synthesis, SCXRD may be employed to unambiguously solve the location of organic linkers and metal clusters, pore sizes and shapes, and the overall framework topology. Although disorder derived from guest solvent molecules can complicate structure solutions, this complication can be avoided through the crystallographic analysis of activated samples, sampled in which the solvent molecules have been mostly removed from a MOFs pores, or through solvent masking, with the use of SQUEEZE software, though care should be taken to assure that use of solvent masking is appropriate for the crystal in question to not obtain misleadingly low *R*-factors. In situations where, for whatever reason large, high quality crystals are unobtainable, and even with they are obtainable, PXRD techniques are exercised. PXRD techniques require crystalline powders and can easily impart information as to the identity of a MOF through comparison with past experimental or simulated patterns. PXRD may also be used to verify crystallinity and percent relative crystallinity, determine the crystallite size and size distribution, and to identify the space group, cell parameters, and structure parameters of a framework. Regrettably, PXRD is frequently observed in MOF-related publications as

the sole technique to verify MOF stability. PXRD for stability testing may be misleading and should be done for in conjunction with other characterization techniques (such as gas sorption tests to assure maintained porosity and surface area or thermogravimetric analysis described below) for reliable, rigorous data and conclusions.[19, 20]

A facile, complimentary stability-probing technique that is often run on MOFs is TGA.[15] Through gradual temperature increase applied to a known initial mass of sample in a controlled atmosphere, the decomposition temperature of the framework (often occurring roughly between 300-700 °C) as well as the presence of solvent guest molecules (often occurring near the solvents boiling point and frequently observed between 40-110 °C) may be detected and demarcated. In addition, when TGA is coupled with a mass spectrometer, the identity of the molecules producing the change in mass may be more clearly elucidated and reported.

Nuclear magnetic resonance spectroscopy is a characterization technique that employs a voltage detection coil to sense the alterations in an RF wave signal induced by precessing nuclear spins around an applied magnetic field.[21, 22] Firstly, a neutron's intrinsic nuclear spin property can be split into to two nondegenerate states upon application of a magnetic field (either parallel or antiparallel to the field). The precessional motion of the nucleus that follows is dependent upon how much of the applied magnetic field the nucleus experiences and is known as the Larmor frequency. The introduction of a RF pulse equivalent in energy to the energy difference between the two induced nuclear spin states results in a process known as resonance and at this point the spin states may flip. The magnitude of this required energy can reveal hints to a nucleus' identity as well as its

surrounding since this value is indicative of how thoroughly a nucleus is shielding from the external magnetic field by surrounding electrons. Although solution-state NMR is used widely in many fields of chemistry, application of this familiar technique to MOFs is somewhat less straightforward due to the insolubility of these materials to common NMR solvents. However, NMR techniques still play an essential role in MOF characterization, particularly when a MOF is constructed from multiple linker types. Rather than directly dissolving and performing NMR spectroscopy on the species in question, MOFs are first decomposed into their component parts. These now soluble organic components may be removed for NMR spectroscopy to confirm the ratios of incorporation as well as the maintained structure of the ligands.

When a material is treated with a source of radiation, a multitude of responses are possible. In the case of the x-ray techniques described previously, irradiation of the crystalline sample with an intense beam of x-rays results in detectable diffraction of this radiation. In contrast, irradiation of a sample with a narrow, high-energy beam of electrons can contribute energy to the nuclei-associated electrons. This energy may elicit excitation of an inner-shell electron to a higher energy state followed by subsequent relaxation and emission of energy, known as characteristic radiation. Alternatively, sufficient energy may elicit another type of outcome effectively detaching the nuclei-associated electron completely, effectively ionizing the atom. This emitted electron is known as a secondary electron. Scanning Electron Microscopy (SEM) is a materials characterization technique which relies on the detection of these secondary electrons released from a material that is bombarded with electrons.[16, 23, 24] This technique affords two-dimensional visualization of

a sample and is often used to characterize the morphology of MOF crystals attained by differing crystallization conditions or to verify the stability of MOFs by analyzing their surfaces before and after different treatments.

MOF characterization techniques are relatively comprehensive although a few gaps remain unfilled. In particular, defect analysis, particularly the detection of irregular or unordered defects, typically requires a combination of techniques in order to obtain a complete picture of the MOF's structure including the presence, frequency, location, and type (missing cluster or missing linker) of defects. For instance, occasional pore-clogging defect products may not appear to significantly affect guest diffusion or surface area in a 3D structure, depending upon the connectivity of the pores (1D channels may reveal a more noticeable difference in guest diffusion when clogged). In this case, simply analyzing the N_2 isotherms may misguide the experimenter into believing the MOF is defect-free. Alternatively, characterization through x-ray diffraction may suggest an absence of defects since x-ray diffraction is a bulk technique and the average structural diffractions may overwhelm diffraction peaks arising from defects.

I.3 Applications of Metal-Organic Frameworks

The attraction to MOFs as potential solutions to practical issues in gas storage, gas separation, drug delivery, catalysis, proton conductance, and sensing generally originates from either their high porosities, tunable pore sizes and windows, or from the flexibility in organic and inorganic component selection. Regarding gas storage, an ideal platform would bind a selected gas of interest strongly enough to improve the storage density

without requiring an impractical energy cost in the form of applied pressure but weak enough so that the gas may be released efficiently without application of excessive vacuum or heat. Generally speaking, gas adsorption in MOFs is positively correlated to the pore volume, the surface area, and the concentration of open metal sites (OMSs). Open metal sites are often considered the primary sites of adsorption and possess the highest enthalpies of adsorption. The interaction of these sites with the guests is also dependent upon the gas itself: consider the smaller size of H_2[25] compared to CH_4[26, 27] or the presence of a quadrupole moment for CO_2.[28] Additionally, the identity of the metal of the open metal sites will yield differing binding energies for each gas. In addition to open metal sites, gas molecules may be held in place by what are known as secondary adsorption sites, dominated by interactions, often Van der Waals forces, with the organic linkers and contiguous methane molecules bound to the OMSs.[29, 30] While these interactions are weaker than those found at OMSs, they can additively provide a substantial amplification of the frameworks gas uptake capacity, dependent upon temperature, and are easier to release from the framework for delivery. Gas uptake can be maximized through fine tuning of the linker lengths to offer additional space for secondary adsorption without making the pores so large that secondary adsorption sites do not benefit from interaction with the strongly held, primary adsorbed gas molecules. In a similar vein, gas separations have been explored through tuning of the frameworks toward favorable or unfavorable interactions with gas molecules. Some separations that have been demonstrated thus far include the selective separation of alkanes, the separation of tetrahydrothiophene from methane, and CO_2 from methane and C_1 to C_2 hydrocarbons. Rather than simple capture

of guest species, MOFs are also capable of being equipped with the functionality to sense guest species and to produce a detectible response following uptake.[31, 32] Generally speaking, MOF-based sensing can be divided into luminescent, interferometric, and mechanical sensors – though other means, such as conductive, solvato/vapochromatic, and sensing have also been explored.

Due to their high surface areas, the presence of physically separated metal building units, the potential for a high density of open metal sites to serve as catalytically active sites (especially after solvent removal), and tunable pore metrics, MOFs have been frequently considered for catalytic applications.[33-35] Another advantage MOF-based catalysts possess is that their pore windows may be adjusted to exclude substrates over a certain size or in particular shapes, suggesting the possibility of size-selective catalysis. As a brief purview, the presence of metal SBUs with OMSs through axial ligand removal or solvent evacuation has led to Lewis acid catalysis, cyanosilyation of aldehydes, alkane and alkene oxidation, and oxidative couplings with the metal-oxide as the catalytic site. Aside from the metal SBUS, the incorporation of Schiff-base and binaphthyl metal complexes has catalyzed olefin epoxidation and the addition of $ZnEt_2$ to aromatic aldehydes. MOFs with metalloporphyrin ligands have been shown useful in the hydroxylation of alkanes and the epoxidation of olefins. Finally, catalytically active species may be present in MOF structures as internalized guests, as is the case of polyoxometalate encapsulation to yield a catalyst for the oxidation of alkenes and hydrolysis of esters or with nanoparticle integration to produce a water splitting catalyst.

Catalysis with biological inspiration has also been accomplished using biomimetic metalloporphyrin linkers such as cytochrome P450, iron-sulfur clusters, or trapped proteins.[36, 37] Enzymes require very specific environments to preserve their folded structures and functionality and are therefore vulnerable to miniscule variations in pH, temperature, or salt concentration. Their fragility positions them as excellent candidates for guest protection. The purpose of the MOF here is to provide a barrier between a fragile payload and denaturing species to retain activity without being liberated.[38] As of late, MOFs loaded with enzymes have been employed for diverse applications such as the activation of anticancer prodrugs[39] as well as for the degradation of toxic species-contaminated wastewater. However, biological applications of MOFs extend beyond biomimetic catalysis. Biologically relevant guest uptake, protection, and release are persistently burgeoning domains of MOF applicability by virtue of their extraordinary surface areas and porosities, chemically tunable interiors, and adjustable stability and toxicity. Fascinated by what dormant advantages MOFs could afford concerning sustained or site-selective release, guest release has been the most popular of the three mentioned MOFs-as-hosts applications. Although pH and dissociation-based release mechanisms have seen the most use, MOF-drug vehicles have also been forged capable of light-,[40, 41] pressure-,[42] magnetic field-,[43] environmental hydrophobicity/hydrophilicity-,[44] and complementary DNA-induced[45] drug release mechanisms. An interesting utilization of MOFs was investigated at The University of New Mexico where it was demonstrated that a Zr-based MOF could be used for the cryopreservation and recovery of red blood cells.[46] Finally, MOFs can internalize toxic species in biological environments, thereby inhibiting

their ability to damage surrounding cells, as has been shown with uptake of intestinal salicylate by MIL-127(Fe)[47] and the efficient absorption of *p*-cresyl from human serum albumin by NU-1000.[48]

CHAPTER II

THERMODYNAMICALLY CONTROLLED LINKER INSTALLATION INTO FLEXIBLE ZIRCONIUM MOFS*

II.1 Introduction

Although microwave,[49, 50] sonochemical,[50, 51] electrochemical,[52-54] and mechanochemical[55, 56] synthesis methods are occasionally implemented, the prototypical syntheses of MOFs entail solvothermal reactions,[1] wherein a metal salt is heated in conjunction with a coordinating organic linker in a sealed container filled with a high boiling point solvent such as dimethyl formamide, diethyl formamide, or water. Typically over the course of a few days, metal, solvent, and ligand coordinate and decoordinate until they crystallize to settle into an energetic minimum. Throughout this delicate process, the time required, crystal quality, and crystal size are all dependent upon a multitude of factors including the temperature, pressure, time of reaction, pH of the solution, method of heating employed, solubility of reagents, the presence and concentration of modulating agents, concentrations of the metal salts and ligands, the oxidation states of the metals, the coordination group identity on the organic linker, and more. While this method benefits from its apparent simplicity (add reagents to a vial, place in an oven, and wait) the theoretical possibilities of MOFs are also limited by the reality of the conditions for solvothermal synthesis, which typically include high temperatures (usually over 100 °C), the use of specific solvents, and exposure to acidic or basic conditions.

---

*Adapted with permission from Lollar, C. T.; Pang, J.; Qin, J.-S.; Yuan, S.; Powell, J. A.; Zhou, H.-C. *Cryst. Growth Des.* 2019, 19, 4, 2069-2073. Copyright 2019 American Chemical Society.

In order to incorporate more delicate functionalities, post-synthetic decoration methods have been developed.[57-59] After a MOF is already assembled, the postsynthetic modification (PSM) techniques available to the framework are dependent upon its current structure. When the bonds established between organic linkers and metal SBUs are labile enough, organic ligands may be partially replaced with other ligands of the same topicity. Analogously, metal atoms forming the metal SBUs of the MOF may be exchanged with other metals postsynthetically, with the exchange percentage being dependent upon the stability of the existing cluster compared to the metal-exchanged cluster and the relative concentration of the added metal. Rather than replacement, metal cations may be installed onto the existing metal clusters in compatible cases in a technique known as cluster metalation or atomic layer deposition in MOFs (AIM). Intuitively, organic ligands may also be introduced into a MOF without significant replacement of existing ligands through a process known as postsynthetic ligand insertion (PSLI). This type of PSM will occur when the existing ligands are stable enough to resist replacement or differ in size and/or topicity from the linker being installed postsynthetically. Such installations may be more amenable after defect formation/ligand removal although some MOFs possess *de novo* unsaturated metal centers prime for ligand installation. In this chapter is described the postsynthetic linker insertion of two different linkers of slightly different length and bulk into two slightly different variants of a MOF, PCN-606-OH and PCN-606-OMe.

II.2 Experimental Section

II.2.1 Materials and Instrumentation

All reagents and solvents were commercially obtained and used as received unless otherwise specified. Single crystal x-ray diffraction (SCXRD) data were collected on a Bruker D8-Venture diffractometer equipped with a Cu sealed tube (λ=1.54178 Å) at 40 kV at Texas A&M University and on beamline 11.3.1/12.2.1 for small molecule crystallography at 6-17 kV at the Advanced Light Source at Lawrence Berkeley National Labs.[60] Powder X-ray diffraction (PXRD) was accomplished using a Bruker D8-Focus Bragg-Brentano X-ray powder diffractometer equipped with a Cu sealed tube (λ=1.54178 Å) at 40 kV and 40 mA. ^{1}H nuclear magnetic resonance (NMR) data were collected on an Inova 500 MHz spectrometer or a Mercury 300 spectrometer where chemical shifts (δ with units of ppm) were determined using a residual solvent proton as standard. N_2 adsorption-desorption isotherms were acquired at 77 K on a Micromeritics ASAP 2020 system and standardized against a dedicated P˚ sensor. Thermogravimetric analysis (TGA) was conducted using a Mettler-Toledo Analyzer.

II.2.2 Ligand Synthesis

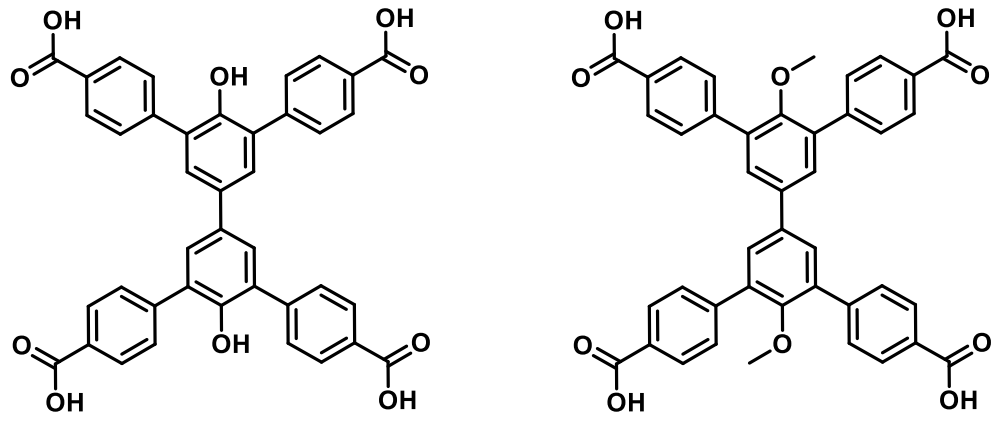

4,4'-OH-H_4TPCB **4,4'-OMe-H_4TPCB**

Figure 3. The structures of ligands 4,4'-dihydroxybiphenyl-3,3',5,5'-tetra(phenyl-4-carboxylic acid) (4,4'- OH-H4TPCB) and 3,3',5,5'-tetra(ethyl-4-carboxyphenyl)-4,4'-dimethoxy- biphenyl (4,4'-OMe-H4TPCB). Adapted with permission from [2]. Copyright 2019 American Chemical Society.

Tetracarboxylic acid ligands 4,4'-dihydroxybiphenyl-3,3',5,5'-tetra(phenyl-4-carboxylic acid) (4,4'-OH-H_4TPCB) and 3,3',5,5'-tetra(ethyl-4-carboxyphenyl)-4,4'-dimethoxy- biphenyl (4,4'-OMe-H_4TPCB) were synthesized using methods reported in a previous publication which are summarized below.[61]

II.2.2.1 Synthesis of 4,4'-OH-H4TPCB

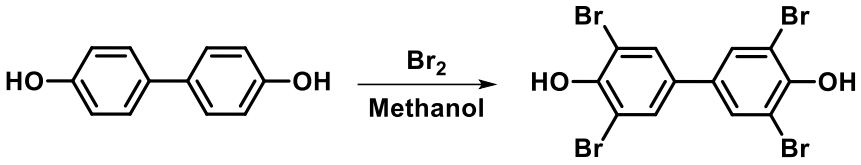

Figure 4. The synthetic scheme used to obtain 3,3',5,5'-tetrabromo-4,4'-biphenol. Adapted with permission from [2]. Copyright 2019 American Chemical Society.

II.2.2.1.1 Synthesis of 3,3',5,5'-tetrabromo-4,4'-biphenol

Bromine (13.8 mL, 268.6 mmol) was slowly added to a solution of 4,4'-biphenol (10 g, 54 mmol) in methanol (400 mL). After 1 hour of stirring, the resulting precipitate was separated by filtration and washed with saturated aqueous solutions of $NaHCO_3$ to remove unwanted acids, Na_2SO_3 to remove remaining free bromine from solution, and water as a measure to remove lingering non-organic compounds. The resulting white powder was dissolved in acetone and dried over anhydrous Na_2SO_4. Pure product was obtained by recrystallization in acetone (14.6 g, 54 %). ^{1}H NMR spectroscopy detected two peaks in a 2:1 ratio, (300 MHz, DMSO-d6) δ 7.87 (s, 4H), 10.03 (s, 2H) ppm.

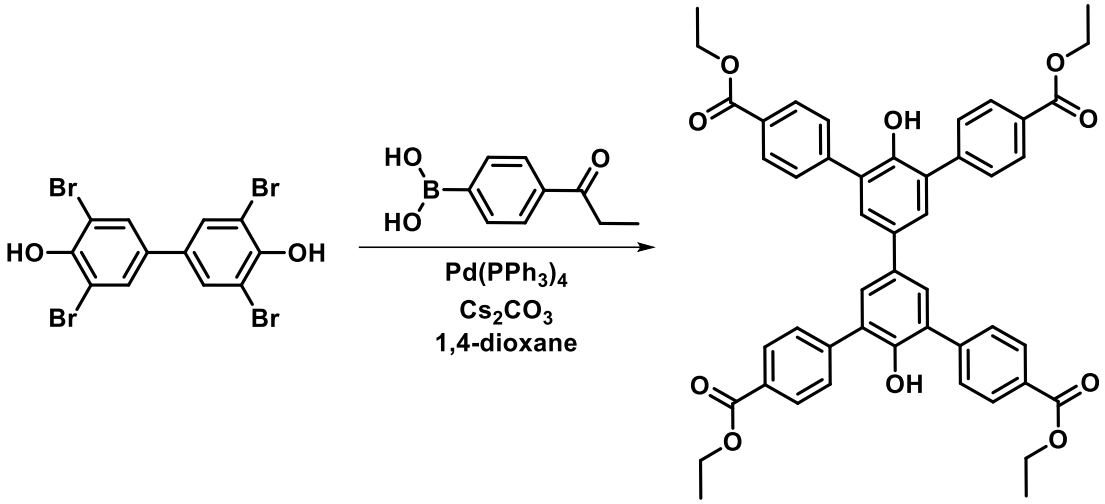

Figure 5. The synthetic scheme used to obtain 3,3',5,5'-tetra(ethyl-4-carboxyphenyl)-4,4'-dihydroxybiphenyl. Adapted with permission from [2]. Copyright 2019 American Chemical Society.

II.2.2.1.2 Synthesis of 3,3',5,5'-tetra(ethyl-4-carboxyphenyl)-4,4'-dihydroxybiphenyl

3,3',5,5'-tetrabromo-4,4'-biphenol (1.00 g, 2 mmol), (4-(ethoxycarbonyl)phenyl)-boronic acid (4.18 g, 12 mmol), Na_2CO_3 (3.80 g, 36 mmol), and $Pd(OAc)_2$ (0.05 g) solids were combined in a 250-mL Schlenk flask and vacuumed on a Schlenk line before being refilled with an atmosphere of N_2. This vacuum-refill process was repeated a total of three times before 150 mL degassed DMF/H_2O (1:1 v/v) was transferred to the system. The reaction mixture was heated to 65 °C for 72 h under a N_2 atmosphere. The reaction solution was poured into water and the pH was adjusted to about 5 by slow addition of 6M HCl, to result in precipitate formation. The obtained solid was filtered and washed with water to remove any water-soluble impurities. Further purification of the product was accomplished by flash chromatography on a silica gel column using ethyl acetate/hexane (1:4 v/v) as eluent and evaporation of the fraction containing the product. The product was

obtained as pale yellow solid (0.98 g, 68 %). ^{1}H NMR spectroscopy detected 6 peaks, (300 MHz, $CDCl_3$) δ 1.44 (t, 12H), 4.43 (q, 8H), 5.36 (s, 2H), 7.56 (s, 4H), 7.71 (d, 8H), 8.18 (d, 8H) ppm.

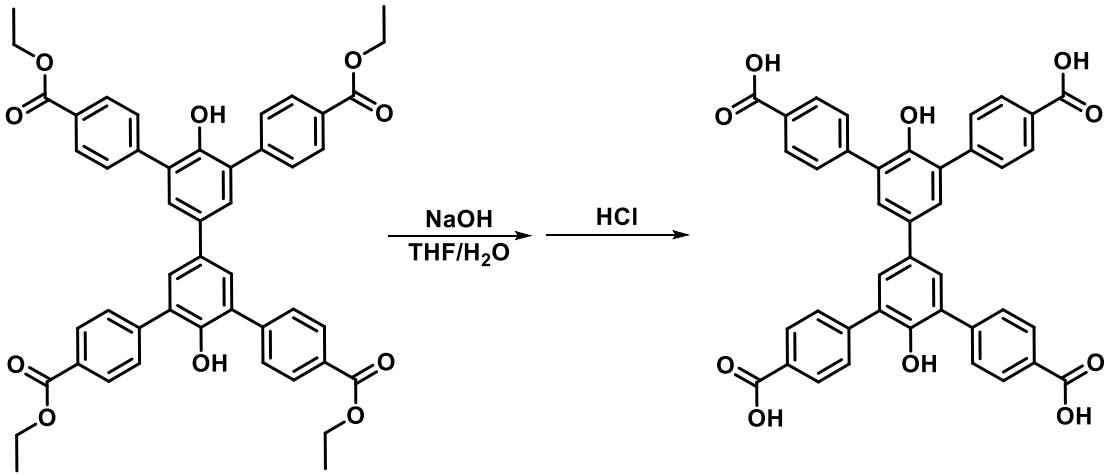

Figure 6. The synthetic scheme used to obtain 4,4'-dihydroxybiphenyl-3,3',5,5'-tetra(phenyl-4-carboxylic acid) (4,4'-OH-H4TPCB). Adapted with permission from [2]. Copyright 2019 American Chemical Society.

II.2.2.1.3 Synthesis of 4,4'-dihydroxybiphenyl-3,3',5,5'-tetra(phenyl-4-carboxylic acid) (4,4'-OH-H$_4$TPCB)

3,3',5,5'-tetra(ethyl-4-carboxyphenyl)-4,4'-dihydroxybiphenyl was dissolved in 30 mL of THF before 50 mL of 10 M NaOH aqueous solution was added. The mixture was stirred under reflux for 10 h. After this, the organic solvent was removed by rotary evaporation. The pH of the aqueous phase was adjusted to 2 by slow addition of 6 M HCl. The resulting precipitate was collected via filtration, washed with water (200 mL), and dried under vacuum to afford 4,4'-OH-H$_4$TPCB (1.9 g, 95 %). ^{1}H NMR spectroscopy

detected 5 peaks, (300 MHz, DMSO-d6) δ 7.65 (s, 4H), 7.79 (d, 8H), 8.03 (d, 8H), 8.74 (s, 2H), 12.95 (s, 4H) ppm.

II.2.2.2 Synthesis of 4,4'-OMe-H$_4$TPCB

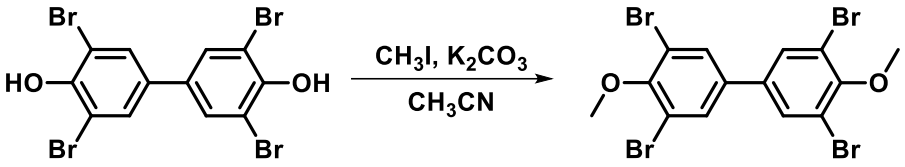

Figure 7. The synthetic scheme used to obtain 3,3',5,5'-tetrabromo-4,4'-dimethoxy-1,1'-biphenyl. Adapted with permission from [2]. Copyright 2019 American Chemical Society.

II.2.2.2.1 Synthesis of 3,3',5,5'-tetrabromo-4,4'-dimethoxy-1,1'-biphenyl

3,3',5,5'-tetrabromo-4,4'-biphenol (4.00 g, 8 mmol), CH_3I (6.80 g, 48 mmol), and K_2CO_3 (3.30 g, 24 mmol) were dissolved in CH_3CN (100 mL), heated while stirring at reflux for 18 h, and then cooled to room temperature. Solvent was removed by rotary evaporation and the resulting mixture was poured into water and extracted three times with dichloromethane. The combined organic layers were dried over anhydrous $MgSO_4$, filtered, and then solvent was again removed via rotary evaporation. After purification by column chromatography on silica gel using hexane as eluent and evaporation of the fraction containing the product, the product was obtained as white powder (2.88 g, yield: 68%). ^{1}H NMR spectroscopy yielded 2 peaks, (300 MHz, $CDCl_3$) δ 3.94 (s, 6H), 7.65 (s, 4H) ppm.

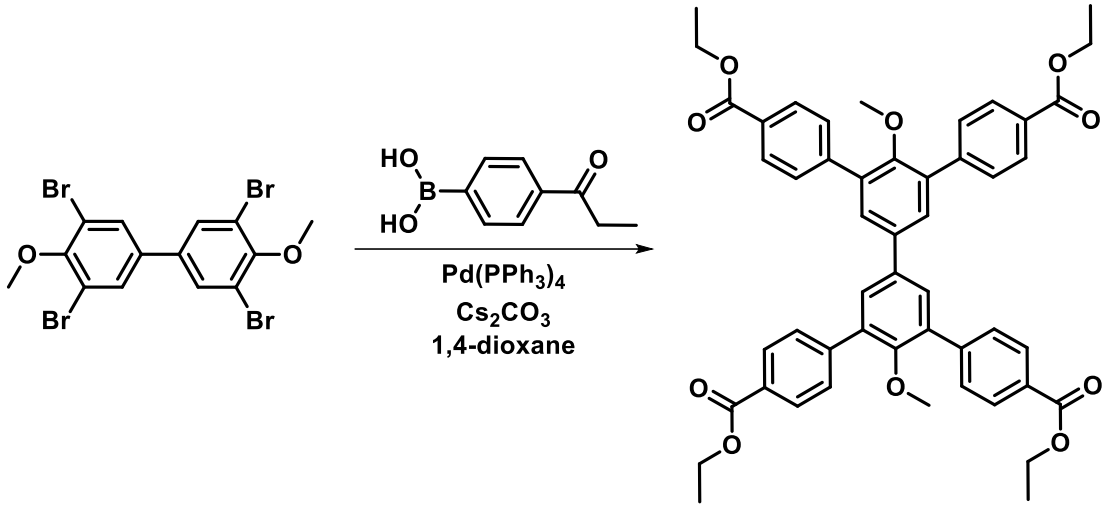

Figure 8. The synthetic scheme used to obtain 3,3',5,5'-tetra(ethyl-4-carboxyphenyl)-4,4'-dimethoxy-biphenyl. Adapted with permission from [2]. Copyright 2019 American Chemical Society.

II.2.2.2.2 Synthesis of 3,3',5,5'-tetra(ethyl-4-carboxyphenyl)-4,4'-dimethoxy-biphenyl

3,3',5,5'-tetrabromo-4,4'-dimethoxy-1,1'-biphenyl (1.06 g, 2 mmol), (4-(ethoxycarbonyl)phenyl)boronic acid (4.18 g, 12 mmol), Cs_2CO_3 (11.8 g, 36 mmol), and tetrakis(triphenylphosphine)palladium (0.092 g, 0.08 mmol) were combined, vacuumed and refilled with an atmosphere of N_2 three times before 300 mL degassed 1,4-dioxane was transferred to the system. The reaction mixture was heated to 85 °C for 72 h under a N_2 atmosphere. After the reaction mixture cooled to room temperature, the solvent was removed via rotary evaporator and water was added to the resulting mixture. Next, the product was extracted three times with dichloromethane. The combined organic layers were dried over anhydrous $MgSO_4$ and the solvent was again removed via rotary evaporator. After purification by column chromatography on silica gel using ethyl

acetate/hexane (1:5 v/v) as eluent and evaporation of the fraction containing the product, the product was obtained as pale yellow solid (1.32g, yield: 82%). ^{1}H NMR spectroscopy yielded 6 peaks, (300 MHz, $CDCl_3$): δ 1.44 (t, 12H), 3.20 (s, 6H), 4.43 (q, 8H), 7.63 (s, 4H), 7.76 (d, 8H), 8.15 (d, 8H) ppm.

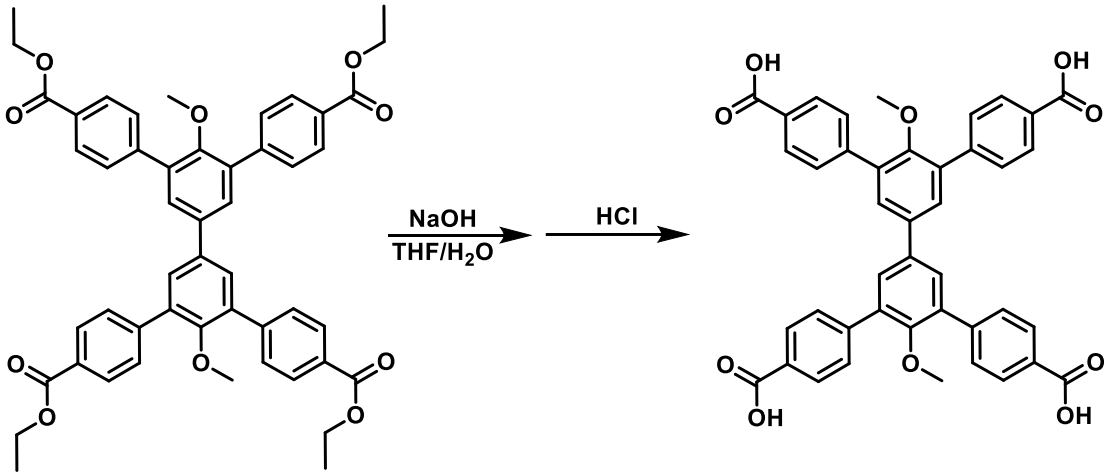

Figure 9. The synthetic scheme used to obtain 4,4'-dimethoxybiphenyl-3,3',5,5'-tetra(phenyl-4-carboxylic acid) (4,4'-OMe-H4TPCB) Adapted with permission from [2]. Copyright 2019 American Chemical Society.

II.2.2.2.3 Synthesis of 4,4'-dimethoxybiphenyl-3,3',5,5'-tetra(phenyl-4-carboxylic acid) (4,4'-OMe-H_4TPCB)

3,3',5,5'-tetra(ethyl-4-carboxyphenyl)-4,4'-dimethoxy-biphenyl (3.23 g, 4 mmol) was dissolved in 30 mL of THF, to which 50 mL of 10 M NaOH was added. The mixture was stirred under reflux for 10 h before solvent was removed by rotary evaporation. Next, 6 M HCl was slowly added until the solution pH reached 2. The resulting precipitate was collected via filtration, washed with water (200 mL), and dried under vacuum to afford

4,4’-OMe-H_4TPCB (2.64 g, 95 %). ^{1}H NMR spectroscopy yielded 5 peaks, (300 MHz, DMSO-d6) δ3.09 (s, 6H), 7.78 (s, 4), 7.80 (d, 8H), 8.03 (d, 8H), 12.98 (s, 4H) ppm.

II.2.2.3 Synthesis of TPDC and EDDB

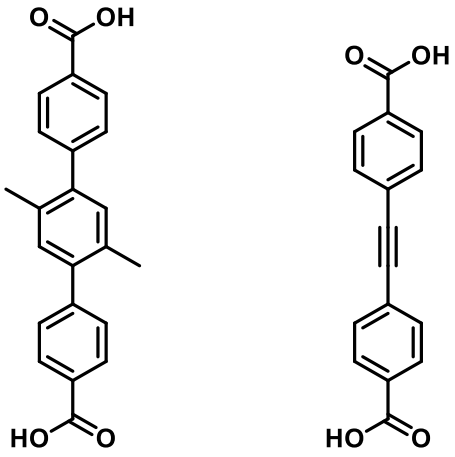

Figure 10. The structures of ligands 4,4’-dihydroxybiphenyl-3,3’,5,5’-tetra(phenyl-4-carboxylic acid (TPDC) and 4,4’-(ethyne-1,2-diyl)dibenzoic acid (EDDB). Adapted with permission from [2]. Copyright 2019 American Chemical Society.

4,4’-dihydroxybiphenyl-3,3’,5,5’-tetra(phenyl-4-carboxylic acid (TPDC)[62] and 4,4’-(ethyne-1,2-diyl)dibenzoic acid (EDDB)[63] were synthesized using previously reported methods. Key steps are described below.

II.2.2.3.1 Synthesis of 2’,5’-dimethylterphenyl-4,4”-dicarboxylic acid

To an oven dried round bottom flask was added cesium carbonate () and cesium fluoride () stirring in water. *p*-dioxane was subsequently added to the flask before

degassing by bubbling N_2 through the reaction mixture for 2 hours. Following this, 2,5-dibromo-*p*-xylene (), 4-methoxycarbonylphenylboronic acid (), and tetrakis(triphenylphosphine) palladium$^{(0)}$ () were added to the mixture. Reagents were reacted at 120 °C for 2 days under a nitrogen atmosphere. Once finished, the vessel was cooled to room temperature and the product was extracted 3 times with dichloromethane and washed 3 times with water. The product was dried over Na_2SO_4, solvent was removed by rotary evaporation, and then purified using silica gel column chromatography with dichloromethane/ethyl acetate (1/1) as eluent to produce a white powder. The purified product was then dissolved in a tetrahydrofuran/methanol mixture () stirring before potassium hydroxide () was added. This solution was heated to 90 °C refluxing for 1 day. The vessel was allowed to cool to room temperature before being filtered. The collected solid was washed twice with tetrahydrofuran. The solid was then dissolved in THF spiked with TFA and reacted for 2 hours to yield a white powder.

II.2.2.3.2 Synthesis of 4,4'-(ethyne-1,2-diyl)dibenzoic acid

Initially, methyl 4-iodobenzoate (), 1% bis(triphenylphosphine)palladium (II) chloride (), and CuI () were dissolved in dry tetrahydrofuran and triethylamine under nitrogen. Trimethylsilylacetylene () was added and the reaction was let to stir at room temperature overnight. The mixture was concentrated by rotary evaporation before being washed 3 times with ethyl acetate and reconcentrated. This product was stirred in methanol () with potassium carbonate () for 2 hours before being concentrated by rotary evaporation. To the product was added HCl () before being extracted 3 times with dichloromethane,

dried over sodium sulfate, and reconcentrated. Combination of this product with methyl 4-iodobenzoate (), bis(triphenylphosphine)palladium (II) chloride, and CuI in a mixture of tetrahydrofuran () and triethylamine () under a N_2 atmosphere for 24 hours yielded the crude diester precursor, which was then washed with chloroform, filtered, and recrystallized from toluene. Lastly, conversion of the ester to the carboxylic acid was accomplished through refluxing in ethanol with sodium hydroxide () for 24 hours. After reacting, the product was concentrated by rotary evaporation before being dissolved in water and acidified to a pH of about 1 with dropwise addition of concentrated HCl. The solid was then collected via filtration, washed three times with water, and oven-dried overnight.

II.2.3 MOF Synthesis

PCN-606-OH and PCN-606-OMe were synthesized using previously reported methods that are summarized below:[61]

II.2.3.1 PCN-606-OH

$ZrCl_4$ (~20.0 mg), 4,4'-dihydroxybiphenyl-3,3',5,5'-tetra(phenyl-4-carboxylic acid (~11.0 mg), benzoic acid (521.0 mg), and DMF (2 mL) were combined into a 4 mL Pyrex vial before being heated to 120 °C for 3 days. After this, the vessel was allowed to cool to room temperature and washed three times with fresh DMF to yield yellow crystals.

II.2.3.2 PCN-606-OMe

$ZrCl_4$ (~20.0 mg), 4,4'-dimethoxybiphenyl-3,3',5,5'-tetra(phenyl-4-carboxylic acid) (~13.0 mg), benzoic acid (610.0 mg), and DMF (2 mL) were combined into a 4 mL Pyrex vial before being heated to 120 °C for 3 days. After this, the vessel was allowed to cool to room temperature and washed three times with fresh DMF to yield colorless crystals.

II.2.3.3 PCN-606-OH-EDDB

Crystals of PCN-606-OH (about 10 mg) were soaked in a solution of 10 mg 4,4'-(ethyne-1,2-diyl)dibenzoic acid (EDDB) dissolved in 3 mL DMF. The solution was placed in an 80 °C oven for 72 hours. After removing the sample from the oven and allowing the vessel to room to room temperature, the solvent was removed and replaced with fresh DMF 3 times.

II.2.3.4 PCN-606-OH-TPDC

Crystals of PCN-606-OH (about 10 mg) were soaked in a solution of 10 mg 2',5'-dimethylterphenyl-4,4"-dicarboxylate (TPDC) dissolved in 3 mL DMF. The solution was placed in a 120 °C oven for 72 hours. After removing the sample from the oven and allowing the vessel to room to room temperature, the solvent was removed and replaced with fresh DMF 3 times.

II.2.3.5 PCN-606-OMe-EDDB

Crystals of PCN-606-OMe (about 10 mg) were soaked in a solution of 10 mg 4,4'-(ethyne-1,2-diyl)dibenzoic acid (EDDB) dissolved in 3 mL DMF. The solution was placed in an 80 °C oven for 72 hours. After removing the sample from the oven and allowing the vessel to room to room temperature, the solvent was removed and replaced with fresh DMF 3 times.

II.2.3.6 PCN-606-OMe-TPDC

Crystals of PCN-606-OMe (about 10 mg) were soaked in a solution of 10 mg 2',5'-dimethylterphenyl-4,4"-dicarboxylate (TPDC) dissolved in 3 mL DMF. The solution was placed in a 120 °C oven for 72 hours. After removing the sample from the oven and allowing the vessel to room to room temperature, the solvent was removed and replaced with fresh DMF 3 times.

II.2.4 Single Crystal X-ray Diffraction

Single crystals before and after linker installation were transferred to oil and mounted onto a loop for single crystal X-ray data collection. For the partially desolvated MOFs, the single crystals were taken from the mother liquid and mounted into a loop standing in a stream of nitrogen slowly warming up from 100 K to room temperature and then cooling down to 100 K. Diffraction was measured on Bruker Smart Apex diffractometers equipped with a Cu-Kα sealed-tube X-ray source (λ = 1.54178 Å, graphite monochromated) and low temperature device (100 K). The data frames were recorded

using the program APEX3 and processed using the program SAINT routine within APEX3. The data were corrected for absorption and beam corrections based on the multi-scan technique as implemented in SADABS. The structures were solved by direct methods using SHELXS and refined by full-matrix least-squares on F2 using SHELXL software. All non-hydrogen atoms were refined with anisotropic displacement parameters. The hydrogen atoms on the aromatic rings were located at geometrically calculated positions and refined by riding. Since free solvent molecules in MOFs are highly disordered, attempts to locate and refine the solvent peaks were unsuccessful. The diffuse electron densities resulting from these solvent molecules were removed using the SQUEEZE routine of PLATON; structures were then refined again using the data generated. Crystal data are summarized below. CCDC 1569633, 1569634, 159636, 1854071, and 1875211-1875213 contain the relevant supplementary crystallographic data. This data may be obtained free of charge from The Cambridge Crystallographic Data Centre.

Table 1. Crystal data and structure refinement for PCN-606-OH and derivatives. Adapted with permission from [2]. Copyright 2019 American Chemical Society.

	PCN-606-OH	PCN-606-OH-EDDB	PCN-606-OH-TPDC
CCDC	1569633	1875212	1854071
Formula	$C_{10}H_{5.50}O_{4.50}Zr_{0.75}$	$C_{16}H_{10.17}O_6Zr$	$C_{50}H_{24}O_{18}Zr_3$
Formula weight	266.06	389.63	1186.35
Temperature/K	100.15	100.15	100.15

Table 1. Continued

	PCN-606-OH	PCN-606-OH-EDDB	PCN-606-OH-TPDC
Radiation	CuKα (λ = 1.54184)	CuKα (λ = 1.54184)	CuKα (λ = 1.54184)
Shape/Color	Block/Yellow	Block/Red	Block/Yellow
Crystal system	Orthorhombic	Orthorhombic	Orthorhombic
Space group	*Cmmm*	*Cmmm*	*Cmmm*
a/Å	18.7781(10)	21.4840(6)	23.1272(7)
b/Å	35.2745(8)	34.5678(9)	34.0179(10)
c/Å	16.0212(3)	15.4290(4)	15.0243(5)
α/°	90	90	90
β/°	90	90	90
γ/°	90	90	90
Volume/Å^3	10612.3(6)	11458.4(5)	11820.2(6)
Z	16	12	4
ρ_{calc}g/cm^3	0.666	0.678	0.667
μ/mm^{-1}	2.638	2.468	2.399
F(000)	2104	2330	2352
Completeness	99%	99%	99%
Reflections collected	3025	4526	5730
Unique reflections	2409	3929	4780
Parameters	149	158	163

Table 1. Continued

	PCN-606-OH	PCN-606-OH-EDDB	PCN-606-OH-TPDC
R_{int}	0.0281	0.0420	0.0375
R_1 [I>2σ(I)]	0.0452	0.0676	0.0745
wR_2 [I>2σ(I)]	0.1283	0.2052	0.2034
R_1 (all data)	0.0507	0.0733	0.0829
wR_2 (all data)	0.1308	0.2126	0.2164
Goodness-of-fit on F^2	1.002	1.075	1.087

Table 2. Crystal data and structure refinement for PCN-606-OMe and derivatives. Adapted with permission from [2]. Copyright 2019 American Chemical Society.

	PCN-606-OMe	PCN-606-OMe-dry	PCN-606-OMe-EDDB	PCN-606-OMe-TPDC
CCDC	1569634	159636	1875211	1875213
Formula	$C_{21}H_{13}O_9Zr_{1.50}$	$C_{168}H_{104}O_{72}Zr_{12}$	$C_{12.12}H_{8.75}O_{4.50}Zr_{0.75}$	$C_{53}H_{42}O_{18}Zr_3$
Formula weight	546.14	4369.15	294.86	1240.52
Temperature/K	100.15	100.15	100.15	100.15
Radiation	CuKα (λ = 1.54184)	CuKα (λ = 1.54184)	CuKα (λ = 1.54184)	CuKα (λ = 1.54184)
Shape/Color	Block/Colorless	Block/Colorless	Block/Colorless	Block/Colorless
Crystal system	Orthorhombic	Orthorhombic	Orthorhombic	Orthorhombic
Space group	*Pbam*	*Cmmm*	*Cmmm*	*Cmmm*

Table 2. Continued

	PCN-606-OMe	PCN-606-OMe-dry	PCN-606-OMe-EDDB	PCN-606-OMe-TPDC
a/Å	35.2146(9)	17.007(9)	21.5531(6)	23.2506(5)
b/Å	19.7752(16)	36.117(19)	34.7752(9)	34.1088(7)
c/Å	15.7268(6)	16.155(8)	15.2170(4)	14.8706(3)
α/°	90	90	90	90
β/°	90	90	90	90
γ/°	90	90	90	90
Volume/Å^3	10951.8(10)	9923(9)	11405.3(5)	11793.1(4)
Z	8	1	16	4
ρ_{calc} / (g/cm^3)	0.662	0.731	0.687	0.699
μ/mm^{-1}	2.563	0.342	2.481	2.414
F(000)	2168	2168	2360	2496
Completeness	90%	99%	97%	99%
Reflections collected	5380	1492	5126	6280
Unique reflections	3082	936	3457	5810
Parameters	248	101	111	199
R_{int}	0.0453	0.2704	0.1109	0.0216
R_1 [I>2σ(I)]	0.0586	0.0933	0.0712	0.0372
wR_2 [I>2σ(I)]	0.1754	0.2153	0.1982	0.1131

Table 2. Continued

	PCN-606-OMe	PCN-606-OMe-dry	PCN-606-OMe-EDDB	PCN-606-OMe-TPDC
R_1 (all data)	0.0790	0.1421	0.0960	0.0385
wR_2 (all data)	0.1869	0.2384	0.2106	0.1148
Goodness-of-fit on F^2	0.946	1.009	1.062	1.063

II.2.5 Powder X-ray Diffraction

MOF crystalline powders were collected after synthesis and prepared for activation by slow solvent exchange from DMF to a lower boiling point solvent (acetone). Solvent was separated from the MOF crystals and activation was done under vacuum and heating at 80 ^{o}C for 5 h. At this point, PXRD data were collected on linker-inserted analogues and compared to unmodified PCN-606-OH and PCN-606-OMe samples as well as simulated PXRD patterns.

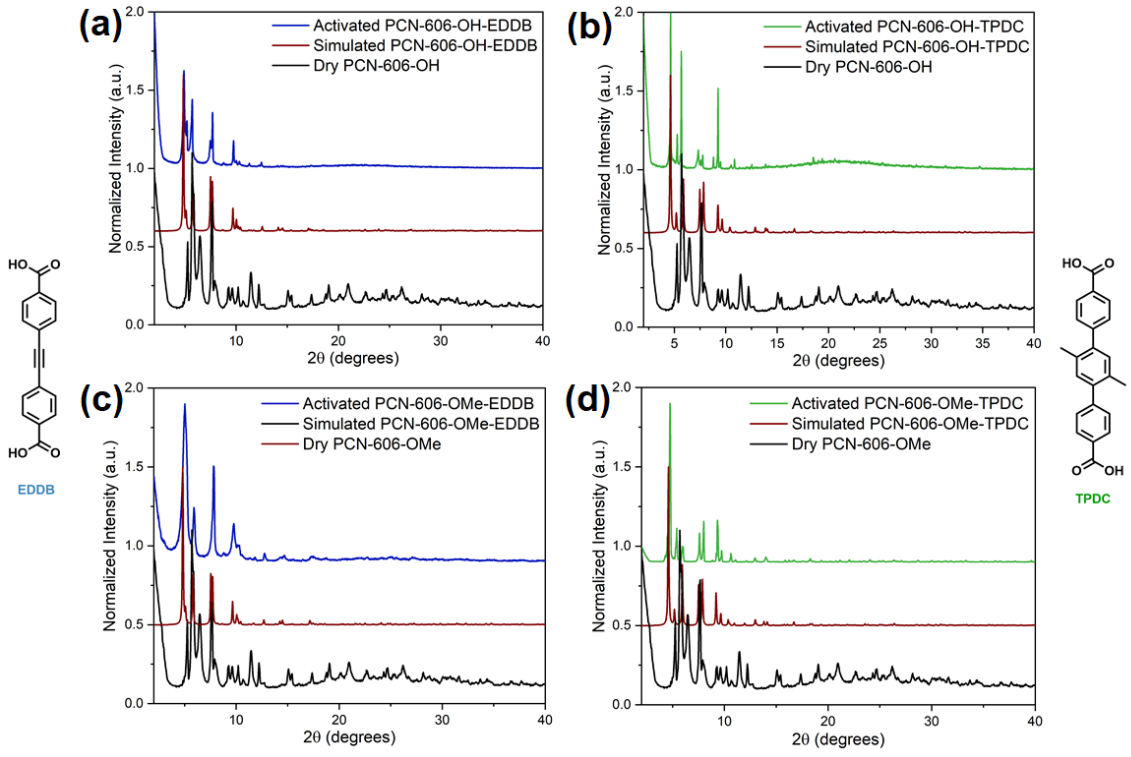

Figure 11. Powder x-ray diffraction comparison of (a) dry, unmodified PCN-606-OH, activated PCN-606-OH-EDDB, and the simulated pattern of PCN-606-OH-EDDB (b) dry, unmodified PCN-606-OH, activated PCN-606-OH-TPDC, and the simulated pattern of PCN-606-OH-TPDC, (c) dry, unmodified PCN-606-OH, activated PCN-606-OMe-EDDB, and the simulated pattern of PCN-606-OMe-EDDB, and (d) dry, unmodified PCN-606-OMe, activated PCN-606-OMe-TPDC, and the simulated pattern of PCN-606-OMe-TPDC. Adapted with permission from [2]. Copyright 2019 American Chemical Society.

II.2.6 ^{1}H NMR Spectroscopy

Before ^{1}H NMR spectroscopy, 0.5 mL of DMSO-d_6 was added to about 5 mg of activated MOF sample followed by a drop of D_2SO_4. Samples were sonicated for 7 minutes and centrifuged. The supernatant was extracted for NMR. The resulting spectra and calculated linker ratios for the digested MOF samples appear below.

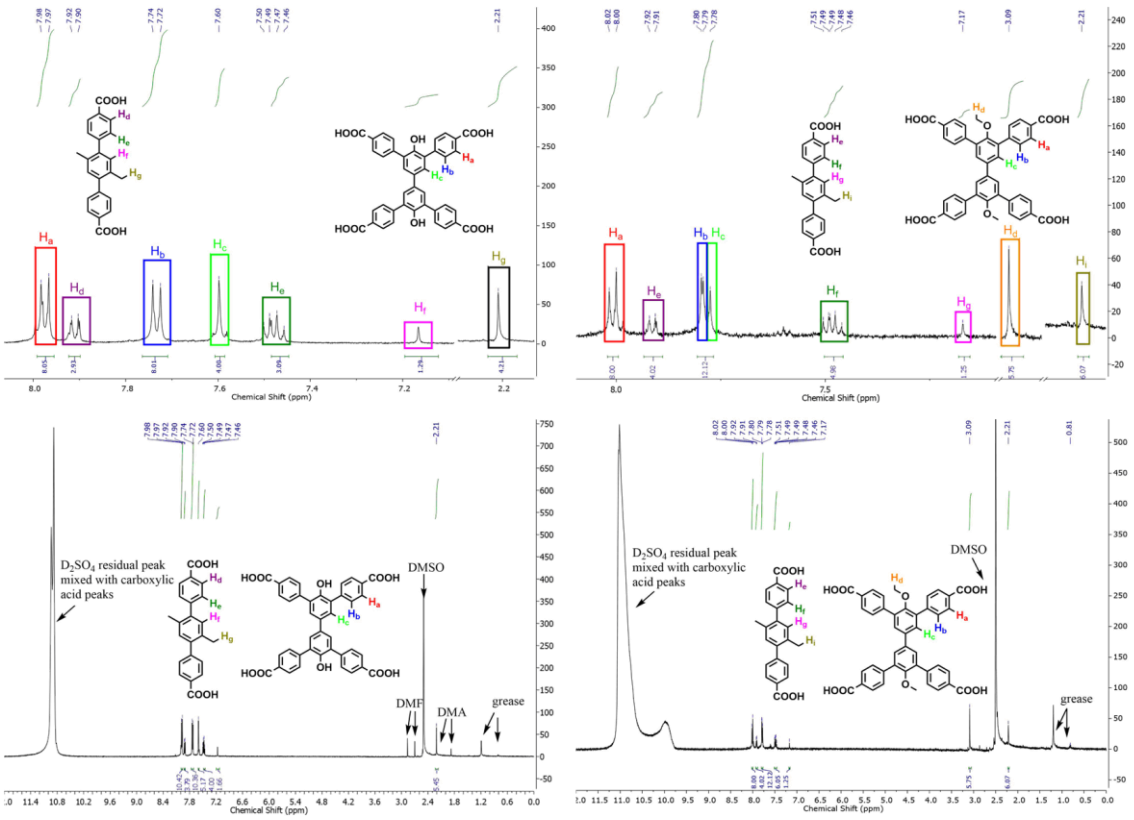

Figure 12. Partial ^{1}H NMR spectrum of PCN-606-OH-TPDC after digestion (top left) and PCN-606-OMe-TPDC after digestion (top right) with relevant peaks labeled. Full ^{1}H NMR spectrum of PCN-606-OMe-TPDC after digestion (bottom left) and PCN-606-OH-EDDB after digestion (bottom right) with impurities labeled. Adapted with permission from [2]. Copyright 2019 American Chemical Society.

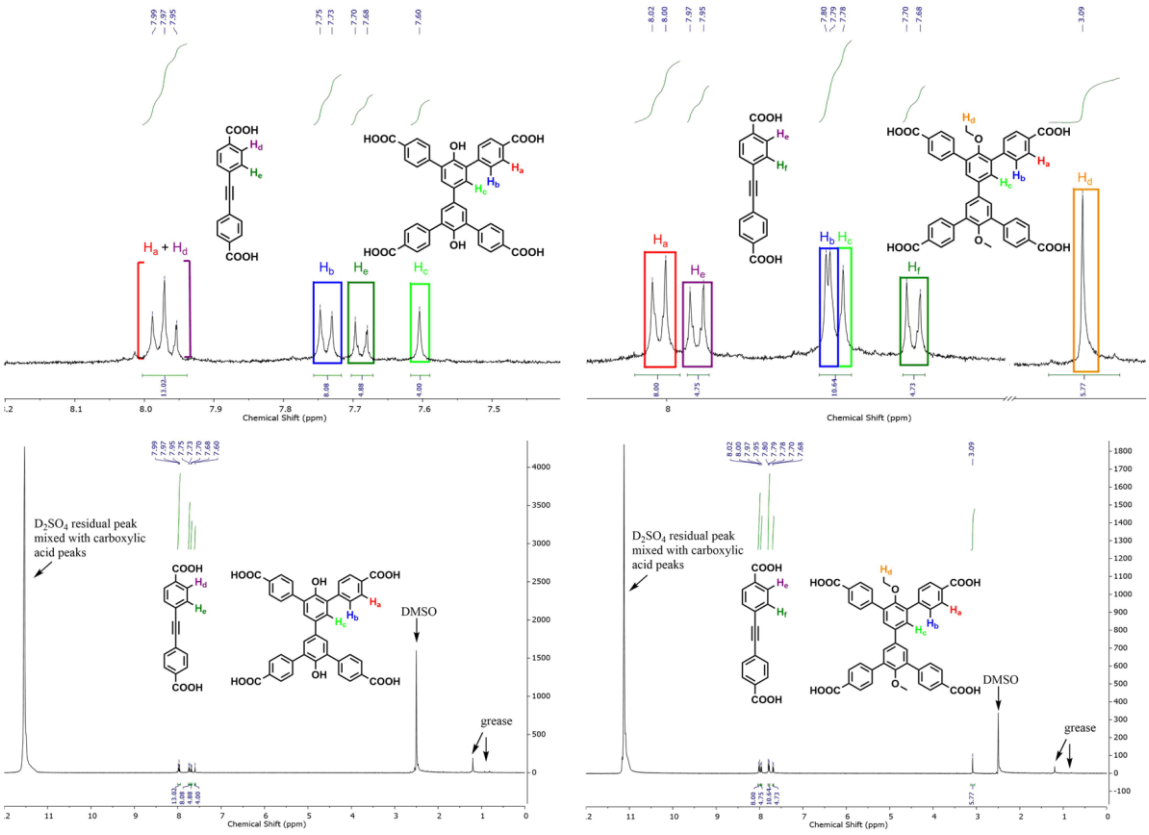

Figure 13. Partial ^{1}H NMR spectrum of PCN-606-OH-EDDB after digestion (top left) and PCN-606-OMe-EDDB after digestion (top right) with relevant peaks labeled. Full ^{1}H NMR spectrum of PCN-606-OH-EDDB after digestion (bottom left) and PCN-606-OMe-EDDB after digestion (bottom right) with impurities labeled. Adapted with permission from [2]. Copyright 2019 American Chemical Society.

Table 3. Linker ratios from 1H NMR Spectra of digested samples (L1 = 4,4'-OH-H4TPCB ; L2 = 4,4'-OMe-H4TPCB). Adapted with permission from 60. Copyright 2019 American Chemical Society.

MOF	Linker Ratio
PCN-606-OH	L1: 100%
PCN-606-OMe	L2: 100%
PCN-606-OH-EDDB	L1 : EDDB = 1.00 : 1.22 (~55.0 % EDDB)

Table 3. Continued

MOF	Linker Ratio
PCN-606-OMe-EDDB	L2 : EDDB = 1.00 : 1.23 = (~55.2 % EDDB)
PCN-606-OH-TPDC	L1 : TPDC = 1.37 : 1.00 = (~42.2 % TPDC)
PCN-606-OH-TPDC (One Pot)	L1 : TPDC = 1.00 : 1.10 = (~52.3% TPDC)
PCN-606-OMe-TPDC	L2 : TPDC = 1.00 : 1.05 (~ 51.2 % TPDC)
PCN-606-OMe-TPDC (One Pot)	L2 : TPDC = 1.00 : 1.29 (~56.3% TPDC)

II.2.7 N_2 Sorption Isotherms

N_2 adsorption measurements were performed using a Micromeritics ASAP 2020 surface area and pore size analyzer. Before measurements, as-synthesized samples were washed with DMF several times. Next, the crystals were carefully decanted and washed with acetone several times. Samples were activated under vacuum at 80 °C for 5 h. Low-pressure N_2 adsorption isotherms were measured at 77 K in a liquid nitrogen bath and are displayed below.

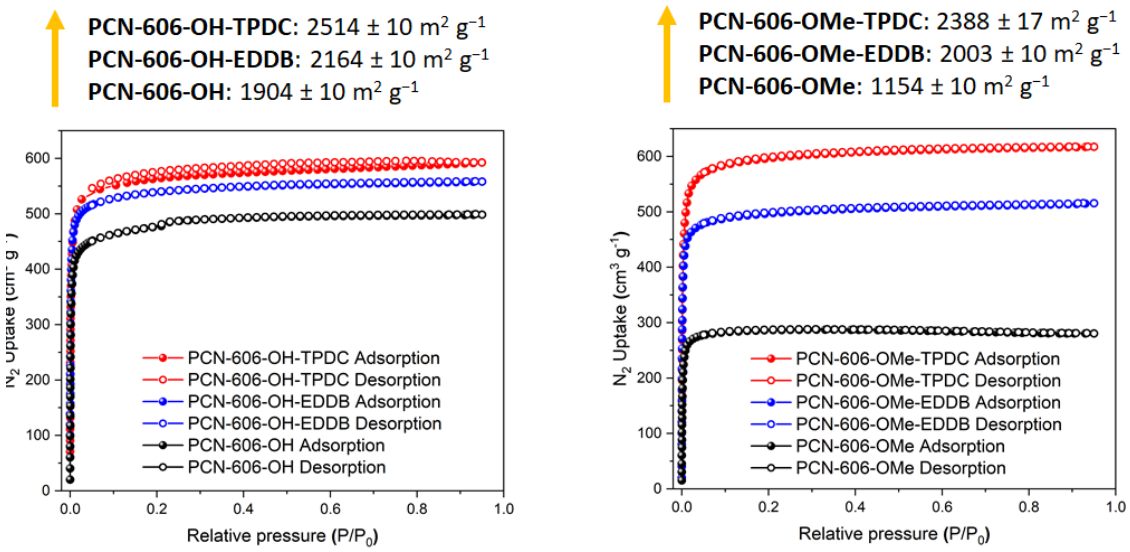

Figure 14. N_2 sorption isotherms of (left) PCN-606-OH, PCN-606-OH-TPDC, and PCN-606-OH-EDDB, and (right) PCN-606-OMe, PCN-606-OMe-TPDC, and PCN-606-OMe-EDDB. Adapted with permission from [2]. Copyright 2019 American Chemical Society.

II.3 Results and Discussion

PCN-606 is a stable MOF that crystallizes in the orthorhombic *Cmmm* space group producing a 4,8-c **scu**-net topology with a topological point symbol of $\{4^{16}.6^{12}\}\{4^4.6^2\}_2$ (**Figure 15**). PCN-606 was selected as a platform for linker insertion for three key reasons. First, PCN-606 possesses tetratopic linkers and 8-connected Zr_6 clusters (**Figure 15**) with exceptional stability, variable connectivity, and open metal sites for postsynthetic linker installation (**Figure 15**). Secondly, PCN-606's **scu**-type topology is often likened to and referred to as a 'wine-rack lattice'.[64] Wine-rack lattices feature X-shaped nodes and rhombohedral pores and are distinguished by their low-energy 'breathing' modes, whereby the framework can reversibly expand and contract by deviation in the ligand-metal-ligand angles away from 90°. This degree of flexibility is predicted to aid in the

accommodation of different linker lengths. Lastly, the synthetic tuning for and flexibility of PCN-606 had already been established experimentally by previous work through measurement along the channel pores before and after partial desolvation (**Figures 15d and 15e**)[65] and by subsequent use as a bromine nanocontainer for room temperature brominations, whereby MOFs with more accommodating, flexible pores showed higher

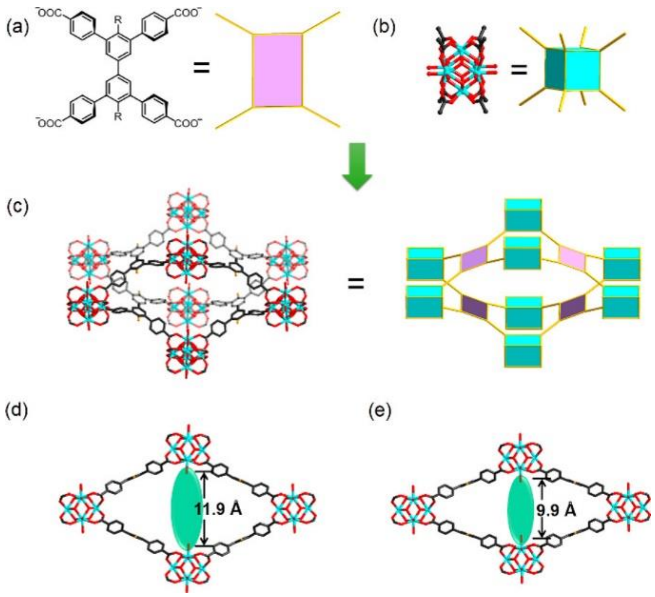

Figure 15. Structure and topology of (a) the tetratopic carboxylate structural ligand and (b) the 8-connected Zr_6 cluster that form the parent MOF, PCN-606-R. (c) The structure and topological reduction of PCN-606-R. The structures of PCN-606-R with the differences in height along the pore in question highlighted (d) before and (e) after partial desolvation. Adapted with permission from [2]. Copyright 2019 American Chemical Society.

bromine uptake.[61] In particular, PCN-606-OH and PCN-606-OMe were selected, whose $Zr_6(\mu_3\text{-}O)_4(\mu_3\text{-}OH)_4(H_2O)_4(OH)_4$ nodes are connected by 4,4′OH-H4TPCB (4,4′-dihydroxybiphenyl-3,3′,5,5′-tetra(phenyl-4-carboxylic acid)) or 4,4′-OMeH4TPCB (4,4′-

dimethoxybiphenyl-3,3′,5,5′-tetra(phenyl-4- carboxylic acid)), respectively. The relative energies of these ligands when forced in a PCN-606-type (**scu**) framework, a PCN-605-type (**flu**) framework, or a PCN-608-type framework (**csq**) were calculated and indicate a preference for the **scu** and **csq** topologies over the **flu** topology. This is because the functional groups in the 4- and 4′-positions of these ligands should encourage the adoption of the **scu**- or **csq**-net topology by maintaining the coplanarity of the inner biphenyl rings in a D_{2h} symmetry, likely as a consequence of conjugative effects. Although targeting of the (4,8)-connected **scu**-net structure in particular is possible through synthetic condition tuning, a small amount of **flu**-type, PCN-605 impurity could not be avoided. These **scu**-net MOFs contain large one-dimensional pore channels, a high degree of flexibility, and 8-connected metal nodes with inherent defects prime for the postsynthetic installation of additional linkers. The overall appearance of **scu** topology MOFs are often likened to wine-rack lattices and postsynthetic linker insertion into these lattices produces frameworks often referred to as 'reinforced' wine-rack type structures.[66, 67] To obtain 'reinforced' wine-racks, two ligands, H_2EDDB (4,4′-(ethyne-1,2-diyl)dibenzoic acid) and Me_2TPDC (2′,5′-dimethylterphenyl-4,4″-dicarboxylate) whose structures are shown in **Figure 16**, were selected for insertion into PCN-606-OH and PCN-606-OMe (a general structure of PCN-606-R, where R = -OH or -OMe, with crystallographic axes labeled can also be found in **Figure 16**). The OH^-/H_2O ligands on the metal clusters of these MOFs may be removed relatively easily to allow for postsynthetic integration of the linear dicarboxylate ligands since ditopic ligands are more easily held in a framework than monotopic solvent "ligands". Generally, higher connectivities correspond to higher

stabilities, since the probability a ligand can disconnect and separate from the framework decreases as the number of coordination bond breaking events that need to occur simultaneously increases.[7, 68] We have recently reported on PCN-606-OH with postsynthetically installed TPDC linkers (PCN-606-OH-TPDC) in a separate pursuit of developing more complex, multicomponent MOFs. Me_2TPDC is longer and bulkier than H_2EDDB, and so insertion of this ligand postsynthetically into either framework seemed less promising. For this reason, postsynthetic insertion using H_2EDDB was attempted first. It was found that H_2EDDB can be successfully incorporated into PCN-606-OH and PCN-606-OMe by soaking either of the PCN-606-R derivatives in a solution of excess ligand in DMF at 80 °C to form new MOFs which were termed PCN-606-OH-EDDB and PCN-606-OMe-EDDB. However, when the same procedural variables were applied using the Me_2TPDC ligand, linker insertion proved unsuccessful. This was attributed to the aforementioned difference in length and bulkiness. Cognizant of the flexibility of these wine-rack frameworks in combination with the fact that Me_2TPDC only barely dwarfed H_2EDDB, the question arose as to whether this insertion could be accomplished by further provoking PCN-606-R's inherent pliability. Interestingly, raising the temperature of the linker insertion process appears to push the flexibility boundaries of the framework. Indeed, it was found that when the parent MOF was soaked in a solution of excess Me_2TPDC ligand in DMF at 120 °C, the PCN-606-OH-TPDC and PCN-606-OMe-TPDC structures successfully formed (**Figure 17**). It is worthwhile to note that we were also able

to obtain PCN-606-R-TPDC through a one-pot synthesis containing both TPCB and TPDC with ligand insertion ratios comparable to post synthetic insertion (**Table 3**); how-

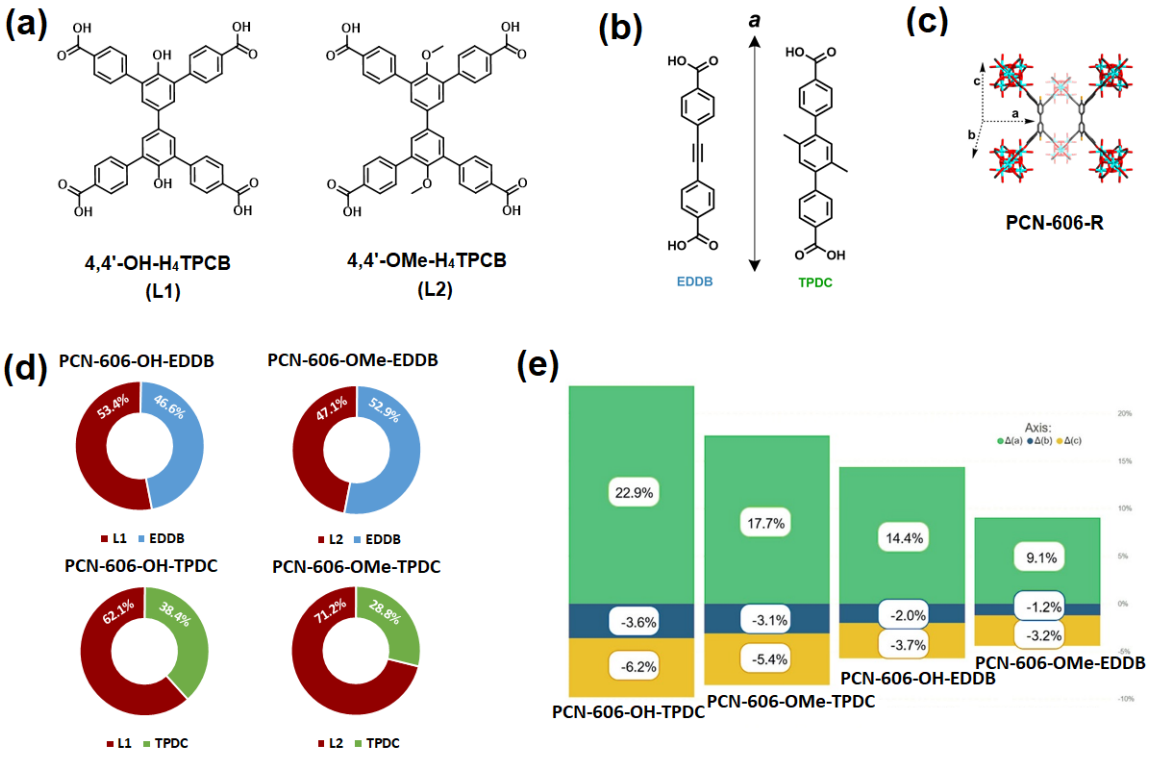

Figure 16. Chemical structures of (a) the primary structural ligands in PCN-606-OH (left) and PCN-606-OMe (right), (b) the secondary ligands EDDB and TPDC, and (c) PCN-606-R with axes labeled where the "a" directions corresponds to the *a*-axis, or the axis of insertion, (d) post-synthetic incorporation percentages of the primary and secondary linkers compared, and (e) a stacked column chart comparing the percent change in the *a* (green), *b* (blue), and *c* (yellow) axes lengths after ligand installation into the parent framework. Adapted with permission from [2]. Copyright 2019 American Chemical Society.

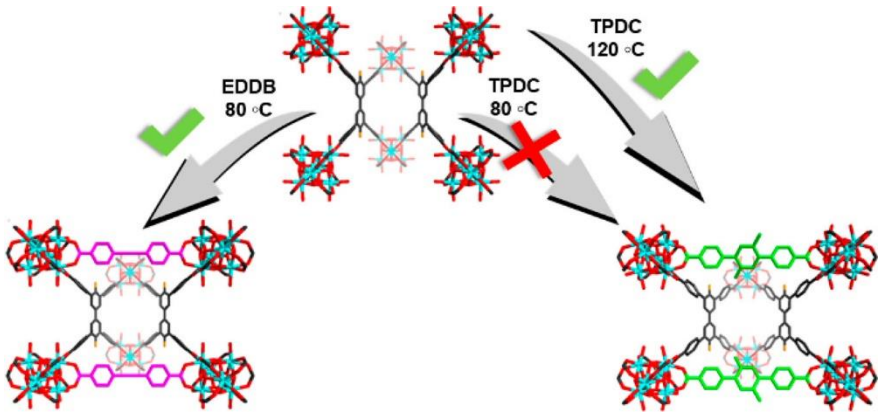

Figure 17. Schematic representation of the difference in installation temperature required for the successful incorporation of EDDB and TPDC. Adapted with permission from [2]. Copyright 2019 American Chemical Society.

ever, we were unable to acquire PCN-606-R-EDDB in this manner. Successful installation of the linear linkers was confirmed with ^{1}H NMR analysis of the decomposed MOF samples. Single-crystal X-ray diffraction (SCXRD) studies revealed that the newly formed MOFs were all 4,10-c nets with new topologies and a point symbol of $\{4^{16}.5^{12}.6^{16}.7\}\{4^{4}.5^{2}\}_{2}$. Although ^{1}H NMR and SCXRD confirmed the successful postsynthetic incorporation of the linear linkers, the details of this insertion were still unclear. In particular, successful postsynthetic linker installation may predominantly rely upon the MOFs' inherent flexibility and the enhancement of such upon exposure to an increase in temperature, it could be argued that the increase in temperature is transferred primarily to the linker, allowing access to more diverse vibrational modes which facilitates entry into the MOFs' pores, or the process might require a combination of both possibilities. To uncover more information regarding the means of postsynthetic ligand introduction into PCN-606-R frameworks, it was important to verify the changes in the

frameworks themselves by noting the change in length of the axis of installation (the *a*-axis) before and after insertion. Upon incorporation of the slightly less obtrusive H_2EDDB ligand into PCN-606-OH and PCN-606-OMe, the *a*-axis expanded from an initial 18.8 Å and 19.8 Å to 21.5 Å (a difference of 2.7 Å or a 14.4% expansion) and 21.6 Å (a difference of 1.8 Å or a 9.1% expansion) to form PCN-606-OH-EDDB and PCN-606-OMe-EDDB, respectively. The resulting *a*-axis lengths for the −OH and −OMe MOFs are nearly identical since the inserted linker is the same. This may suggest that distortion in the linker is minimal or less accessible in comparison to the changes that may occur in the parent MOF, at least in regard to the final linker-inserted framework. The integration of the larger Me_2TPDC ligand in PCN-606-OH and PCN-606-OMe to form PCN-606-OH-TPDC and PCN-606-OMe-TPDC results in *a*-axis length expansions from the same initial 18.8 Å and 19.8 Å to final lengths of 23.1 Å (a difference of 4.3 Å or a 22.9% expansion) and 23.3 Å (a difference of 3.5 Å or a 17.7% expansion), respectively. Once again, the resulting *a*-axis lengths of PCN-606-OH-TPDC and PCN-606-OMe-TPDC naturally are very close. The greater *a*-axis expansion for the incorporation of the more demanding TPDC linker is likely reflected in the requirement for a higher energy input via an elevated installation temperature (120 °C as opposed to 80 °C) to help overcome the thermodynamic barrier to its formation. As the *a*-axis expands, the *b*-axis and *c*-axis can interestingly be seen slightly shrinking to compensate. Explicitly, when Me_2TPDC extends the *a*-axis of PCN-606-OH by 4.3 Å (22.9%), the *b*-axis reduces by 1.3 Å (3.6%) and the *c*-axis reduces by 1.0 Å (6.2%). When the same ligand is inserted into PCN-606-OMe with an *a*-axis extension of 3.5 Å (17.7%), the *b*-axis shrinks by 1.1 Å (3.1%) and

the *c*-axis shrinks by 0.9 Å (5.4%). The addition of the smaller ligand, H_2EDDB, into PCN-606-OH produces a growth in the *a*-axis by 2.7 Å (14.4%) accompanied by *b*-axis and *c*-axis reductions by 0.7 Å (2.0%) and 0.6 Å (3.7%), respectively. Lastly, insertion of H_2EDDB into PCN-606-OMe increases the *a*-axis by 1.8 Å (9.1%) while concurrently decreasing the *b*-axis and *c*-axis by 0.4 Å (1.2%) and 0.5 Å (3.2%), respectively. In all cases, the *a*-axes show a larger percentage increase than the sum of the *b*- and *c*-axes decrease suggesting an overall increase in size, which will be mentioned later in terms of volume (these percent changes are displayed together for more facile comparison in **Figure 16**). Additionally, the changes in axes lengths are more dramatic in the case of PCN-606-OH-R′ than for PCN606-OMe-R' (where R′ = EDDB or TPDC). It is conceivable that the steric effects in the methoxy- derivative somewhat impede structural ligand distortion in the framework, leading to smaller changes in axis lengths. Admittedly, the smaller magnitude of axial changes is also certainly aided by the fact that PCN-606-OMe's axes lengths were already closer to those of the linker-inserted PCN-606-OMe-R'. However, this reasoning is challenged by the fact that in our previous reports, the *a*-axis of PCN-606-OH shrinks by about 22.3% while the *a*-axis of PCN-606-OMe shrinks by about 14.0% upon desolvation. In this case there was no common 'final' axis length at which to converge and so the restricted contraction is stronger evidence of a less flexible framework. Although the linkers are installed along the *a*-axis, it is also helpful to consider changes in volume in order to understand MOF flexibility. As may be predicted, unmodified PCN-606-OH and -OMe have the smallest volumes of about 10,600 $Å^3$ and 11,000 $Å^3$. Upon insertion of the smaller EDDB ligand, this volume expands by 7.97%

and 4.14%, respectively. With the addition of the bulkier TPDC ligand, volumes of each MOF expanded by 11.4% and 7.68%, respectively. These values are reasonable considering the larger size of TPDC as well as the lower flexibility of PCN-606-OMe compared with PCN-606-OH or simply the larger starting volume of PCN-606-OMe. More specific crystal data may be found in **Table 1** and **Table 2**. Aside from a crystallographic understanding of PCN-606-R's pores, the internal spaces of these MOFs were also probed before and after each ligand installation with N_2 gas as the probe molecule. Nitrogen sorption isotherms shown in **Figure 18** were

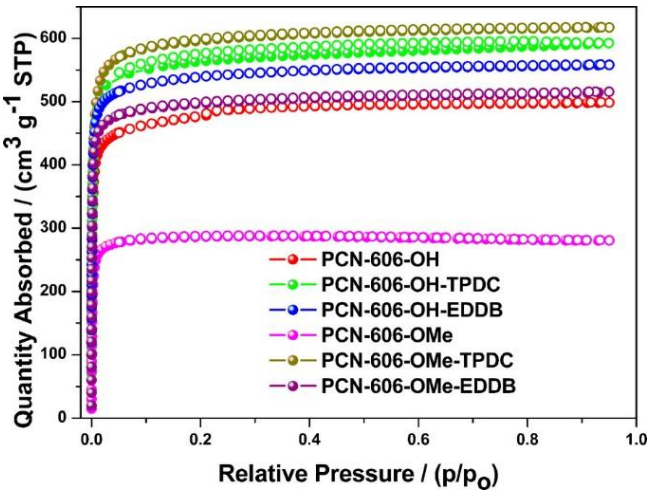

Figure 18. N_2 adsorption isotherms for PCN-606-R, PCN-606-R-EDDB, and PCN-606-R-EDDB where R is −OH or −OMe. Adapted with permission from.[2] Copyright 2019 American Chemical Society.

collected at 77 K (1 atm) and compared. In the case of both the −OH and −OMe derivatives, N_2 uptake follows the same trend as *a*-axis length and crystallographically-measured volume expansion, increasing in the order of PCN-606-R < PCN-606-R-EDDB

< PCN-606-R-TPDC. Specifically, PCN-606-OMe shows the lowest uptake at about 280 $cm^3\ g^{-1}$, followed by PCN-606-OH at about 498 $cm^3\ g^{-1}$, PCN-606-OMe-EDDB at 515 $cm^3\ g^{-1}$, PCN-606-OH-EDDB at 558 $cm^3\ g^{-1}$, PCN-606-OH-TPDC at 592 $cm^3\ g^{-1}$, and PCN-606-OMe-TPDC at 618 $cm^3\ g^{-1}$. These translate into BET surface areas of 2003 ± 10 $m^2\ g^{-1}$ for PCN-606-OMe-TPDC, 2164 ± 10 $m^2\ g^{-1}$ for PCN-606-OH-TPDC, 2514 ± 10 $m^2\ g^{-1}$ for PCN-606-OH-EDDB, and 2388 ± 17 $m^2\ g^{-1}$ for PCN-606-OMe-EDDB. It may seem intuitive that adding linkers into a MOF's pores can increase the available surface area; however, a marked disparity is observed in the amount by which PCN-606-OMe increases in surface area upon linker insertion compared to PCN-606-OH. This difference arises due to the abnormally low nitrogen uptake in unmodified PCN-606-OMe. This is likely a consequence of MOF flexibility. If PCN-606-OMe adopts a closed pore state when unmodified and solvent is evacuated, some surfaces will be inaccessible, resulting in a decreased surface area as measured by nitrogen adsorption. This closed pore state was not observable through SCXRD because SCXRD samples were not harshly activated prior to data collection, rather, they were extracted from mother liquor and placed in a stream of nitrogen not exceeding room temperature. Therefore, the SCXRD structures contained solvent molecules which disallowed transformation into the closed pore state. Linker insertion into PCN-606-OMe forces the MOF into an open pore conformation, explaining the comparatively dramatic increase in nitrogen uptake. With the data seeming to point to a difference in the thermodynamic barriers to installation for these two ligands, the thermal stability of the resulting MOFs and their parents was naturally called into question. Thermogravimetric analysis indicated the increased

stability of the MOFs after linker insertion, with a more prominent increase in thermal stability in the case of PCN-606-OMe and derivatives as compared to the less conspicuous increase in thermal stability for PCN-606-OH MOFs. The TGA data are contained in **Figure 19.**

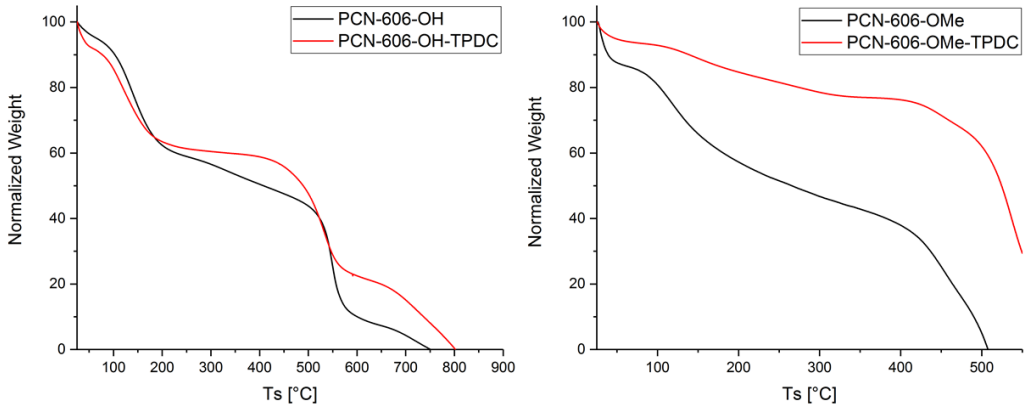

Figure 19. Thermogravimetric analysis of PCN-606-OH, PCN-606-OH-TPDC (left), PCN-606-OMe, and PCN-606-OMe- TPDC (right).

In summary, linker installation into PCN-606-R parent frameworks has yielded a collection of four MOFs, PCN-606-OH-EDDB, PCN-606-OMe-EDDB, PCN-606-OH-TPDC, and PCN-606-OMe-TPDC. The TPDC linker is bulkier and slightly longer than the EDDB linker, and so a higher temperature was necessary for successful installation. X-ray crystallography provided information on the changes in axis lengths and volume upon linker installation, providing general insight into the flexibility of the two PCN-606-R derivatives as well as the temperature-dependent flexibility of these frameworks. The reported results highlight two related points, (1) that small differences in linker size may

result in significant discrepancies in the activation energies of insertion and (2) that the size of the linkers a flexible MOF is capable of accepting may be adjusted by additional energy input in the form of heat. As of late, the number of interesting studies on pathways and conditions for MOF flexibility have been increasing. Enhancing our understanding of how to manipulate, explain, and predict flexible MOF behavior will doubtlessly enable greater control over future functional MOF structures and behaviors.

CHAPTER III

NOVEL CONSEQUENCES OF LINKER SYMMETRY REDUCTION IN IRON-BASED MOFS

III.1 Introduction

The disparities in MOFs' pore regimes, whether through size, shape, chemical properties, or a combination of these, make them appropriate for distinct applications. Size-selective separation applications are a typical example wherein pores should be large enough to allow the passage of relevant compounds yet small enough to exclude unwanted potential contaminants.[3, 69] However, some innovative works investigating selective separations from samples of mixed xenon and krypton have reversed the expected approach and taken advantage of the favorable accumulation of van der Waals interactions that occurs with larger compounds better able to reach the walls of a MOF's framework, resulting in more selective separations in larger pore diameters.[70] Additionally, rather sizeable pores are required for successful housing of larger guests such as enzymes while the combination of sizable pores and small pore windows are ideal for enzyme protection.[38, 57] More confined pore spaces are important in applications such as proton conductance in order to permit facile proton hopping without excessive congestion to impede hopping.[71]

In pursuit of access to a collection of MOFs with variable pore sizes and shapes, numerous pore-modification methods have been investigated. Although Yaghi *et al* reported an isoreticular series of MOFs (IRMOFs) with linkers of varying length, bulk,

and functionality under a similar set of solvothermal conditions,[72] the procurement of MOFs with spacious pores is typically not as straightforward as employing lengthier ligands.[7] With other factors held constant, attempting this approach with solvothermal synthesis produces MOFs inflicted with compromised stability if any MOF is obtained at all. A noticeable decrease in structural stability with an increase in linker length is commonly explained through comparing the stability of the transition state of a linker detaching itself from a metal or metal cluster. For a shorter linear ligand, the bending that would occur during decomposition would be at a more extreme angle than would be required of a longer analogue translating to a higher activation barrier for the shorter ligand.[73] The length of the organic ligand is only one factor to consider in predicting and describing the rationale behind MOF stability or instability.

The Zhou group is renowned for a focus on the design and synthesis of ultra-stable MOFs.[7, 57, 74] Labile coordination bonds between low-valence metals and carboxylate-containing organic ligands elicit chemical instability in many MOFs to water, acid, or base, dramatically limiting their further applicability and commercialization.[19, 75] According to the Pearson hard/soft acid/base (HSAB) principle,[76] ultra-stable MOFs can be targeted through the use of high-valent, hard Lewis acidic species, which are known to form more resilient bonds with carboxylate ligands. This affinity is rationalized by concepts of orbital overlap and orbital energy matching. Since the mixing of atomic orbitals to form molecular orbitals produces one orbital of energy lower than the average of the individual atomic orbitals and one orbital of energy higher than the average of the individual atomic orbitals and the degree of mixing by atomic orbitals is inversely

proportional to their difference in energy, stronger bonds are generated from the mixing of HOMOs and LUMOs with similar energies.

Previously, the Zhou group has published a study on the MOFs which result from linker symmetry reduction of a trapezoidal, tetratopic linker with 8-connected Zr_6 clusters. Application of the original C_{2h} linker generated the **scu**-type network PCN-606 described in chapter II of this dissertation. However, reduction of the linker symmetry to C_s produces a new **scu**-type network, PCN-609. The distinguishing feature of these two MOFs is the number of different pocket types in the structures. In PCN-606 there are two pocket types, one pocket resides in the *ab* crystallographic plane with a length of about 10.9 Å and a smaller pocket exists in the *bc*-plane with a length of about 8.1 Å. PCN-609 in comparison possesses three distinct open pockets, one in the *ab*-place of about 10.7 Å, one in the *bc*-plane of about 6.1 Å, and a final pocket coexisting in the *bc*-plane of about 10.3 Å. This fascinating study demonstrates how linker symmetry reduction can produce novel MOFs with new binding pockets. However, PCN-606 and PCN-609 both possess **scu**-type topologies, likely in part due to the high symmetry of the 8-connected Zr_6 clusters. It is hypothesized that more complex structures would become available if the symmetry of the metal SBU was also decreased.

III.2 Experimental Section

III.2.1 Materials and Instrumentation

All reagents and solvents used in the following synthetic studies were commercially available and used as supplied without further purification. The organic

ligands employed were synthesized through the routines described below. Single crystal X-ray diffraction experiments were carried out on Bruker D8-Venture diffractometers equipped with Cu microfocus tubes (λ = 1.54178 Å) at 40 kV at Texas A&M University and on beamline 11.3.1/12.2.1 for small molecule crystallography at 6-17 kV at the Advanced Light Source at Lawrence Berkeley National Labs.[60] Scanning Electron Microscopy (SEM) measurements were carried out on a JEOL JSM-7500F, an ultra-high-resolution field emission scanning electron microscope (FE-SEM) equipped with a high brightness conical FE gun and a low aberration conical objective lens. ^{1}H NMR spectra were obtained on an Inova 500 MHz spectrometer or a Mercury 300 spectrometer where chemical shifts (δ with units of ppm) were determined using a residual solvent proton as standard. Gas sorption measurements were conducted on a Micromeritics' ASAP 2020 system and standardized against a dedicated P° sensor. High-pressure CH_4 adsorption isotherms were carried out on an HPVA II high pressure volumetric analyzer.

III.2.2 Ligand Synthesis

III.2.2.1 Synthesis of 4,4'-NH_2-H_4TPCB

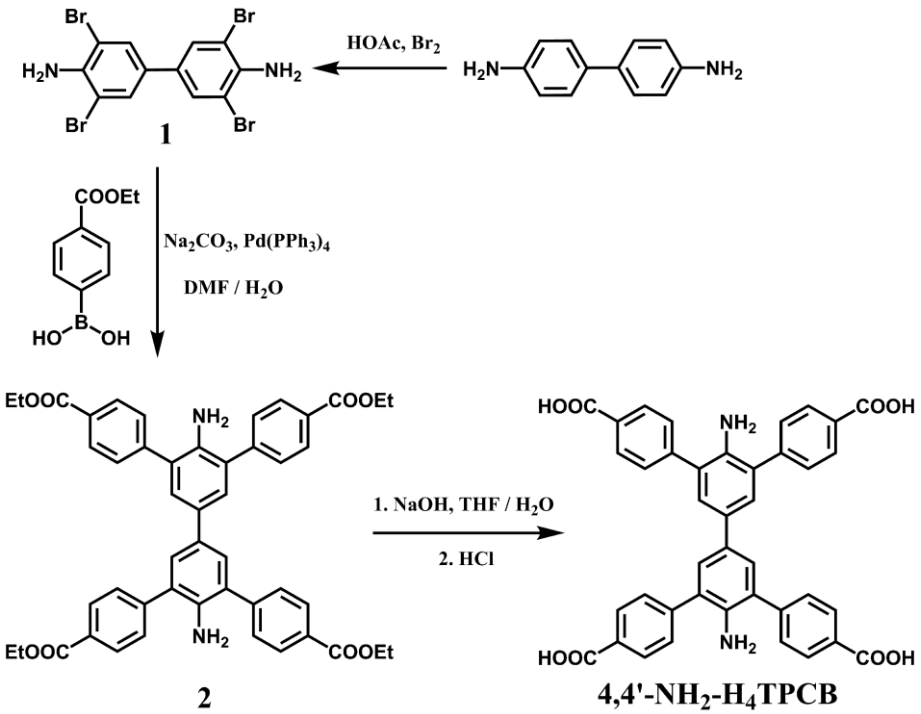

Figure 20. Synthesis of 4,4'-diamino-biphenyl-3,3',5,5'-tetra(phenyl-4-carboxylic acid (4,4'-NH_2-H_4TPCB).

III.2.2.1.1 Synthesis of 3,3',5,5'-tetrabromo-4,4'-diamino-biphenyl (1)

Bromine (4 mL, 80 mmol) was added to a solution of 4,4'-benzidine (3.7 g, 20 mmol) in acetic acid (100 mL) and stirred at 35 ^{o}C for 30 min. The reaction solution was poured into ice water and stirred vigorously. The resulting precipitate was filtered and washed sequentially with aqueous solutions of $NaHCO_3$, Na_2SO_3, and water. Pure

compound 1 was obtained by recrystallization in toluene (7.3 g, 73 %). ^{1}H NMR spectroscopy detected 2 peaks (300 MHz, DMSO-d_6) δ 5.39 (s, 4H), 7.73 (s, 4H) ppm.

III.2.2.1.2 Synthesis of 3,3',5,5'-tetra(ethyl-4-carboxyphenyl)-4,4'-diamino-biphenyl (2)

Compound 1 (2 mmol, 1 g), (4-(ethoxycarbonyl)phenyl)boronic acid (4.18 g, 12 mmol), Cs_2CO_3 (11.8 g, 36 mmol), and tetrakis(triphenylphosphine)palladium (0.092 g, 0.08 mmol) were added to a 500-mL Schlenk flask charged with a stir bar. The flask was pumped under vacuum and refilled with N_2 three times before 300 mL degassed 1,4-dioxane was transferred to the system and the reaction mixture was heated at 85 °C for 72 h under a N_2 atmosphere. After the reaction mixture was cooled to room temperature, the organic solvent was removed using a rotary evaporator, and the resulting mixture was poured into water and extracted with dichloromethane (3 × 100 mL). The combined organic layers were dried over anhydrous $MgSO_4$ before the solvent was removed again using a rotary evaporator. After purification by column chromatography on silica gel using ethyl acetate/hexane (1:3 v/v) as eluent and evaporation of the fraction containing the product, compound 2 was obtained as a pale yellow solid (1.2 g, 78 %). ^{1}H NMR detected 6 distinct peaks (300 MHz, $CDCl_3$) δ 1.42 (t, 12H), 3.90 (s, 4H), 4.42 (q, 8H), 7.39 (s, 4H), 7.66 (d, 8H), 8.16 (d, 8H) ppm.

III.2.2.1.3 Synthesis of 4,4'-diamino-biphenyl-3,3',5,5'-tetra(phenyl-4-carboxylic acid) (4,4'-NH_2-H_4TPCB)

Compound 2 (3.1 g, 4 mmol) was dissolved in 30 mL of THF, to which 50 mL of 10 M NaOH aqueous solution was added. The mixture was stirred under reflux for 10 h before the organic solvent was removed using a rotary evaporator. The aqueous phase was acidified to pH = 2 by dropwise addition of 6 M HCl aqueous solution. The resulting precipitate was collected via filtration, washed with water (200 mL), and dried under vacuum to afford 4,4'-NH_2-H_4TPCB (2.4 g, 90 %). ^{1}H NMR detected 5 peaks (300 MHz, DMSO-d_6) δ 3.49 (s, 4H), 7.40 (s, 4H), 7.67 (d, 8H), 8.05 (d, 8H), 13.05 (s, 4H) ppm.

III.2.2.2 Synthesis of 4,4’-OMe-H_4TPCB

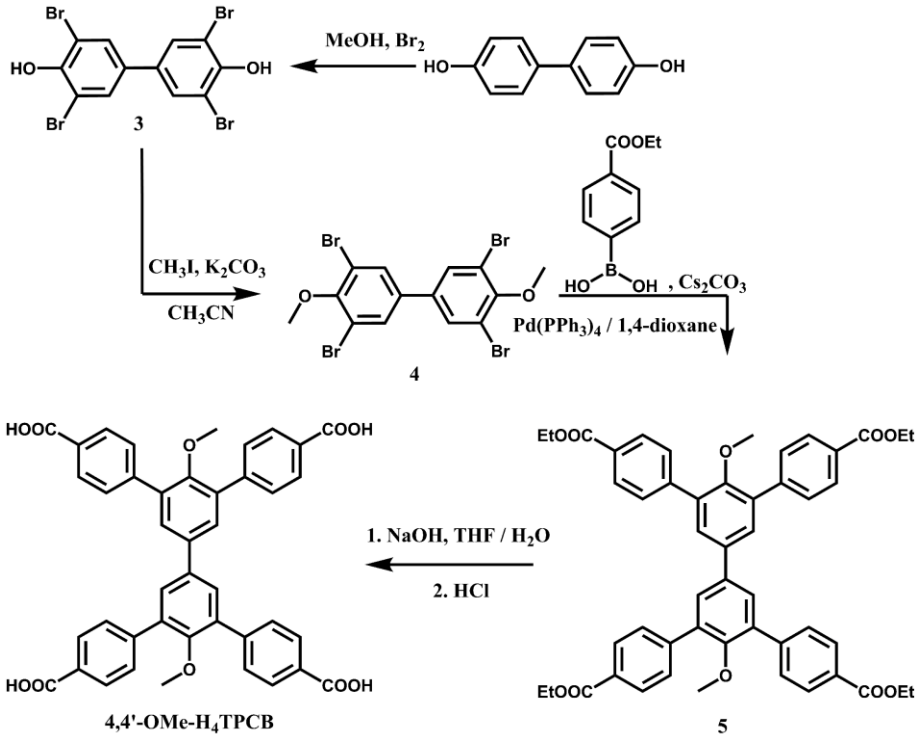

Figure 21. Synthesis of 4,4'-dimethoxybiphenyl-3,3',5,5'-tetra(phenyl-4-carboxylic acid (4,4’-OMe-H_4TPCB).

III.2.2.2.1 Synthesis of 3,3’,5,5’-tetrabromo-4,4’-biphenol (3)

Bromine (13.8 mL, 268.6 mmol) was added to a solution of 4,4’-biphenol (10 g, 54 mmol) in methanol (400 mL). After 1 h of stirring, the resulting precipitate was filtered and washed sequentially with aqueous solutions of $NaHCO_3$, Na_2SO_3, and water. The resulting white powder was dissolved in acetone and dried over anhydrous Na_2SO_4. Pure compound 3 was obtained by recrystallization in acetone (14.6 g, 54 %). ^{1}H NMR detected 2 distinct peaks (300 MHz, DMSO-d_6) δ 7.87 (s, 4H), 10.03 (s, 2H) ppm.

III.2.2.2.2 Synthesis of 3,3',5,5'-tetrabromo-4,4'-dimethoxy-1,1'-biphenyl (4)

Compound 3 (4.0 g, 8 mmol), methyl iodide (6.8 g, 48 mmol), and K_2CO_3 (3.3 g, 24 mmol) were dissolved into acetonitrile (100 mL). The reaction mixture was heated at reflux for 18 h and then cooled to room temperature. Acetonitrile was removed using rotary evaporation and the resulting mixture was poured into water and extracted with dichloromethane (3 × 100 mL). The combined organic layers were dried over anhydrous $MgSO_4$, and then the solvent was removed again using a rotary evaporator. After purification by column chromatography on silica gel using hexane as eluent and evaporation of the fraction containing the product, compound 4 was obtained as a white powder (2.88 g, 68 %). ^{1}H NMR (300 MHz, $CDCl_3$) δ 3.94 (s, 6H), 7.65 (s, 4H) ppm.

III.2.2.2.3 Synthesis of 3,3',5,5'-tetra(ethyl-4-carboxyphenyl)-4,4'-dimethoxy-biphenyl (5)

Compound 4 (1.06 g, 2 mmol), (4-(ethoxycarbonyl)phenyl)boronic acid (4.18 g, 12 mmol), Cs_2CO_3 (11.8 g, 36 mmol), and tetrakis(triphenylphosphine)palladium (0.092 g, 0.08 mmol) were added to a 500-mL Schlenk flask charged with a stir bar. The flask was pumped under vacuum and refilled with N_2 three times before 300 mL degassed 1,4-dioxane was transferred to the system. The reaction mixture was heated to 85 °C for 72 h under a N_2 atmosphere. After the reaction mixture cooled to room temperature, the organic solvent was removed using a rotary evaporator, and the resulting mixture was poured into water and extracted with dichloromethane (3 × 100 mL). The combined organic layers

were dried over anhydrous $MgSO_4$, and then the solvent was removed again using a rotary evaporator. After purification by column chromatography on silica gel using ethyl acetate/hexane (1:5 v/v) as eluent and evaporation of the fraction containing the product, compound 5 was obtained as a pale yellow solid (1.32 g, 82 %). ^{1}H NMR detected 6 distinct peaks (300 MHz, $CDCl_3$): δ 1.44 (t, 12H), 3.20 (s, 6H), 4.43 (q, 8H), 7.63 (s, 4H), 7.76 (d, 8H), 8.15 (d, 4H) ppm.

III.2.2.2.4 Synthesis of 4,4'-dimethoxybiphenyl-3,3',5,5'-tetra(phenyl-4-carboxylic acid) (4,4'-OMe-H_4TPCB)

Compound 5 (3.23 g, 4 mmol) was dissolved in 30 mL of THF, to which 50 mL of 10 M NaOH aqueous solution was added. The mixture was stirred under reflux for 10 h, and then the organic solvent was removed using a rotary evaporator. The aqueous phase was acidified to pH = 2 by dropwise addition of 6 M HCl aqueous solution. The resulting precipitate was collected via filtration, washed with water (200 mL), and dried under vacuum to afford 4,4'-OMe-H_4TPCB (2.64 g, 95 %). ^{1}H NMR detected 4 distinct peaks (300 MHz, DMSO-d_6) δ3.12 (s, 6H), 7.82 (t, 12H), 8.03 (d, 8H), 12.98 (s, 4H) ppm.

III.2.2.3 Synthesis of 4,4'-OCp-H_4TPCB

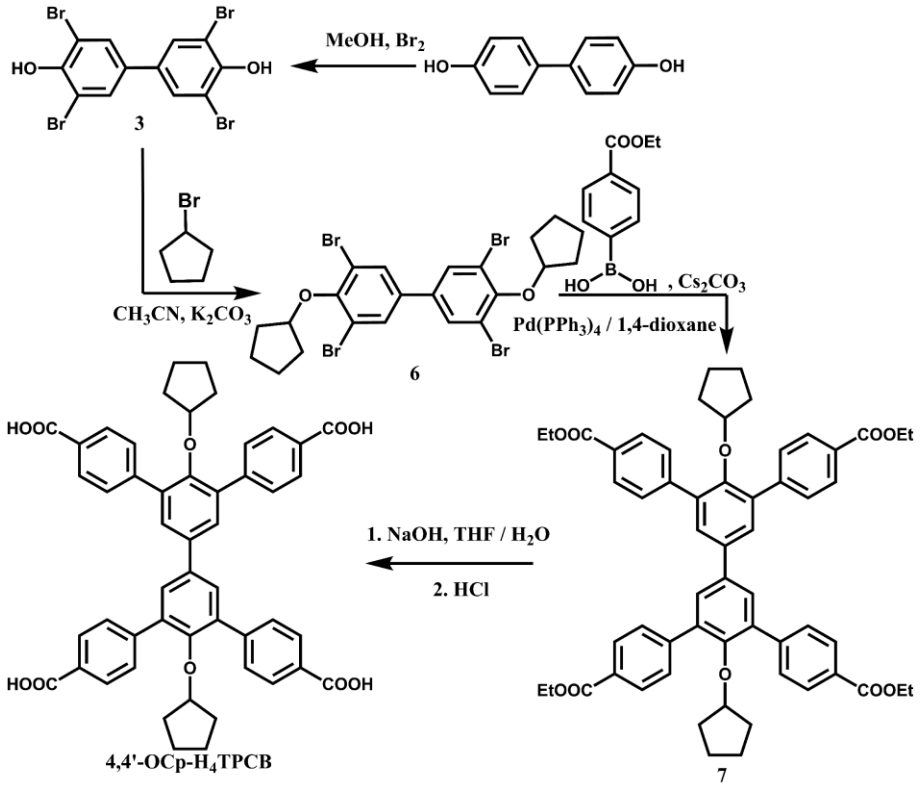

Figure 22. Synthesis of 4,4'-dicyclopentyloxybiphenyl-3,3',5,5'-tetra(phenyl-4-carboxylic acid) (4,4'-OCp-H_4TPCB).

III.2.2.3.1 Synthesis of 3,3',5,5'-tetrabromo-4,4'-dicyclopentyloxy-1,1'-biphenyl (6)

Compound 3 (4.0 g, 8 mmol), bromocyclopentane (7.15 g, 48 mmol), and K_2CO_3 (3.3 g, 24 mmol) were dissolved into acetonitrile (100 mL). The reaction mixture was heated at reflux for 18 h and then cooled to room temperature. Acetonitrile was removed using rotary evaporation and the resulting mixture was poured into water and extracted with dichloromethane (3 × 100 mL). The combined organic layers were dried over anhydrous $MgSO_4$, and then the solvent was removed again using a rotary evaporator. After purification by column chromatography on silica gel using hexane as eluent and

evaporation of the fraction containing the product, compound 6 was obtained as a white powder (2.86 g, 56 %). ^{1}H NMR detected 6 distinct peaks (300 MHz, $CDCl_3$) δ 1.66 (m, 4H), 1.82 (m, 4H), 2.00 (m, 4H), 2.08 (m, 4H), 5.04 (m, 2H), 7.67 (s, 4H) ppm.

III.2.2.3.2 Synthesis of 3,3',5,5'-tetra(ethyl-4-carboxyphenyl)-4,4'-dicyclopentyloxy-biphenyl (7)

Compound 6 (1.28g, 2 mmol), (4-(ethoxycarbonyl)phenyl)boronic acid (2.33 g, 12 mmol), Cs_2CO_3 (11.8 g, 36 mmol), and tetrakis(triphenylphosphine)palladium (0.092 g, 0.08 mmol) were added to a 500-mL Schlenk flask charged with a stir bar. The flask was pumped under vacuum and refilled with N_2 three times before 300 mL degassed 1,4-dioxane was transferred to the system. The reaction mixture was heated to 85 °C for 72 h under a N_2 atmosphere. After the reaction mixture cooled to room temperature, the organic solvent was removed using a rotary evaporator, and the resulting mixture was poured into water and extracted with dichloromethane (3 × 100 mL). The combined organic layers were dried over anhydrous $MgSO_4$, and then the solvent was removed again using a rotary evaporator. After purification by column chromatography on silica gel using ethyl acetate/hexane (1:4 v/v) as eluent and evaporation of the fraction containing the product, compound 7 was obtained as a pale yellow solid (1.24 g, 68 %). ^{1}H NMR detected 8 distinct peaks (300 MHz, $CDCl_3$): δ 1.07 (m, 12H), 1.35 (m, 4H), 1.45 (t, 12H), 3.84 (s, 4H), 4.45 (q, 8H), 7.63 (s, 4H), 7.86 (d, 8H), 8.14 (d, 8H) ppm.

III.2.2.3.3 Synthesis of 4,4'-dicyclopentyloxybiphenyl-3,3',5,5'-tetra(phenyl-4-carboxylic acid) (4,4'-OCp-H_4TPCB)

Compound 7 (3.23 g, 4 mmol) was dissolved in 30 mL of THF, to which 50 mL of 10 M NaOH aqueous solution was added. The mixture was stirred under reflux for 10 h, and then the organic solvent was removed using a rotary evaporator. The aqueous phase was acidified to pH = 2 by dropwise addition of 6 M HCl aqueous solution. The resulting precipitate was collected via filtration, washed with water (200 mL), and dried under vacuum to afford 4,4'-OCp-H_4TPCB (2.64 g, 95 %). ^{1}H NMR (300 MHz, DMSO-d_6) δ 0.91 (m, 4H), 1.10 (m, 8H), 1.28 (m, 4H), 3.76 (m, 2H), 7.85 (t, 12H), 8.03 (d, 8H), 12.99 (s, 4H) ppm.

III.2.2.4 Synthesis of H_4CBTB

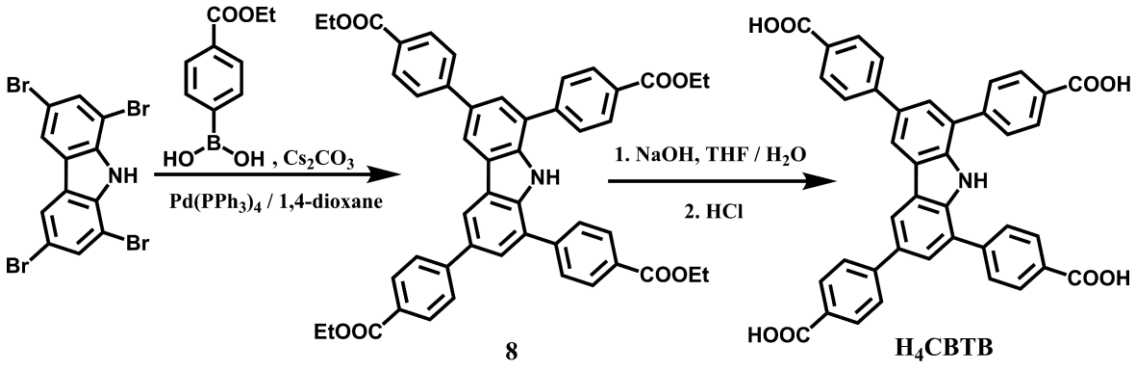

Figure 23. Synthesis of tetraethyl 4,4',4",4'"-(9H-carbazole-1,3,6,8-tetrayl)tetrabenzoate (H_4CBTB).

III.2.2.4.1 Synthesis of tetraethyl 4,4',4'',4'''-(9H-carbazole-1,3,6,8-tetrayl)tetrabenzoate (8)

1,3,6,8-tetrabromo-9H-carbazole (1.45g, 3 mmol), (4-(ethoxycarbonyl)phenyl)boronic acid (3.49 g, 18 mmol), Cs_2CO_3 (11.8 g, 36 mmol), and tetrakis(triphenylphosphine)palladium (0.14 g, 0.12 mmol) were added to a 500-mL Schlenk flask charged with a stir bar. The flask was pumped under vacuum and refilled with N_2 three times before 250 mL degassed 1,4-dioxane was transferred to the system. The reaction mixture was heated to 85 °C for 72 h under a N_2 atmosphere. After the reaction mixture cooled to room temperature, the organic solvent was removed using a rotary evaporator, and the resulting mixture was poured into water and extracted with dichloromethane (3 × 100 mL). The combined organic layers were dried over anhydrous $MgSO_4$, and then the solvent was removed again using a rotary evaporator. After purification by column chromatography on silica gel using ethyl acetate/hexane (1:5 v/v) as eluent and evaporation of the fraction containing the product, compound **8** was obtained as pale yellow solid (1.81 g, yield: 79 %). ^{1}H NMR detected 8 distinct peaks (300 MHz, $CDCl_3$): δ 1.46 (m, 12H), 4.47 (m, 8H), 7.80 (d, 6H), 7.88 (d, 4H), 8.19 (d, 4H), 8.26 (d, 4H), 8.48 (s, 2H), 8.53 (s, 1H) ppm.

III.2.2.4.2 Synthesis of 4,4',4'',4'''-(9H-carbazole-1,3,6,8-tetrayl)tetrabenzoic acid (H_4CBTB)

Compound **8** (1.52 g, 2 mmol) was dissolved in 15 mL of THF, to which 20 mL of 10 M NaOH aqueous solution was added. The mixture was stirred under reflux for 10

h, and then the organic solvent was removed using a rotary evaporator. The aqueous phase was acidified to pH = 2 by dropwise addition of 6 M HCl aqueous solution. The resulting precipitate was collected via filtration, washed with water (200 mL), and dried under vacuum to afford **H_4CBTB** (1.24 g, 96 %). ^{1}H NMR detected 5 distinct peaks (300 MHz, DMSO-d_6) δ7.89 (d, 2H), 8.08 (m, 16H), 8.88 (s, 2H), 10.98 (s, 1H), 12.99 (s, 4H) ppm.

III.2.3 MOF Synthesis

III.2.3.1 Synthesis of PCN-648

$Fe_3(\mu_3\text{-}O)(CH_3COO)_6$ (100 mg), 4,4'-NH_2-H_4TPCB (50 mg), acetic acid (3 mL), and DMF (16 mL) were charged in a 20 mL Pyrex vial. The mixture was heated in a 150 °C oven for 4 days. After cooling down to room temperature, the red crystals of PCN-648 were harvested (yield: 72 %).

III.2.3.2 Synthesis of PCN-658

$Fe_3(\mu_3\text{-}O)(CH_3COO)_6$ (100 mg), 4,4'-OCp-H_4TPCB (50 mg), acetic acid (3 mL), and DMF (16 mL) were charged in a 20 mL Pyrex vial. The mixture was heated in a 150 °C oven for 3 days. After cooling down to room temperature, the red crystals of PCN-658 were harvested (yield: 65 %).

III.2.3.3 Synthesis of PCN-678

$Fe_3(\mu_3\text{-}O)(CH_3COO)_6$ (100 mg), 4,4'-OMe-H_4TPCB (50 mg), acetic acid (3 mL), and DMF (16 mL) were charged in a 20 mL Pyrex vial. The mixture was heated in a 150

°C oven for 3 days. After cooling down to room temperature, the red crystals of PCN-678 were harvested (yield: 81 %).

III.2.3.4 Synthesis of PCN-668 (Single crystal)

$Fe(NO_3)_3 \cdot 9H_2O$ (100 mg), H_4CBTB (50 mg), acetic acid (3 mL), and DMF (16 mL) were charged in a 20 mL Pyrex vial. The mixture was heated in a 150 °C oven for 7 days. After cooling down to room temperature, the red crystals of PCN-668 were harvested (yield: 23 %).

III.2.3.5 Synthesis of PCN-668 (Powder)

$Fe(NO_3)_3 \cdot 9H_2O$ (100 mg), H_4CBTB (50 mg), acetic acid (1 mL), and DMF (17 mL) were charged in a 20 mL Pyrex vial. The mixture was heated in a 150 °C oven for 3 days. After cooling down to room temperature, the resulting PCN-668 powder was harvested (yield: 63 %).

III.2.3.6 Synthesis of PCN-668-Cr

100 mg $CrCl_3 \cdot 6H_2O$ was dissolved in 10 mL acetone upon ultrasonification. PCN-668 (ca. 50 mg) was dispersed in the solution (5 mL) and heated for about 4 hours at 80 °C. This procedure was repeated 3 times. After cooling down to room temperature, the green crystals of PCN-668-Cr were harvested (yield: 90 %).

III.2.4 Single Crystal X-ray Diffraction

Single crystals of the MOFs were taken from the mother liquid without further treatment, transferred to oil, and mounted onto a loop for single crystal X-ray data collection. Diffraction was measured on a Bruker Smart Apex diffractometer equipped with a Cu-Kα microfocus tube X-ray source (λ = 1.54178 Å) and a low temperature device (100 K). The structure was solved by direct methods using *SHELXS* and refined by full-matrix least-squares on F^2 using *SHELXL* software. All non-hydrogen atoms were refined with anisotropic displacement parameters. The hydrogen atoms on the aromatic rings were located at geometrically calculated positions and refined by riding. However, the hydrogen atoms for the coordinated molecules could not be easily found from the residual electron density peaks and the attempt of theoretical addition was not done. Therefore, the number of reported hydrogen atoms is more than the calculated value. The free solvent molecules are highly disordered in MOFs and attempts to locate and refine the solvent peaks were unsuccessful. The diffused electron densities resulting from these solvent molecules were removed using the SQUEEZE routine of PLATON; structures were then refined again using the data generated. Crystal data are summarized in **Table 4** and **Table 5**. CCDC 1569627 contains the supplementary crystallographic data for PCN-648, PCN-658, PCN-678 and PCN-668. These data can be obtained free of charge from The Cambridge Crystallographic Data Centre.

Table 4. Crystal data and structure refinements for PCN-648 and PCN-658.

	PCN-648	PCN-658
CCDC	1959592	1959591
Formula	$C_{49}H_{42}Fe_3N_4O_{16}$	$C_{52}H_{30}Fe_3O_{16}$
Formula weight	1110.41	1078.31
T (K)	100	100
Wavelength (Å)	1.54184	1.54184
Shape / Color	block / brown	block / yellow
Crystal System	orthorhombic	monoclinic
Space group	Cmca	C2/c
Unit Cell	a = 30.8378(9) Å	a = 20.6800(14) Å
	b = 32.0582(9) Å	b = 32.981(2) Å
	c = 15.7523(5) Å	c = 12.0834(9) Å
	$\alpha = \beta = \gamma = 90$ °	$\alpha = \gamma = 90$ °
	V = 15572.8(8) Å^3	β = 120.913(2) °
		V = 7070.7(9) Å^3
Z	8	4
d_{calcd} (g/cm^3)	0.947	0.988
μ (mm^{-1})	4.828	0.656
F (000)	4560	2079
Completeness	0.996	0.998
Collected reflections	5509	7247
Unique reflections	4169	4932
Parameters	264	280
R_{int}	0.0327	0.0300
R_1 [I > 2σ(I)]	0.1146	0.1137
wR_2 [I > 2σ(I)]	0.3632	0.3782
R_1 (all data)	0.1346	0.1431
wR_2 (all data)	0.3818	0.4169

Table 4. Continued

	PCN-648	PCN-658
GOF on F^2	1.592	1.685

Table 5. Crystal data and structure refinements for PCN-678 and PCN-668.

	PCN-678	PCN-668
CCDC	1959594	1959593
Formula	$C_{42}H_{30.67}Fe_2O_{12.67}$	$C_{40}H_{29.33}Fe_2NO_{10.67}$
Formula weight	849.70	806.34
T (K)	100	100
Wavelength (Å)	1.54184	1.54184
Shape / Color	block / dark red	block / dark red
Crystal System	trigonal	hexagonal
Space group	R-3	$P6_3/mcm$
Unit Cell	a = 19.7416(4) Å	a = 39.6049(17) Å
	c = 44.7819(10) Å	c = 62.220(3) Å
	$\alpha = \beta$ = 90 º	$\alpha = \beta$ = 90 º
	γ = 120 º	γ = 120 º
	V = 15114.6(7) Å^3	V = 84520(8) Å^3
Z	9	24
d_{calcd} (g/cm^3)	0.840	0.380
μ (mm^{-1})	3.790	1.790
F (000)	3924	9928
Completeness	0.987	0.994
Collected reflections	5344	4051
Unique reflections	4751	2889
Parameters	257	455
R_{int}	0.0224	0.0512
R_1 [I > 2σ(I)]	0.0456	0.0468

Table 5. Continued

	PCN-678	PCN-668
wR_2 [I > 2σ(I)]	0.1599	0.1235
R_1 (all data)	0.0487	0.0578
wR_2 (all data)	0.1651	0.1262
GOF on F^2	0.742	1.009

III.2.5 SEM/EDS Mapping

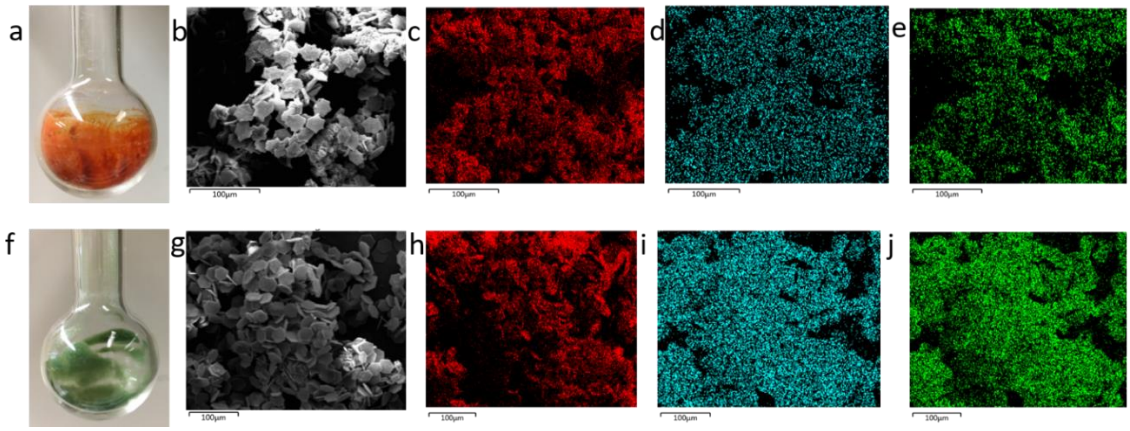

Figure 24. Images of (a) PCN-668 and (f) PCN-668-Cr. SEM images of (b) PCN-668 and (g) PCN-668-Cr. The eds mapping of PCN-668: (c) carbon, (d) iron, (e) oxygen, and PCN-668-Cr: (h) carbon, (i) chromium, (j) oxygen.

III.2.6 N_2 Sorption Isotherms

N_2 adsorption measurements were performed using a Micromeritics ASAP 2020 surface area and pore size analyzer. Before sorption experiments, as-synthesized samples were washed with DMF several times to remove unreacted starting ligands and inorganic species. Afterwards, the crystals were carefully decanted and washed with DMF and acetone several times. Then the samples were activated under vacuum at 80 °C for 10 h.

Low-pressure N_2 adsorption isotherms were measured at 77 K in a liquid nitrogen bath. The specific surface areas were determined using the Brunauer-Emmett-Teller model from the N_2 sorption data.

III.2.7 PXRD

MOF crystalline powders were collected after synthesis and prepared for activation by slow solvent exchange from DMF to a lower boiling point solvent (acetone). Solvent was separated from the MOF crystals and activation was done under vacuum and heating at 80 °C for 5 h. At this point, sample was divided into four parts for different treatment. PXRD data was collected on one apportionment without treatment, below labeled as 'as-synthesized'. The remaining samples were soaked in either neutral pH aqueous solution, pH=11 aqueous solution, or pH=1 aqueous solution for 24 hours before solution was removed and samples were dried for PXRD data collection. Related samples were layered and compared with simulated patterns.

III.3 Results and Discussion

Initially, unsubstituted H_4TPCB and 2,2'-OH-H_4TPCB were selected as organic linkers in the synthesis of Zr-frameworks, but no crystalline product could be obtained. When substituents were introduced to the 4,4'-positions, a two-dimensional MOF (PCN-648) based on 4,4'-NH_2-TPCB and the Fe_3O cluster (**Figure 25**) and a three-dimensional microporous MOF (PCN-678) based on 4,4'-OMe-TPCB and the Fe_3O cluster were formed. The 4,4'-NH_2-TPCB ligand adopts a D_2 symmetry in PCN-648 with a dihedral

angle of 35.13° between the two inner phenyl rings while the 4,4'-OMe-TPCB ligand adopts a C_{2v} symmetry in PCN-678 with the two inner phenyl rings coplanar.

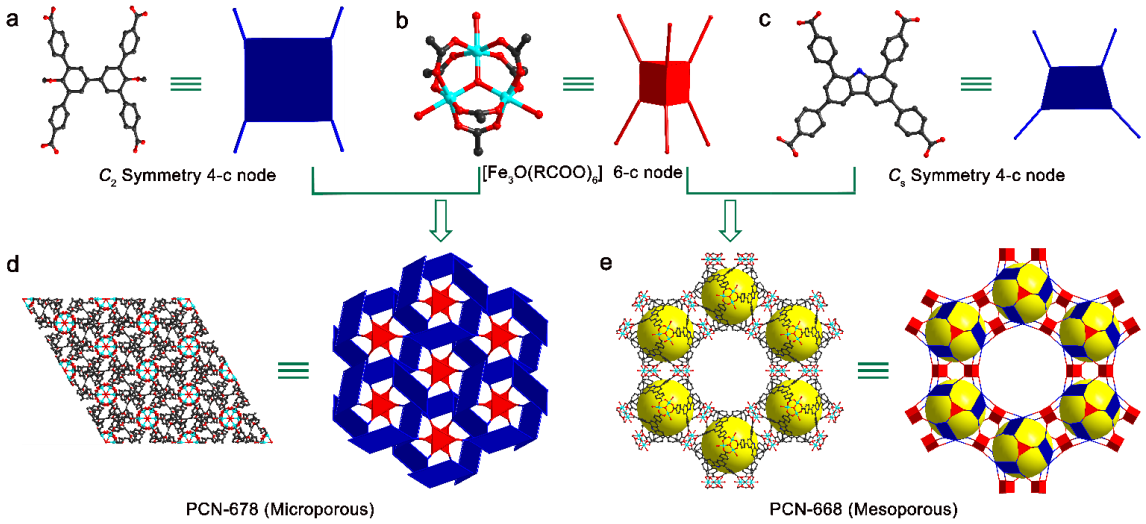

Figure 25. The crystal structure and topology of PCN-678 and PCN-668. a) The C2 symmetry, 4-connected 4,4'-OMe-TPCB4- ligand. b) The 6-connected trigonal-prismatic [Fe3O(RCOO)6] cluster. c) The Cs symmetry, 4-connected CBTB4- ligand. d) Perspective view of PCN-678 along the c axis and the (4,6)-c topology of the microporous framework. e) Perspective view of PCN-668 along the c axis and the (4,6)-c topology of the mesoporous framework. Color scheme: black, C; red, O; blue, N; light blue, Fe. For clarity, H atoms are not shown.

Interestingly, while the metal cluster in PCN-678 was 6-connected as expected, the cluster in PCN-648 was 4-connected with two sites occupied by terminally coordinated formate and acetate molecules. From a topological point of view, simplification of the 4,4'-OMe-TPCB^{4-} ligands as 4-connected nodes and Fe_3 clusters as 6-connected nodes, PCN-678 adopts a new 4,6-c net with the topological point symbol of $\{4^2.6^3.8\}_3\{4^3.6^9.8^3\}_2$ (**Figure 25**). In Zr-tetracarboxylate framework systems, increasing the size of the

substituents in the 4,4'-position prompts the formation of mesoporous, csq-topology MOFs (PCN-608).[65] Therefore, the 4,4'-OCy-TPCB ligand, with its large substituents, was also studied in the Fe-tetracarboxylate frameworks system. However, direct synthesis methods using this ligand yielded only a microporous MOF (termed PCN-658). The ligand in PCN-658 adopts a D_2 symmetry with a dihedral angle of 48.89° between the two inner phenyl rings, which is similar to that of 4,4'-NH_2-TPCB in PCN-648. Strangely, no trinuclear cluster can be observed in PCN-648. Rather, an iron chain was formed bridged by two carboxylate groups from the linker and one formate. In the past, we have developed a strategy to construct iron MOFs on the basis of trinuclear iron clusters using pre-synthesized clusters in our previous work.[77] Therefore, synthesis with 4,4'-OCy-TPCB ligands was attempted using the pre-synthesized trinuclear iron clusters instead of $Fe(NO_3)_3$. Again, attempts to obtain PCN-648 with trinuclear iron clusters rather than iron chains failed.

It has been confirmed by Matzger and co-workers that diverse structures can be obtained using reduced symmetry ligands.[78, 79] We have also successfully obtained a series of multicomponent Zr-MOFs using a reduced symmetry ligand H_4CBTB (PCN-609 series).[80] Bearing this in mind, the trapezoidal, tetratopic carboxylate ligand H_4CBTB was selected to construct new iron MOFs with intriguing structures. Solvothermal reactions of H_4CBTB, $Fe(NO_3)_3$•$9H_2O$, and acetic acid in DMF afford the mesoporous framework complex $[Fe_6(\mu_3\text{-}OH)_2(CBTB)_3(H_2O)_6]$•$(solvent)_x$ (termed PCN-668). Single-crystal X-ray diffraction experiments at 100 K reveal that PCN-668 is constructed by fully deprotonated $CBTB^{4-}$ ligands and trinuclear $[Fe_3O(COOR)_6]$ clusters, crystallizing in the

hexagonal space group $P6_3/mcm$. Each $CBTB^{4-}$ ligand coordinates to four Fe_3 clusters and each Fe_3 cluster links to six $CBTB^{4-}$ ligands (**Figure 25**). Combination of six $CBTB^{4-}$ ligands and eight Fe_3 clusters form a cubic cage-like secondary building unit (SBU) with dimensions of approximately 18 Å. The cubic nanocage SBU is slightly distorted because of the low symmetry of the $CBTB^{4-}$ ligands and distortion of the clusters. Each cage is linked to two neighboring cages through the sharing of one Fe_3 cluster vertex on the two poles and four neighboring cages through the sharing of two Fe_3 cluster vertices (or one edge) in the equatorial plane. On the whole, the cubic cages are connected to form a three-dimensional, non-interpenetrated network (**Figure 25**). In addition, connection of the nanocages one by one gives rise to a very large round channel with the cubic nanocages arranged neatly on the walls of the channel. Mesoporous channels open along the *c* axis with dimensions of approximately 22 Å. For a clearer description of the framework, the $CBTB^{4-}$ ligands may be simplified as 4-connected nodes and the Fe_3 clusters as 6-connected nodes. In this way, PCN-668 adopts a new 4,6-c net with a topological point symbol of $\{4^{10}6^48\}_3\{4^46^2\}_6\{4^68^9\}$ (**Figure 25**).

Interestingly, any two neighboring nanocages in PCN-668 are not coincident through any symmetrical operation — that is, they are enantiomeric cages (**Figure 26**). To the best of our knowledge, this is the first mesoporous MOF based on enantiomeric polyhedral nanocages. The CBTB ligand favors C_s symmetry with a C_2 symmetrical axis, as is observed in the Zr-based framework PCN-609. However, the self-assembly of CBTB ligands with Fe_3O clusters forces the ligand to asymmetry, producing chiral cage-like units

(**Figure 26**). Overall, the *m* symmetrical plane in PCN-668 makes it a mesomeric framework.

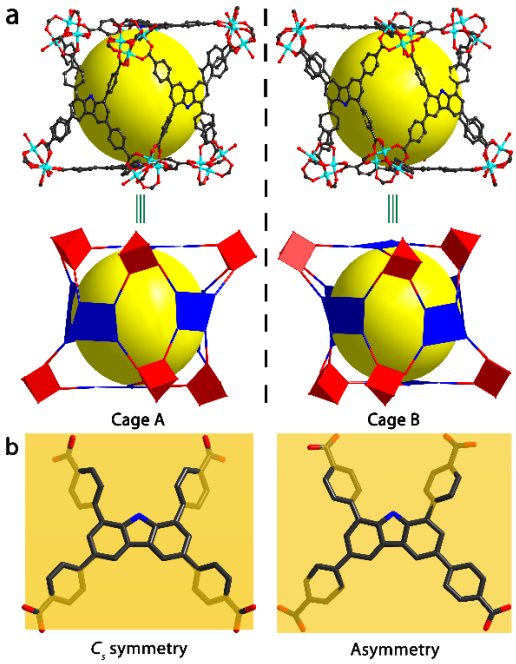

Figure 26. (a) The enantiomeric cage-like secondary building units observed in PCN-668. (b) The ideal C_s symmetry and the C_1 symmetrical $CBTB^{4-}$ ligand in PCN-668. Color scheme: black, C; red, O; light blue, Fe. For clarity, H atoms are not shown.

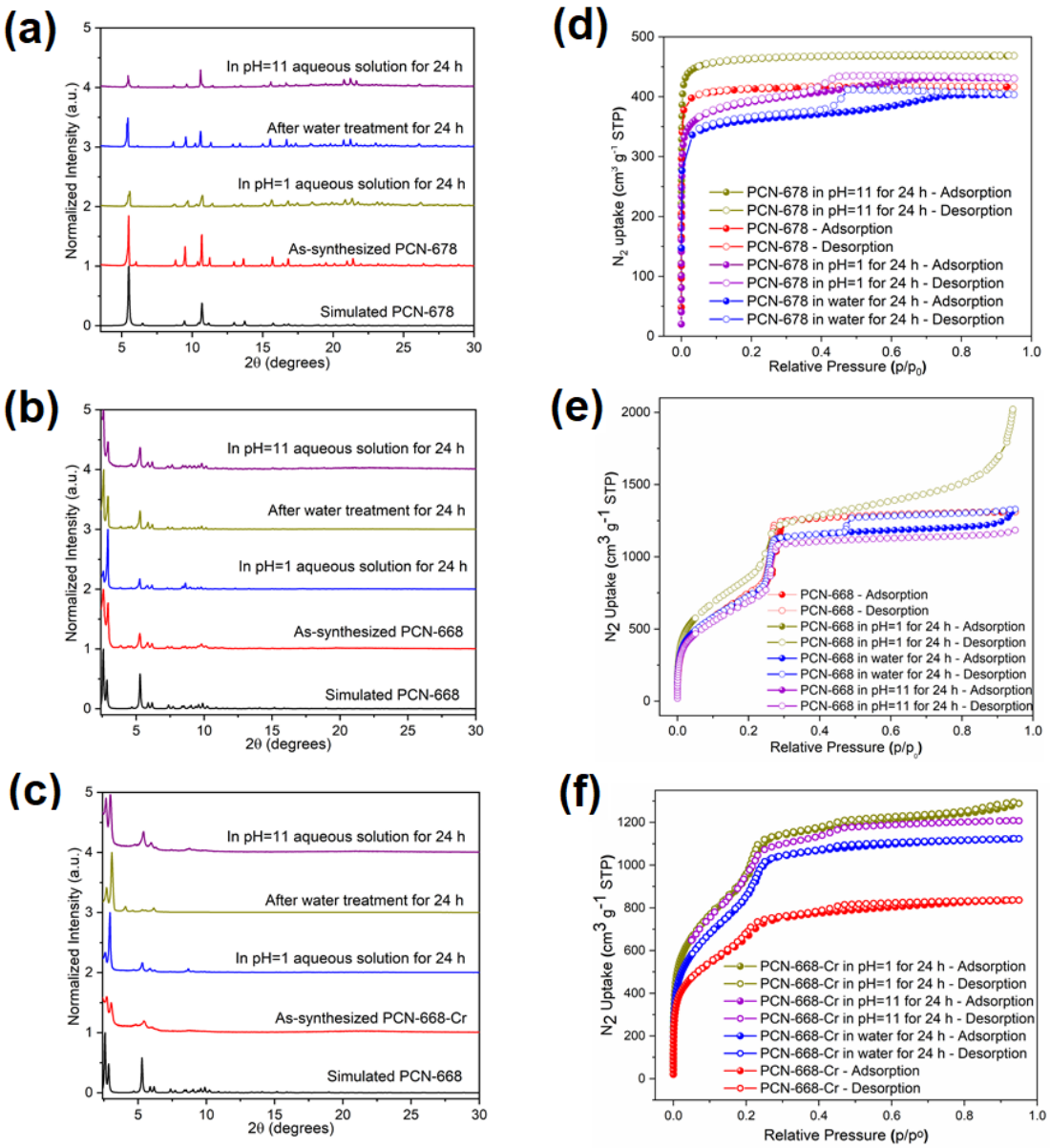

Figure 27. Stability tests for the microporous MOF PCN-678 and mesoporous MOFs PCN-668 and PCN-668-Cr. PXRD patterns of (a) PCN-678, (c) PCN-668, and (e) PCN-668-Cr simulated, as-synthesized, and after 24 hour exposure to water, acidic solution, and basic solution. N_2 sorption isotherms for (b) PCN-678, (e) PCN-668, and (f) PCN-668-Cr as-synthesized, and after 24 hour exposure to water, acidic solution, and basic solution.

Hexagonal single crystals of PCN-668 were obtained with a significant amount of rectangular polycrystal impurity after week-long solvothermal reaction with 3 mL acetic acid at 150 °C. Considering that the acidity of the reaction system plays an important role in the synthesis of zirconium-based MOFs, the crystal growth conditions were minorly revised with carefully regulated dosage of the acetic acid modulator in order to obtain purer phase PCN-668.[77, 81-83] When 1 mL acetic acid was added to adjust the pH of the reaction mixture, pure microcrystalline PCN-668 was obtained after 3 days at 150 °C, as confirmed by powder X-ray diffraction experiments (**Figure 27**).

The frameworks of PCN-648 and PCN-658 collapse after removal of the mother liquor, indicative of low stability. Therefore, no porosity-related data can be obtained. The solvent accessible volume in fully evacuated PCN-678 and PCN-668 are 56.4 % and 81.2 %, respectively, calculated by PLATON with a probe of 1.8 Å. In order to check the permanent porosity of PCN-678 and PCN-668, nitrogen adsorption isotherms were measured at 77 K and 1 atm. As shown in **Figure 27**, the N_2 sorption of PCN-678 exhibits a typical type I isotherm with a saturated adsorption amount of 416 $cm^3\ g^{-1}$, signifying a microporous nature for PCN-678. In contrast, the N_2 sorption of PCN-668 exhibits a typical IV isotherm with a saturated adsorption amount of 1311 $cm^3\ g^{-1}$, signifying a mesoporous nature for PCN-668. The BET apparent surface area of PCN-678 and PCN-668 calculated from the N_2 adsorption data are 1720 ± 5 and 2772 ± 25 $m^2\ g^{-1}$, respectively. The pore size in activated PCN-678 and PCN-668 are also analyzed by the non-local density functional theory (NLDFT) model from the N_2 adsorption data with a narrow

distribution of micropores around 1.2 nm for PCN-678 and a narrow distribution of micropores around 1.5 nm and mesopores around 3.0 nm for PCN-668.

In order to investigate the chemical stability of these microporous and mesoporous MOFs, after washing with DMF and deionized water, as-synthesized crystalline samples of PCN-678 and PCN-668 were immersed in aqueous solutions with pH = 1, pH = 7, and pH = 11 for 24 hours. The PXRD patterns show that the frameworks remain intact after acidic or basic solution treatment, implying that no framework collapse or phase transition occurs during stability testing (**Figure 27**). The N_2 adsorption of the microporous MOFs after treatment show typical type I isotherms with a slight change of the adsorption amount. However, as shown in **Figure 27**, the nitrogen adsorption isotherm at 77 K of the acidic solution treated mesoporous MOF sample shows a rapid increase in the high-pressure region (0.8 - 1 atm). This phenomenon should be attributed to partial collapse of the framework and formation of macropores, indicating instability of the mesoporous MOF under acidic condition.

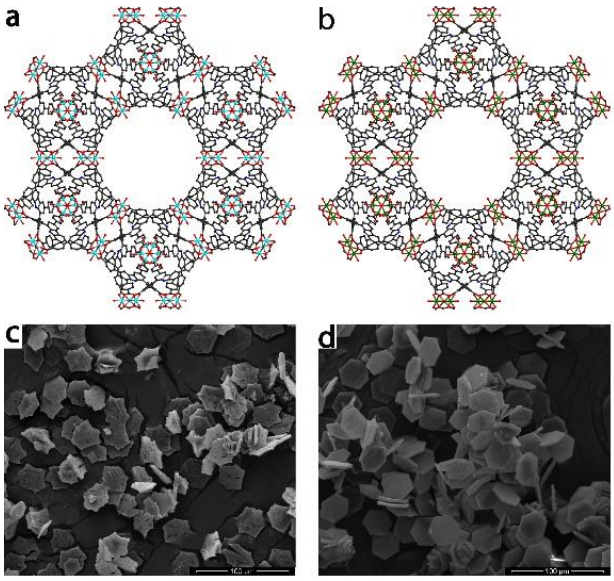

Figure 28. Comparison of PCN-668-Fe and PCN-668-Cr. (a) Crystal structure of PCN-668-Fe; (b) crystal structure of PCN-668-Cr. (c) SEM image of PCN-668-Fe; (d) SEM image of PCN-668-Cr.

According to the literature, trinuclear chromium-based MOFs can be obtained via a post-synthetic route which may be more stable than the precursor. Therefore, solvent-assisted metal metathesis was applied to PCN-668 to yield the Cr(III) analogue PCN-668-Cr. As shown in **Figure 24**, the sample color changed from yellow to green after metal exchange and SEM images show smoothing of the MOF crystals (**Figure 28**). EDX mapping, as well as ICP analysis, was recorded for PCN-668 before and after metal exchange to confirm the full exchange of Fe for Cr. The chemical stability of the new Cr(III)-based MOF was also examined. As expected, PCN-668-Cr boasts higher stability as confirmed from both the PXRD patterns and N_2 adsorption isotherms after acidic or basic aqueous solution treatment (**Figure 27**).

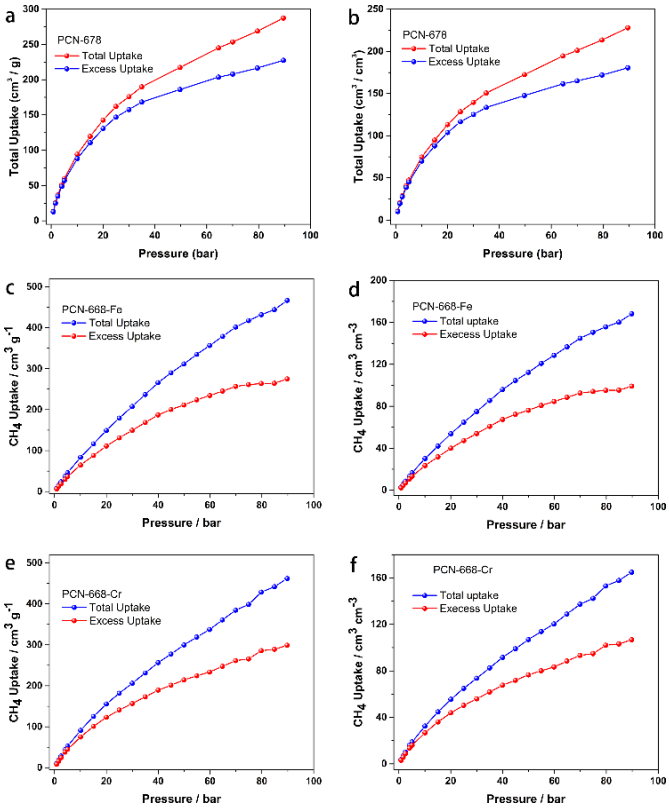

Figure 29. High-pressure methane uptake (total and excess) isotherms of PCN-678 (a, b), PCN-668-Fe (c, d), and PCN-668-Cr (e, f).

Considering the high porosity and stability of these microporous and mesoporous MOFs, high-pressure methane uptake properties were measured at room temperature. As shown in **Figure 29**, the microporous PCN-678 shows a total gravimetric methane uptake of 287 cm^3 g^{-1} at 90 bar while the mesoporous PCN-668 and PCN-668-Cr exhibit much higher total gravimetric methane uptakes of 467 and 462 cm^3 g^{-1}, respectively, at 90 bar. The relatively high gravimetric methane working capacity of the mesoporous MOFs (421 cm^3 g^{-1} for PCN-668 and 408 cm^3 g^{-1} for PCN-668-Cr from 90 to 5 bar) should be attributed to the high pore volume of the frameworks. However, considering crystal

density, the volumetric methane total uptake of PCN-678 (228 cm^3 cm^{-3} at 90 bar) is much higher than those of PCN-668 (168 cm^3 cm^{-3} for PCN-668 and 165 cm^3 cm^{-3} for PCN-668-Cr at 90 bar). In short, the mesoporous MOFs show better gravimetric methane storage properties, but the microporous MOF exhibits better volumetric methane storage properties.

In summary, we present the design and syntheses of two quite stable iron-based MOFs using tetratopic carboxylate ligands with different symmetries. The high symmetry linker-based PCN-678 is microporous, while the low symmetry linker-based PCN-668 is mesoporous. In PCN-668, there is a coexistence of nanoscale cage-like building units and an open, 1D channel. Due to the reduction of the ligand symmetry, the neighboring cages exist as mutual enantiomers. To further improve the chemical stability of the mesoporous MOF, solvent-assisted metal metathesis was applied to PCN-668 and a Cr(III)-based analogue was obtained. PCN-668-Cr exhibits very high stability to both acidic and basic aqueous solution treatments. In addition, PCN-678 shows high volumetric methane storage properties and PCN-668 exhibits high gravimetric methane uptake properties at room temperature.

From these results, a few suppositions may be derived. Linker symmetry reduction in MOFs has been verified as a reasonable means to (1) introduce new binding pockets for gas sorption tuning, (2) manipulate the rigidity and stability of the resulting MOF, and (3) guide toward micro- or mesoporosity, particularly in pursuit of stable mesoporous frameworks. Furthermore, although linker symmetry reduction in a Zr_6-based framework resulted in MOFs with identical **scu** topologies, a similar strategy with a Fe_3-based

framework provided entirely new topologies with the generation of alternating stereoisomeric cages.

CHAPTER IV

LOADING STUDIES OF UREA, THIOUREA, AND COMMERCIAL FERTILIZER INTO AN IRON-BASED MOF

IV.1 Introduction

The adeptness with which the agricultural industry has kept pace with exponentially growing demands for food stuffs is due in part to the increased application of fertilizers to augment the growth of stable food crops. The Food and Agriculture Organization of the United Nations published their *World fertilizer trends and outlook to 2022* projecting that the world demand for fertilizer will rise to a total of about 200,919,000 tonnes by the year 2022.[84] However, the boom in food production provided by fertilizers comes at an economic and environmental cost. Extensive fertilizer use contributes to the risk of bioaccumulation along with ground pollution, water pollution, and air pollution either through leaching into and contamination of ground or surface water or through volatilization and emissions in the form of ammonia, nitrous oxide, and nitric oxide.[85-88] Additionally, issues exist with the direct application of fertilizers, notably with the tradeoff between labor-intensive, frequent, low-dose irrigations and the risk of nutrient burn, or salt burn,[89, 90] in crops as well as increased leaching into the nearby environment. To address these problems, different strategies have been recommended to farmers. One strategy entails the planting of vegetation (known as buffers and vegetative filters) on the edges of and between agricultural fields and water sources to catch runoff.[91] However, this approach requires land to be set aside for a purpose other than supporting profit-generating

crops. Therefore, research into new fertilizer application methods has been a burgeoning area of interest.

To address these areas of concern, research has been conducted into developing controlled or slow release fertilizers (SRFs). SRFs work to slow down the release of fertilizers and the availability of fertilizer at any given time, preventing 'burst' uptakes of nutrient which can damage crops through nutrient burn and decreasing the number of applications necessary to keep crops properly nourished. Natural polymers such as cellulose, chitosan, starch, lignin, and alginate, synthetic polymers such as polyacrylamides and polyurethanes, and combined synthetic-natural polymers have all been investigated as SRFs.[92-95] Important considerations in choosing a matrix include the degradation pathways of the matrix so as not to replace one harmful pollutant with another and how the matrix materials interact with the fertilizer - as is a problem when polyacrylate is employed as its monomer, acrylic acid, will nullify some fertilizer components.[92] The most common type of SRF includes fertilizer dispersed throughout the pores of the release vehicle. The fertilizer release occurs are molecules slowly traverse and exit the host material's pores. This type of SRF can be synthetized using *in-situ* or two-step methodologies.[96-99] Another method for developing SRFs entails coating a fertilizer core with an inert materials and relying on diffusion through the shell for the slow-release function. Finally, some SRFs rely on chemically controlled degradation to release fertilizers into the environment. The release of fertilizer in these materials is typically verified and quantified by UV-Vis techniques or by use of a conductivity meter although more advanced methods such as the use of a lysimeter have also been employed. Although

these forms of SRFs have done a lot to improve agricultural yields, many coated fertilizers are limited by their mechanical stability and resistance to premature release upon damage during production, handling, and storage. Moreover, the release rate of these SRFs have been shown to be more variable than desired.[100] Improvements to SRF platforms remain to be made in order to address these issues.

The physical and chemical similarities and dissimilarities between MOFs and other widely studied porous materials have been previously summarized in the introductory section of this document though a few differences with regards to the specific application of SRFs are emphasized below. While all porous materials may exhibit adsorption of guest molecules, MOFs are well known for their high surface areas, permanent porosities, and crystallinity, lending them to higher sorption capacity and more consistent sorption capabilities. These properties offer enhanced fertilizer loadings, but they also may offer the additional benefit of enhance water retention and slow release of retained water rather than losing gravity pulling water away from roots. Second, MOF tunability is an essential advantage in the fact that the interaction strength between the framework and guest molecules may be modified with sites with hydrogen bonding potential or coordination-type interactions. This approach may be necessary to regulate the ease with which molecules are adsorbed (rate and amount) and the conditions upon which guests will desorb. Lastly, the high thermal stability of MOFs imparts a lot more leniency on fertilizer loading methods to include methods which require higher temperatures in order to obtain more complete loadings.

In order to consider MOFs as candidates for slow-release of fertilizer, a number of questions need to be addressed. Firstly, how can internal loading of fertilizer be assured as opposed to external presence of the fertilizer? Secondly, how can fertilizer that remains external to the MOF be removed without extracting any loaded internalized species? Lastly, how can uptake and release be observed, understood, and monitored? In seeking solutions to these concerns, the literature was scoured for precedence. Past studies pursuing MOFs as SRFs often rely on degradation of the MOF for proper fertilizer release. Oxalate-Phosphate-Amine Metal-Organic Frameworks (OPA-MOFs) have been popularly employed in attempts to meet plants' needs for nitrogen, phosphorus, and iron as well as oxalate, a dianion frequently used as a phosphorus chelator in order to improve phosphorus bioavailability or as a carbon source for oxalotrophic bacteria.[101-104] In these examples, oxalate is typically the MOF structural ligand, urea acts as a structure-directing agent and nitrogen source, and iron phosphates construct the inorganic SBUs and provide the phosphates and iron. In these examples, degradation of the framework and oxalate release is reliant upon oxalotrophic bacteria that are commonly found in soil.

Alternative approaches to MOF utilization as fertilizer have also undergone query. In order to enhance the retention of phosphate anions derived from KH_2PO_4 and thereby extend the time frame of their release, Bansiwal et al. modified a zeolite-A's surface was modified with the cationic surfactant hexadecyltrimethylammonium bromide. In this case, interaction between the surface-attached surfactant and the negative phosphate anions is strong enough to undergo typical washing, heightening the confidence that the fertilizer is attached to rather than simply coexisting with the zeolite.[105] Further thoughtful examples

of alternative approaches have included a MOF-derived porous carbon that demonstrated simultaneous potassium nutrient release along with behavior as a herbicide adsorbent[106] and an Fe-BDC-EDTA MOF for slow-release iron dosage to *Phaseolus vulgaris* in an attempt to provide the necessary iron as a micronutrient for growth without overdosing and harming plant tissues.[107]

Finally, one future prospect intended for this project regards Martian CO_2 capture and release. Although the Martian atmosphere is predominantly CO_2 (roughly 96%), the total atmospheric pressure is quite low, settling around 6.36 mbar on average at the mean radius though it ranges from 1.0 mbar to 14.0 mbar depending on the given elevation and season.[108, 109] When comparing this value to Earth's average 1,013 mbar, it is clear to see that this level of pressure is far too low for a majority of plants to obtain enough CO_2 for sufficient photosynthesis.[110, 111] Aside from the atmospheric pressure, Mars also undergoes dramatic temperature swings that can extend from nighttime lows of -110 °C to daytime highs of 35 °C based upon the elevation, time of day, season, and latitude line being measured. Fortunately, gas adsorption in MOFs is often higher at lower temperature and lower at higher temperatures. By exploiting this common property of MOFs, they could feasibly be used to gather and condense CO_2 under typical Martian conditions – particularly on colder days – that may subsequently be released under warmer 'greenhouse' conditions, helping to concentrate the gas for facilitated usage in plants. In extraplanetary operations, reusability and multifunctionality is crucial and while collaborating with fellow graduate students to explore CO_2 sorptive properties of different MOFs, utilization of light-induced swing adsorption (LISA) optimize adsorption and

release, and building the testing apparatus, it could also prove fruitful to consider other, associated applications. For instance, although the lower gravity on Mars would not affect the movement of water through diffusion, it would significantly decrease the effects of advection resulting in higher water and solute retention times.[112] This could potentially mean these substances will remain available longer without sinking past a plant's reach for utilization and could be used in much lower quantities than is required with Earth's gravity. There is also a risk that this could also cause metabolic product build-up in the soil/regolith that could be detrimental to plant health. MOFs themselves would also contribute to heightened retention and slow release of water and nutrients. For these reasons, experiments are crucial to explore the potential benefits and drawbacks of this approach.

IV.2 Experimental Section

IV.2.1 Materials and Instrumentation

All reagents and solvents were commercially obtained and used as received unless otherwise specified. Commercial fertilizer used in this study was Expert Gardener brand All-Purpose Water Soluble Plant Food (24-8-16). As the instructions direct, 1 teaspoon of commercial fertilizer was dissolved in one gallon of water and stored in this form before use. Powder X-ray diffraction (PXRD) was accomplished using a Bruker D8-Focus Bragg-Brentano X-ray powder diffractometer equipped with a Cu sealed tube (λ=1.54178 Å) at 40 kV and 40 mA. Thermogravimetric analysis (TGA) was conducted using a SHIMADZU TGA-50 thermogravimetric analyzer.

IV.2.2 PCN-250 Synthesis

PCN-250 was synthesized from the preformed metal cluster ($Fe_3(\mu_3\text{-}O)(CH_3COO)_6$) using previously reported methods.[113] In short, the metal cluster was formed by first combining iron(III) nitrate nonahydrate , iron(II) nitrate , and water while stirring and then filtered. Next, a solution of sodium acetate trihydrate in water was added to the reaction vessel still stirring before once again filtering the mixture to obtain a brown precipitate. The precipitate was washed once with water and once with ethanol before being allowed to air dry. Once the cluster had been prepared and dried, about 5.100 g of the cluster were added to1.800 g 3,3',5,5'-azobenzenetetracarboxylate (ABTC) in about 6 L of DMF and 3 L mL acetic acid before being place in a sonicator to help with dissolution. The mixture was heated to 140 °C overnight. After this, stirring was halted and the reaction vessel was allowed to cool. The resulting brown crystals were filtered and washed once with DMF before final collection.

IV.2.3 Fertilizer Incorporation

Fertilizers were incorporated into as-synthetized PCN-250 powder samples using various conditions that are summarized in the table below. Note, 'fertilizer solution' was created by dissolving 1 teaspoon of Expert Gardener All-Purpose Water Soluble Plant Food in 1 gallon of water. Expert Gardener All-Purpose Water Soluble Plant Food is composed of 24.00% nitrogen (3.5% ammoniacal nitrogen and 20.5% urea nitrogen), 8.00% available phosphate (P_2O_5), 16.00% soluble potash (K_2O), 0.02% boron, 0.07%

water soluble copper, 0.15% chelated iron, 0.05% chelated manganese, 0.0005% molybdenum, 0.06% water soluble zinc. These elements were derived from ammonium sulfate, mono potassium phosphate, potassium chloride, urea, urea phosphate, boric acid, copper sulfate, iron EDTA, manganese EDTA, sodium molybdate, and zinc sulfate. After incorporation, any solution present was removed and the remaining solid was dried in an oven overnight.

Table 6. Experimental details for fertilizer loading trials into PCN-250.

Index Number	Amount of PCN-250 (mg)	Amount of Fertilizer	Method of Incorporation
1	109.3	1 mL	Soaked PCN-250 in fertilizer solution for 10 minutes
2	105.8	1 mL	Soaked PCN-250 in fertilizer solution for 1 hour
3	117.6	1 mL	Soaked PCN-250 in fertilizer solution for 2 hours
4	101.6	1 mL	Soaked PCN-250 in fertilizer solution sonicating for 1 hour
5	97.7	1 mL	Soaked PCN-250 in fertilizer solution heated to 130 $^{\circ}C$ for 1 hour
6	107.1	2 mL	Soaked PCN-250 in fertilizer solution for 1 hour
7	106.6	1 mL	Soaked PCN-250 in 40% thiourea solution for 1 hour

Table 6. Continued

Index Number	Amount of PCN-250 (mg)	Amount of Fertilizer	Method of Incorporation
8	102.6	1 mL	Soaked PCN-250 in 40% thiourea solution sonicating for 1 hour
9	104.5	1 mL	Soaked PCN-250 in 40% thiourea solution heated to 130 $^{\circ}C$ for 1 hour
10	129.6	1 mL	Soaked PCN-250 in 40% urea solution for 1 hour
11	111.5	1 mL	Soaked PCN-250 in 40% urea solution sonicating for 1 hour
12	93.3	1 mL	Soaked PCN-250 in 40% urea solution heated to 130 $^{\circ}C$ for 1 hour
13	95.6	2 mL	Soaked PCN-250 in 40% urea solution for 1 hour
14	101.2	2 mL	Soaked PCN-250 in 40% urea solution heated to 130 $^{\circ}C$ for 1 hour
15	115.6	38.0 mg	Ground PCN-250 and 40% urea together then heated to 130 $^{\circ}C$ overnight
16	157.6	38.3 mg	Ground PCN-250 and 40% urea together then added 1 mL water and heated to 130 $^{\circ}C$ overnight
17	120.6	29.8 mg	Ground PCN-250 and 40% thiourea together then heated to 130 $^{\circ}C$ overnight
18	141.9	45.6 mg	Ground PCN-250 and 40% thiourea together before adding 1 mL water and heating to 130 $^{\circ}C$ overnight

IV.2.4 PXRD

Fertilizer-incorporated PCN-250 samples were dried in an oven overnight before PXRD data were collected. These diffraction patterns were plotted with and compared against dry PCN-250 and PCN-250 that had soaked in fertilizer solution for 24 hours or against dry PCN-250 and solid urea or solid thiourea where appropriate.

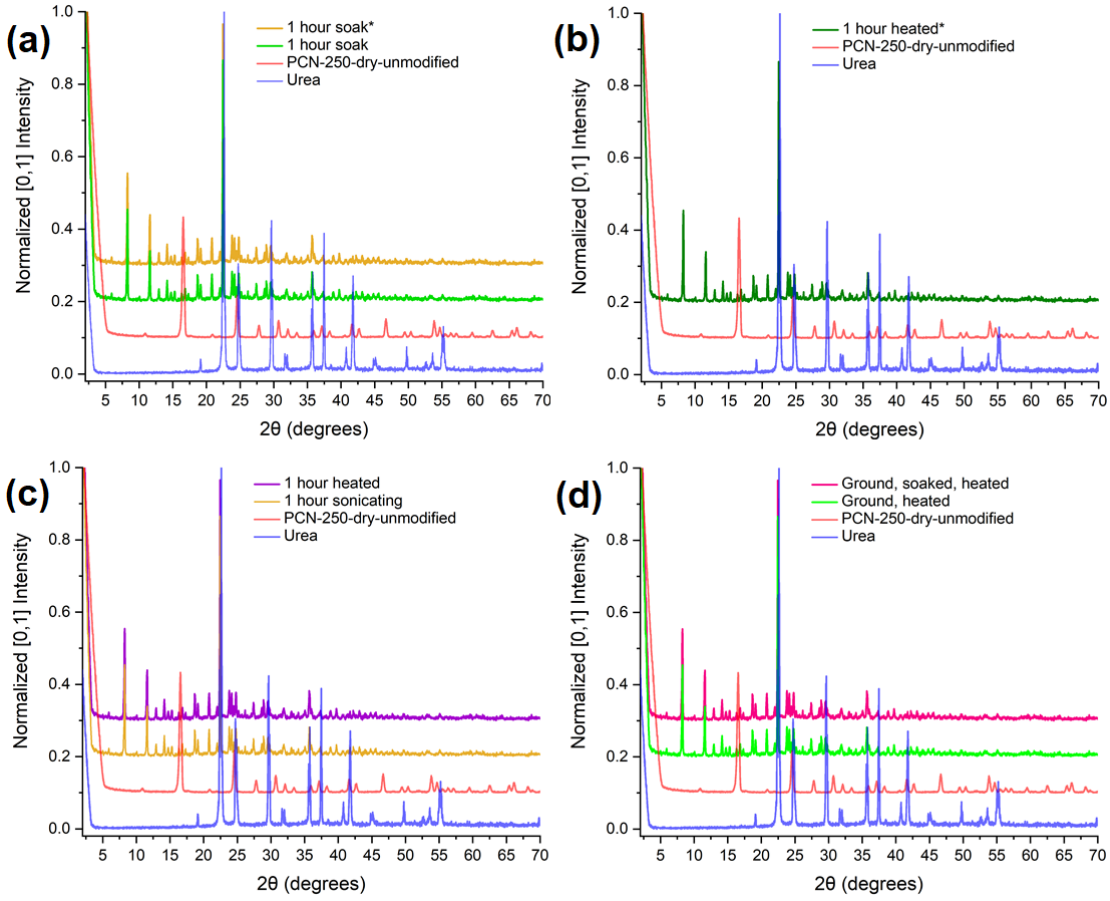

Figure 30. PXRD diffraction patterns of PCN-250 with attempted fertilizer loadings compared to unmodified, dry PCN-250 and crystalline urea. Loading conditions include combining ~100 mg PCN-250 with ~ 10 mg urea (* indicates ~ 20 mg urea) while (a) soaking in water for 1 hour, (b) heating in water for 1 hour, (c) heating in water or sonicating in water for 1 hour, and (d) ground then soaked in water and heated for 1 hour or ground then heated for 1 hour.

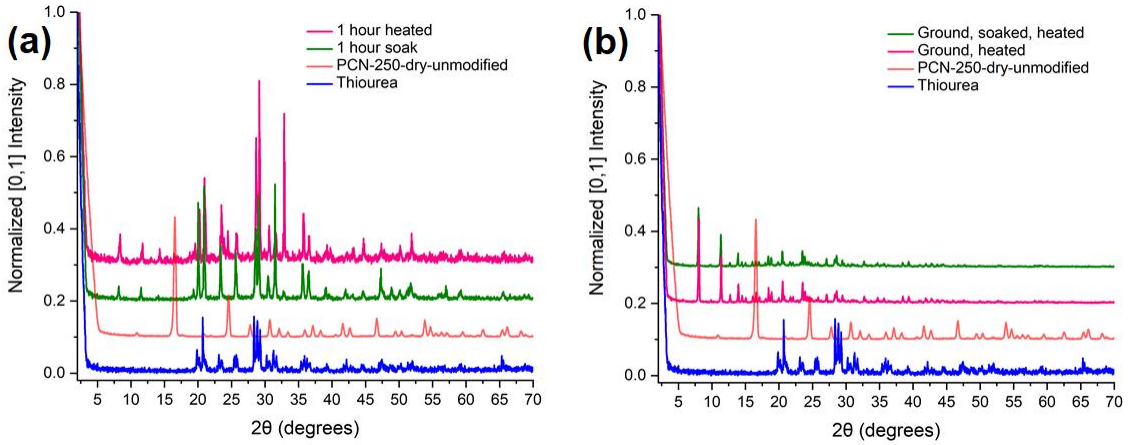

Figure 31. PXRD diffraction patterns of PCN-250 with attempted fertilizer loadings compared to unmodified, dry PCN-250 and crystalline thiourea. Loading conditions include combining ~100 mg PCN-250 with ~ 10 mg thiourea (* indicates ~ 20 mg thiourea) while (a) soaking in water or soaking in water while heating for 1 hour or (b) ground then soaked in water and heated overnight or ground then heated overnight.

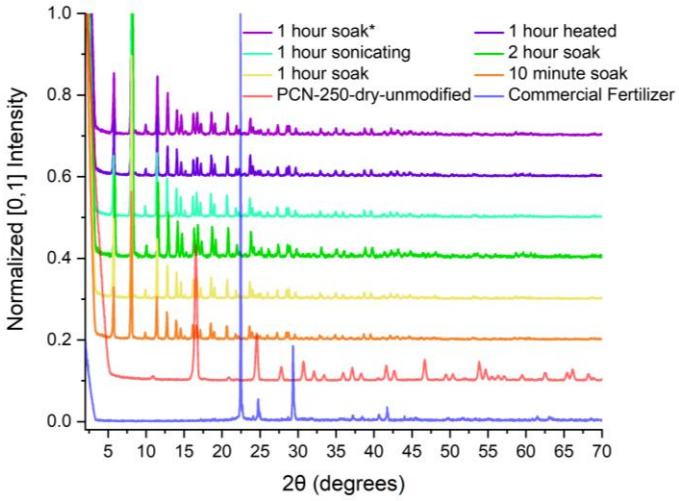

Figure 32. PXRD diffraction patterns of PCN-250 with attempted fertilizer loadings compared to unmodified, dry PCN-250 and crystalline commercial fertilizer. Loading conditions include combining ~100 mg PCN-250 with ~ 1 mL 40% commercial fertilizer (* indicates ~ 2 mL thiourea) soaking, heating, and sonicating for 10 minutes, 1 hour, or 2 hours.

IV.2.5 TGA

TGA was performed on each fertilizer-MOF sample with a heating rate of 5 ^{o}C/minute while beneath a flow of nitrogen gas.

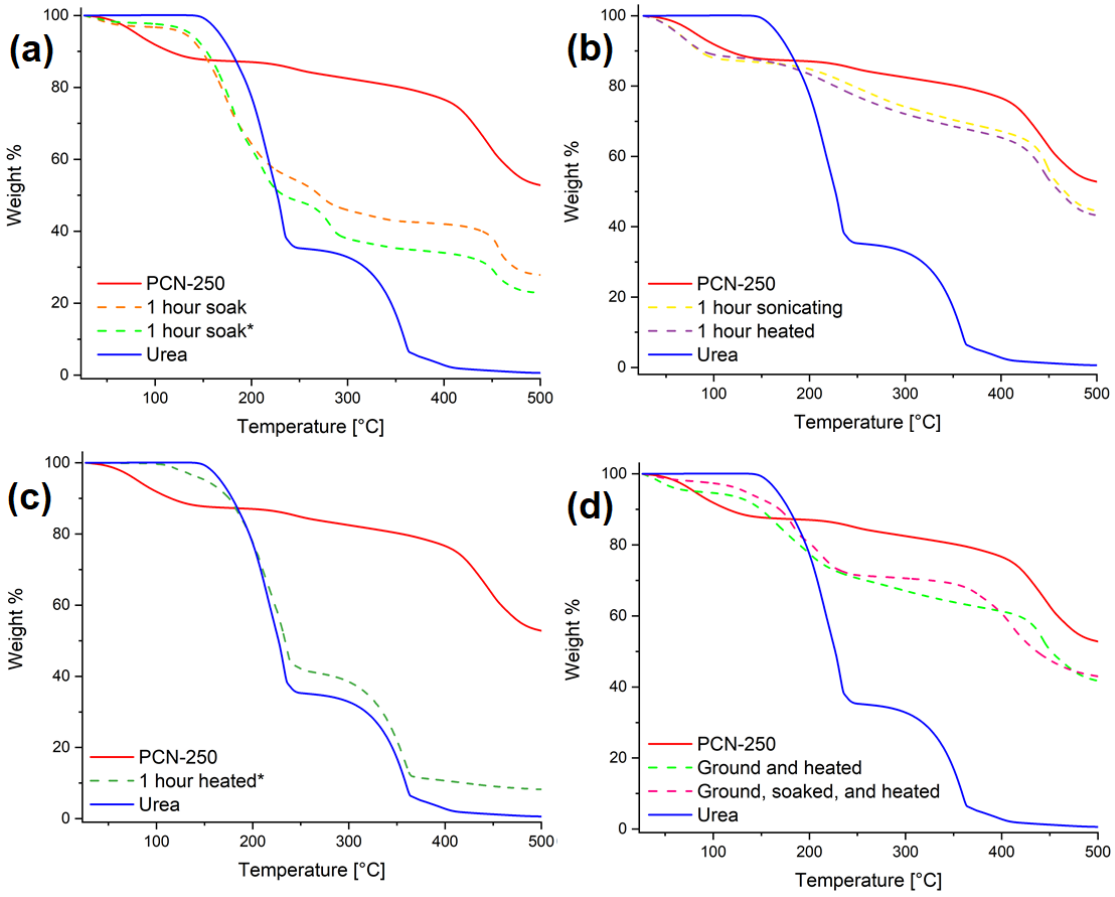

Figure 33. Thermogravimetric analysis of PCN-250 with attempted fertilizer loadings compared to unmodified, dry PCN-250 and crystalline urea. Loading conditions include combining ~100 mg PCN-250 with ~ 10 mg urea (* indicates ~ 20 mg urea) while (a) soaking in water for 1 hour, (b) heating in water for 1 hour, (c) heating in water or sonicating in water for 1 hour, and (d) ground then soaked in water and heated for 1 hour or ground then heated for 1 hour.

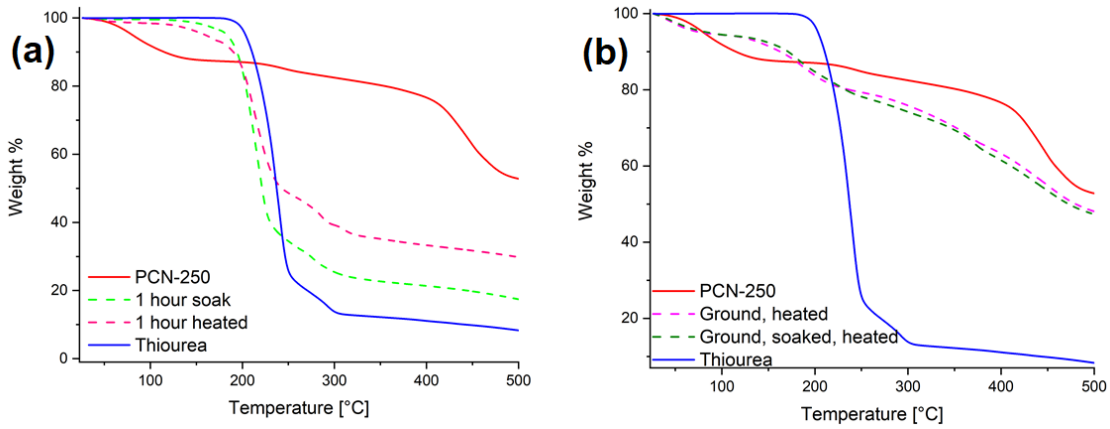

Figure 34. Thermogravimetric analysis of PCN-250 with attempted fertilizer loadings compared to unmodified, dry PCN-250 and crystalline thiourea. Loading conditions include combining ~100 mg PCN-250 with ~ 10 mg thiourea (* indicates ~ 20 mg thiourea) while (a) soaking in water or soaking in water while heating for 1 hour or (b) ground then soaked in water and heated overnight or ground then heated overnight.

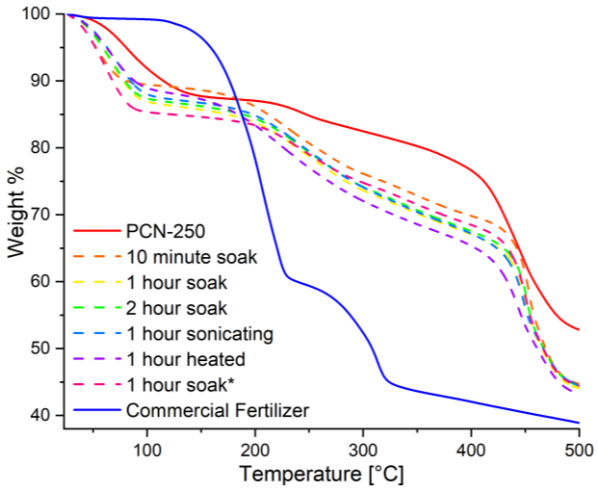

Figure 35. Thermogravimetric analysis of PCN-250 with attempted fertilizer loadings compared to unmodified, dry PCN-250 and crystalline commercial fertilizer. Loading conditions include combining ~100 mg PCN-250 with ~ 1 mL 40% commercial fertilizer (* indicates ~ 2 mL thiourea) soaking, heating, and sonicating for 10 minutes, 1 hour, or 2 hours.

IV.3 Results and Discussion

PCN-250, also referred to as MIL-127, is a **soc** network MOF comprised of Fe_3-μ_3-oxo clusters with azobenzenetetracarboxylic acid (ABTC) ligands. This MOF was selected for fertilizer loading studies for several key reasons. Firstly, PCN-250 is relatively well-studied, particularly in the Zhou group. Past studies on PCN-250 have included examination of CO_2,[114] CH_4,[26] H_2,[25] and C_2H_6[115] adsorption, the effects of water or heavy alkane doping on adsorptive properties,[114, 116, 117] phase transformations in response to applied pressures,[118] partial postsynthetic metal-metathesis at the Fe_3 clusters,[113] and differing methods of defect generation within the framework.[119] This fact may aid to eliminate surprises and simplify loading studies. Secondly, PCN-250 has demonstrated good chemical and thermal stabilities, which could help to minimize structural degredation during fertilizer loading. Third, PCN-250 has already been successfully scaled up to the kg scale and has reached commercialization, being sold through a collaboration between Strem Chemicals and framergy. Lastly, PCN-250 is ideal for Martian localized applications due to its derivation from iron, an extremely common element found in Martian regolith, as well as due to its possession of switchable azobenzene-based linkers capable of **l**ight-**i**nduced **s**wing **a**dsorption (**LISA**)[120] – an especially helpful tool when considering the drastic temperature and pressure swings inherent in the thin, poorly buffered Martian climate. In contrast to these advantages, PCN-250 exhibits no special affinity to polar molecules such as those found in typical fertilizers. Additionally, PCN-250's LISA effect has not been studied while the MOFs pores are loaded with atypical, non-solvent guest species.

The primary issue anticipated with fertilizer loading into PCN-250 related to how it could be assured that the fertilizer was properly occupying the inner spaces of the MOF rather than simply being present outside of the MOF as a mixture. This is particularly a concern when the MOF interiors are somewhat hydrophobic and the loading solvent and guest molecules are hydrophilic. Generally with MOFs, this concern is dealt with through thorough washing after incorporation, however the high solubility of the fertilizer, urea, and thiourea means even one wash could reverse any successful loading that had taken place. Therefore, particular care in verifying the successful internal loading of fertilizer is necessary. As a point of reference, Kitagawa's group published their findings on coordinative insertion of urea into MOF-74 and studied the resulting superprotonic conductivity.[121] In their study, urea was inserted into MOF-74(Mg/Ni) by mixing the activated MOF and urea at ~135 °C and washing thoroughly (10 times) with ethanol. However, because in this case urea is coordinated to the open metal sites in the MOF, such vigorous washing will likely not be appropriate for gentle loading of urea. MOF loading of other highly water-soluble salts such as $CaCl_2$, NH_4NO_3, and $LiNO_3$ have been reported, relying on solvent-free, molten salt loading techniques, without washing, or with very minimal washing.[122, 123] The strategy adopted thus required a combination of characterization techniques and multiple loading approaches.

Firstly, fertilizers urea, thiourea, and a commercial fertilizer were selected for pore encapsulation. Urea and thiourea are common components of commercial fertilizers with one difference being that urea's melting point (~135 °C) is lower than thiourea's (~182 °C) and hence more amenable to loading as a melt if less demanding methods prove

unsuccessful. The incorporation methods attempted are described in **Table 6** and are summarized briefly. Briefly, a dried sample of about 100 mg PCN-250 was combined with either 0 mL, 1 mL, or 2 mL commercial fertilizer solution, 40% urea solution, or 40% thiourea solution. Samples were either left to soak at room temperature, with sonication, or with heating for 10 minutes to 2 hours. After the allotted time, solution was removed from the samples and MOFs were placed in an oven to dry overnight. PXRD patterns were first taken of each sample. Proper loading would be indicated by a powder pattern that retains peaks for the MOF while not including peaks for the fertilizer. This is because as the fertilizer is implanted into the MOF pores, its typical long-range order is believed to be lost and is unlikely to appear in a powder xray pattern. However, it is conceivable that introduction of fertilizer salts could slightly contract the framework and so shifting of peaks is not out of the question. The sample with index number **14** (2 hour soak, 2 mL 40% urea solution, heated to 130 °C) does not show signal expected from the crystalline MOF sample, indicating that the MOF has either decomposed or, more likely, that the salt signal is overwhelming the MOF signal and so the salt is not loaded regardless. Samples **11** (1 hour soak, 1 mL 40% urea solution, sonicating) and **12**'s (1 hour soak, 1 mL 40% urea solution, heated to 130 °C) patterns are also dominated by fertilizer signal although the presence of PCN-250 cannot be ruled out from their PXRD patterns alone. All other spectra either show purely PCN-250 (whether in its typical phase or mixed with some amount of PCN-250' or PCN-250" phase)[118] or a reasonable mixture of PCN-250 and fertilizer. For further investigation of fertilizer loading, TGA was performed on each sample and compared with the TGA plots for unmodified PCN-250 as well as the

appropriate fertilizer. Samples with index numbers **5** (1 hour soak, 1 mL 0.13% v/v fertilizer solution, heated to 130 °C), **10** (1 hour soak, 1 mL 40% urea solution), **13** (1 hour soak, 2 mL 40% urea solution), **15** (38.0 mg urea, ground, heated overnight at 130 °C), **16** (38.3 mg urea, ground, heated overnight in 1 mL water at 130 °C), **17** (29.8 mg thiourea, ground, heated overnight at 130 °C), and **18** (45.6 mg thiourea, ground, heated overnight in 1 mL water at 130 °C) appear to be most promising through inspection of their TGA curves which appear to possess the characteristic peaks similar to both PCN-250 and fertilizer or sit well in between the two.

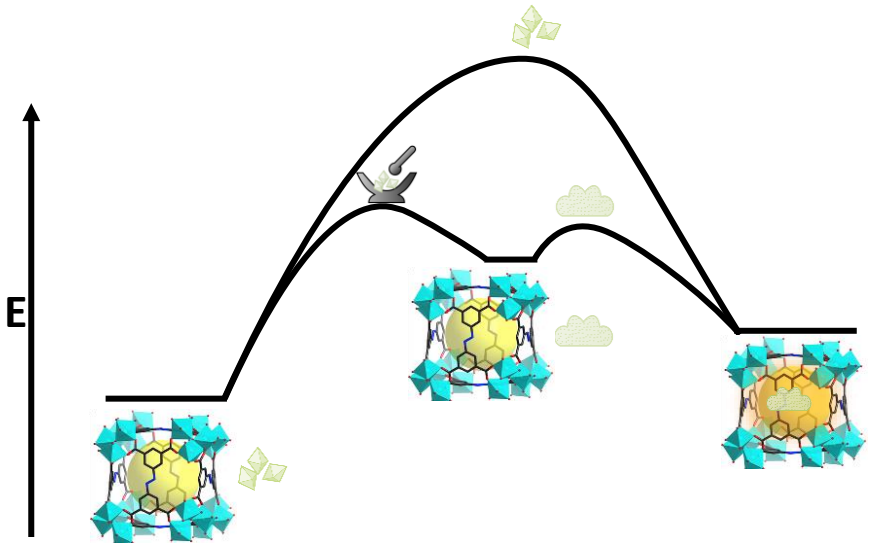

Figure 36. A simplified reaction coordinate featuring PCN-250 and crystalline fertilizer guest on the left and fertilizer-loaded PCN-250 on the right. Experiments suggest that while loading is possible through simple soaking with crystalline fertilizer, loading is much more favorable when a two step process is adopted: grinding followed by heating of the two species together.

These experiments have produced a few trends to notice. (1) Non-coordinative fertilizer loading appears to be somewhat fruitful by means slow diffusion into the MOF

framework, aka through simple soaking. (2) Excessive agitation of the preliminary solution of MOF and fertilizer such as by methods which make use of sonication or heating in water result in poor fertilizer loading. This may be a result of constant disruption of the weak van der Waals forces which hold the guest molecules within the framework and the provided energy may translate into recrystallization of the fertilizer molecules. (3) Preliminary grinding of samples appears to yield the most promising loading of fertilizer. It is possible that mechanical grinding helps fertilizer dissolve and therefore promoting the first step to pore encapsulation. Grinding may reduce what could have been a single, large activation energy barrier to incapsulation into two, more manageable activation energy barriers, represented schematically in **Figure 36**.

CHAPTER V

SUMMARY AND FUTURE OUTLOOK

In this dissertation work, the pore environments of metal-organic frameworks were studied in order to further uncover the rules that dictate the thermodynamics of secondary linker insertion, to understand the potential consequences of linker symmetry reduction to porosity and stability depending upon the symmetry of the metal cluster employed, and to inquire as to which conditions urea, thiourea, and commercial fertilizer will or will not be loaded within the pores of an iron-based MOF, PCN-250. In Chapter II it was determined that even slight differences in linker length and bulk can have dramatically different temperature requirements for insertion. The crystal structures before and after linker insertion, especially the pore volumes and axial lengths, were carefully analyzed in order to draw conclusions regarding the process of insertion. Chapter III uncovered novel structural outcomes of linker symmetry reduction when the connectivity of the metal-cluster was varied. The novel mesoporous MOF obtained, whose mesopores are encircled by alternating stereoisomeric cages, was then strengthened through metal exchange from iron to chromium. In Chapter IV, the non-coordinative loading of various fertilizers, urea, thiourea, and a commercial fertilizer, was attempted in PCN-240, an iron-based MOF, and loading success was analyzed by means of a combination of TGA and PXRD. It was concluded that grinding samples before heat treatment yielded the most fruitful loading results as compared to soaking, sonicating, and heating samples without preliminary grinding. With the enhanced degree of tunability, be it through adjustments to the metal

structural unit, the organic ligand, physical and chemical pore properties, synthetic conditions, and post-synthetic modification, there is also an inevitable complication to the predictability of MOF structures. The work described herein are advancements towards simplifying our understanding of pore-engineering and post-synthetic modifications in metal-organic frameworks with the ultimate goal of moving toward more planned and precise structural regulation.

Future studies that would be beneficial to this goal and build upon the research herein include an exploration of the precise contributions that flexible MOFs deliver compared to the variations in secondary linker conformation that may occur during the process of post-synthetic linker installation. Additionally, after discovering the differences in consequence between linker symmetry reduction between 8-connected Zr_6 cluster-based MOFs and 6-connected Fe_3-μ_3-oxo clusters, a reasonable next step would concern the study of a similar linker symmetry reduction strategy with other metal clusters such as paddlewheel units and single metal sites. Lastly, in order to employ and expand lessons regarding fertilizer guest loading into PCN-250, follow-up studies aught consider the differences in loading obtained by utilizing other common solvents and other individual fertilizer components as well as monitoring PCN-250's aptitude to act as a slow-release fertilizer by employing UV-Vis spectroscopy.

REFERENCES

1. Yaghi, O. M.; O'Keeffe, M.; Ockwig, N. W.; Chae, H. K.; Eddaoudi, M.; Kim, J., Reticular synthesis and the design of new materials. *Nature* **2003,** *423*, 705-714.

2. Lollar, C. T.; Pang, J.; Qin, J.-s.; Yuan, S.; Powell, J. A.; Zhou, H.-C., Thermodynamically Controlled Linker Installation in Flexible Zirconium Metal–Organic Frameworks. *Crystal Growth & Design* **2019,** *19* (4), 2069-2073.

3. Li, H.; Wang, K.; Sun, Y.; Lollar, C. T.; Li, J.; Zhou, H.-C., Recent advances in gas storage and separation using metal-organic frameworks. *Mater. Today* **2018,** *21* (2), 108-121.

4. Lollar, C. T.; Banerjee, S.; Xiao, Z.; Fang, Y.; Zhou, H.-C., Biomedical Integration of Metal-Organic Frameworks. *Trends Chem.* **2020**.

5. Feng, M.; Zhang, P.; Zhou, H.-C.; Sharma, V. K., Water-stable metal-organic frameworks for aqueous removal of heavy metals and radionuclides: A review. *Chemosphere* **2018,** *209*, 783-800.

6. Wang, P. L.; Xie, L. H.; Joseph, E. A.; Li, J. R.; Su, X. O.; Zhou, H. C., Metal-Organic Frameworks for Food Safety. *Chem Rev* **2019,** *119* (18), 10638-10690.

7. Yuan, S.; Feng, L.; Wang, K.; Pang, J.; Bosch, M.; Lollar, C.; Sun, Y.; Qin, J.; Yang, X.; Zhang, P.; Wang, Q.; Zou, L.; Zhang, Y.; Zhang, L.; Fang, Y.; Li, J.; Zhou, H. C., Stable Metal-Organic Frameworks: Design, Synthesis, and Applications. *Adv Mater* **2018,** *30* (37), e1704303.

8. Zhang, J.; Chen, J.; Peng, S.; Peng, S.; Zhang, Z.; Tong, Y.; Miller, P. W.; Yan, X. P., Emerging porous materials in confined spaces: from chromatographic applications to flow chemistry. *Chem Soc Rev* **2019,** *48* (9), 2566-2595.

9. Yang, X. Y.; Chen, L. H.; Li, Y.; Rooke, J. C.; Sanchez, C.; Su, B. L., Hierarchically porous materials: synthesis strategies and structure design. *Chem Soc Rev* **2017,** *46* (2), 481-558.

10. Thompson, B. R.; Horozov, T. S.; Stoyanov, S. D.; Paunov, V. N., Hierarchically structured composites and porous materials from soft templates: fabrication and applications. *Journal of Materials Chemistry A* **2019,** *7* (14), 8030-8049.

11. Boucher, E. A., Porous materials: structure, properties and capillary phenomena. *J. Mater. Sci.* **1976,** *11*, 1734-1750.

12. Batten, S. R.; Champness, N. R.; Chen, X.-M.; Garcia-Martinez, J.; Kitagawa, S.; Öhrström, L.; O'Keeffe, M.; Suh, M. P.; Reedijk, J., Coordination polymers, metal–organic frameworks and the need for terminology guidelines. *CrystEngComm* **2012,** *14* (9).

13. Batten, S. R.; Champness, N. R.; Chen, X.-M.; Garcia-Martinez, J.; Kitagawa, S.; Öhrström, L.; O'Keeffe, M.; Paik Suh, M.; Reedijk, J., Terminology of metal–organic frameworks and coordination polymers (IUPAC Recommendations 2013). *Pure and Applied Chemistry* **2013,** *85* (8), 1715-1724.

14. Zhang, S. Y.; Jensen, S.; Tan, K.; Wojtas, L.; Roveto, M.; Cure, J.; Thonhauser, T.; Chabal, Y. J.; Zaworotko, M. J., Modulation of Water Vapor Sorption

by a Fourth-Generation Metal-Organic Material with a Rigid Framework and Self-Switching Pores. *J Am Chem Soc* **2018,** *140* (39), 12545-12552.

15. Butova, V. V.; Soldatov, M. A.; Guda, A. A.; Lomachenko, K. A.; Lamberti, C., Metal-organic frameworks: structure, properties, methods of synthesis and characterization. *Russian Chemical Reviews* **2016,** *85* (3), 280-307.

16. Howarth, A. J.; Peters, A. W.; Vermeulen, N. A.; Wang, T. C.; Hupp, J. T.; Farha, O. K., Best Practices for the Synthesis, Activation, and Characterization of Metal–Organic Frameworks. *Chemistry of Materials* **2016,** *29* (1), 26-39.

17. Thommes, M.; Kaneko, K.; Neimark, A. V.; Olivier, J. P.; Rodriguez-Reinoso, F.; Rouquerol, J.; Sing, K. S. W., Physisorption of gases, with special reference to the evaluation of surface area and pore size distribution (IUPAC Technical Report). *Pure and Applied Chemistry* **2015,** *87* (9-10), 1051-1069.

18. Ambroz, F.; Macdonald, T. J.; Martis, V.; Parkin, I. P., Evaluation of the BET Theory for the Characterization of Meso and Microporous MOFs. *Small Methods* **2018,** *2* (11).

19. Gelfand, B. S.; Shimizu, G. K., Parameterizing and grading hydrolytic stability in metal-organic frameworks. *Dalton Trans* **2016,** *45* (9), 3668-78.

20. Oien-Odegaard, S.; Shearer, G. C.; Wragg, D. S.; Lillerud, K. P., Pitfalls in metal-organic framework crystallography: towards more accurate crystal structures. *Chem Soc Rev* **2017,** *46* (16), 4867-4876.

21. Ionin, B. I.; Ershov, B. A., *NMR Spectroscopy in Organic Chemistry*. Plenum Press: New York, 1970.

22. Jacobsen, N. E., *NMR Spectroscopy Explained: Simplified Theory, Applications and Examples for Organic Chemistry and Structural Biology*. John Wiley & Sons, Inc.: Hoboken, New Jersey, 2007.

23. Bedia, J.; Muelas-Ramos, V.; Peñas-Garzón, M.; Gómez-Avilés, A.; Rodríguez, J. J.; Belver, C., A Review on the Synthesis and Characterization of Metal Organic Frameworks for Photocatalytic Water Purification. *Catalysts* **2019,** *9* (1).

24. Suga, M.; Asahina, S.; Sakuda, Y.; Kazumori, H.; Nishiyama, H.; Nokuo, T.; Alfredsson, V.; Kjellman, T.; Stevens, S. M.; Cho, H. S.; Cho, M.; Han, L.; Che, S.; Anderson, M. W.; Schüth, F.; Deng, H.; Yaghi, O. M.; Liu, Z.; Jeong, H. Y.; Stein, A.; Sakamoto, K.; Ryoo, R.; Terasaki, O., Recent progress in scanning electron microscopy for the characterization of fine structural details of nano materials. *Progress in Solid State Chemistry* **2014,** *42* (1-2), 1-21.

25. Suh, M. P.; Park, H. J.; Prasad, T. K.; Lim, D. W., Hydrogen storage in metal-organic frameworks. *Chem Rev* **2012,** *112* (2), 782-835.

26. He, Y.; Zhou, W.; Qian, G.; Chen, B., Methane storage in metal-organic frameworks. *Chem Soc Rev* **2014,** *43* (16), 5657-78.

27. Mason, J. A.; Veenstra, M.; Long, J. R., Evaluating metal–organic frameworks for natural gas storage. *Chem. Sci.* **2014,** *5* (1), 32-51.

28. Sumida, K.; Rogow, D. L.; Mason, J. A.; McDonald, T. M.; Bloch, E. D.; Herm, Z. R.; Bae, T. H.; Long, J. R., Carbon dioxide capture in metal-organic frameworks. *Chem Rev* **2012,** *112* (2), 724-81.

29. Lee, K.; Howe, J. D.; Lin, L.-C.; Smit, B.; Neaton, J. B., Small-Molecule Adsorption in Open-Site Metal–Organic Frameworks: A Systematic Density Functional Theory Study for Rational Design. *Chemistry of Materials* **2015,** *27* (3), 668-678.

30. Li, B.; Chrzanowski, M.; Zhang, Y.; Ma, S., Applications of metal-organic frameworks featuring multi-functional sites. *Coordination Chemistry Reviews* **2016,** *307*, 106-129.

31. Kumar, P.; Deep, A.; Kim, K.-H., Metal organic frameworks for sensing applications. *TrAC Trends in Analytical Chemistry* **2015,** *73*, 39-53.

32. Kreno, L. E.; Leong, K.; Farha, O. K.; Allendorf, M.; Van Duyne, R. P.; Hupp, J. T., Metal-organic framework materials as chemical sensors. *Chem Rev* **2012,** *112* (2), 1105-25.

33. Yang, D.; Gates, B. C., Catalysis by Metal Organic Frameworks: Perspective and Suggestions for Future Research. *ACS Catalysis* **2019,** *9* (3), 1779-1798.

34. Furukawa, H.; Cordova, K. E.; O'Keeffe, M.; Yaghi, O. M., The chemistry and applications of metal-organic frameworks. *Science* **2013,** *341* (6149), 1230444.

35. Liu, J.; Chen, L.; Cui, H.; Zhang, J.; Zhang, L.; Su, C. Y., Applications of metal-organic frameworks in heterogeneous supramolecular catalysis. *Chem Soc Rev* **2014,** *43* (16), 6011-61.

36. Gu, Z.-Y.; Park, J.; Raiff, A.; Wei, Z.; Zhou, H.-C., Metal-Organic Frameworks as Biomimetic Catalysts. *ChemCatChem* **2014,** *6* (1), 67-75.

37. Zhang, M.; Gu, Z.-Y.; Bosch, M.; Perry, Z.; Zhou, H.-C., Biomimicry in metal–organic materials. *Coordination Chemistry Reviews* **2015,** *293-294*, 327-356.

38. Lian, X.; Fang, Y.; Joseph, E.; Wang, Q.; Li, J.; Banerjee, S.; Lollar, C.; Wang, X.; Zhou, H. C., Enzyme-MOF (metal-organic framework) composites. *Chem Soc Rev* **2017,** *46* (11), 3386-3401.

39. Lian, X.; Huang, Y.; Zhu, Y.; Fang, Y.; Zhao, R.; Joseph, E.; Li, J.; Pellois, J. P.; Zhou, H. C., Enzyme-MOF Nanoreactor Activates Nontoxic Paracetamol for Cancer Therapy. *Angew Chem Int Ed Engl* **2018,** *57* (20), 5725-5730.

40. Carrillo-Carrion, C.; Martinez, R.; Navarro Poupard, M. F.; Pelaz, B.; Polo, E.; Arenas-Vivo, A.; Olgiati, A.; Taboada, P.; Soliman, M. G.; Catalan, U.; Fernandez-Castillejo, S.; Sola, R.; Parak, W. J.; Horcajada, P.; Alvarez-Puebla, R. A.; Del Pino, P., Aqueous Stable Gold Nanostar/ZIF-8 Nanocomposites for Light-Triggered Release of Active Cargo Inside Living Cells. *Angew Chem Int Ed Engl* **2019,** *58* (21), 7078-7082.

41. Sharma, S.; Mittal, D.; Verma, A. K.; Roy, I., Copper-Gallic Acid Nanoscale Metal–Organic Framework for Combined Drug Delivery and Photodynamic Therapy. *ACS Applied Bio Materials* **2019**.

42. Jiang, K.; Zhang, L.; Hu, Q.; Zhao, D.; Xia, T.; Lin, W.; Yang, Y.; Cui, Y.; Yang, Y.; Qian, G., Pressure controlled drug release in a Zr-cluster-based MOF. *Journal of Materials Chemistry B* **2016,** *4* (39), 6398-6401.

43. Fang, J.; Yang, Y.; Xiao, W.; Zheng, B.; Lv, Y. B.; Liu, X. L.; Ding, J., Extremely low frequency alternating magnetic field-triggered and MRI-traced drug delivery by optimized magnetic zeolitic imidazolate framework-90 nanoparticles. *Nanoscale* **2016,** *8* (6), 3259-63.

44. Samanta, D.; Roy, S.; Sasmal, R.; Saha, N. D.; K, R. P.; Viswanatha, R.; Agasti, S. S.; Maji, T. K., Solvent Adaptive Dynamic Metal-Organic Soft Hybrid for Imaging and Biological Delivery. *Angew Chem Int Ed Engl* **2019,** *58* (15), 5008-5012.

45. Peng, S.; Bie, B.; Sun, Y.; Liu, M.; Cong, H.; Zhou, W.; Xia, Y.; Tang, H.; Deng, H.; Zhou, X., Metal-organic frameworks for precise inclusion of single-stranded DNA and transfection in immune cells. *Nat Commun* **2018,** *9* (1), 1293.

46. Zhu, W.; Guo, J.; Agola, J. O.; Croissant, J. G.; Wang, Z.; Shang, J.; Coker, E.; Motevalli, B.; Zimpel, A.; Wuttke, S.; Brinker, C. J., Metal-Organic Framework Nanoparticle-Assisted Cryopreservation of Red Blood Cells. *J Am Chem Soc* **2019,** *141* (19), 7789-7796.

47. Rojas, S.; Baati, T.; Njim, L.; Manchego, L.; Neffati, F.; Abdeljelil, N.; Saguem, S.; Serre, C.; Najjar, M. F.; Zakhama, A.; Horcajada, P., Metal-Organic Frameworks as Efficient Oral Detoxifying Agents. *J Am Chem Soc* **2018,** *140* (30), 9581-9586.

48. Kato, S.; Otake, K. I.; Chen, H.; Akpinar, I.; Buru, C. T.; Islamoglu, T.; Snurr, R. Q.; Farha, O. K., Zirconium-Based Metal-Organic Frameworks for the Removal of Protein-Bound Uremic Toxin from Human Serum Albumin. *J Am Chem Soc* **2019,** *141* (6), 2568-2576.

49. Klinowski, J.; Paz, F. A.; Silva, P.; Rocha, J., Microwave-assisted synthesis of metal-organic frameworks. *Dalton Trans* **2011,** *40* (2), 321-30.

50. Khan, N. A.; Jhung, S. H., Synthesis of metal-organic frameworks (MOFs) with microwave or ultrasound: Rapid reaction, phase-selectivity, and size reduction. *Corodination Chemistry Reviews* **2015,** *2015* (285), 11-23.

51. Vaitsis, C.; Sourkouni, G.; Argirusis, C., Metal Organic Frameworks (MOFs) and ultrasound: A review. *Ultrasonics - Sonochemistry* **2019,** *52*, 106-119.

52. Al-Kutubi, H.; Gascon, J.; Sudhölter, E. J. R.; Rassaei, L., Electrosynthesis of Metal-Organic Frameworks: Challenges and Opportunities. *ChemElectroChem* **2015,** *2* (4), 462-474.

53. Li, W.-J.; Tu, M.; Cao, R.; Fischer, R. A., Metal-organic framework thin films: electrochemical fabrication techniques and corresponding applications and perspectives. *Journal of Materials Chemistry A* **2016,** *4*, 12356-12369.

54. Martinez Joaristi, A.; Juan-Alcañiz, J.; Serra-Crespo, P.; Kapteijn, F.; Gascon, J., Electrochemical Synthesis of Some Archetypical Zn2+, Cu2+, and Al3+Metal Organic Frameworks. *Crystal Growth & Design* **2012,** *12* (7), 3489-3498.

55. Chen, D.; Zhao, J.; Zhang, P.; Dai, S., Mechanochemical synthesis of metal–organic frameworks. *Polyhedron* **2019,** *162*, 59-64.

56. Andre, V.; Quaresma, S.; da Silva, J. L. F.; Duarte, M. T., Exploring mechanochemistry to turn organic bio-relevant molecules into metal-organic frameworks: a short review. *Beilstein J Org Chem* **2017,** *13*, 2416-2427.

57. Lollar, C. T.; Qin, J. S.; Pang, J.; Yuan, S.; Becker, B.; Zhou, H. C., Interior Decoration of Stable Metal-Organic Frameworks. *Langmuir* **2018,** *34* (46), 13795-13807.

58. Yin, Z.; Wan, S.; Yang, J.; Kurmoo, M.; Zeng, M.-H., Recent advances in post-synthetic modification of metal-organic frameworks: New types and tandem reactions. *Coordination Chemistry Reviews* **2019,** *378*, 500-512.

59. Tanabe, K. K.; Cohen, S. M., Postsynthetic modification of metal-organic frameworks--a progress report. *Chem Soc Rev* **2011,** *40* (2), 498-519.

60. Chemical Crystallography at the ALS. http://chemcryst.lbl.gov/home (accessed January 11th, 2020).

61. Pang, J.; Yuan, S.; Du, D.; Lollar, C.; Zhang, L.; Wu, M.; Yuan, D.; Zhou, H. C.; Hong, M., Flexible Zirconium MOFs as Bromine-Nanocontainers for Bromination Reactions under Ambient Conditions. *Angew Chem Int Ed Engl* **2017,** *56* (46), 14622-14626.

62. Deng, H.; Grunder, S.; Cordova, K. E.; Valente, C.; Furukawa, H.; Hmadeh, M.; Gandara, F.; Whalley, A. C.; Liu, Z.; Asahina, S.; Kazumori, H.; O'Keeffe, M.; Terasaki, O.; Stoddart, J. F.; Yaghi, O. M., Large-Pore Apertures in a Series of Metal-Organic Frameworks. *Science* **2012,** *336*, 1018-1023.

63. Tranchemontagne, D. J.; Park, K. S.; Furukawa, H.; Eckert, J.; Knobler, C. B.; Yaghi, O. M., Hydrogen Storage in New Metal–Organic Frameworks. *The Journal of Physical Chemistry C* **2012,** *116* (24), 13143-13151.

64. Hunt, S. J.; Cliffe, M. J.; Hill, J. A.; Cairns, A. B.; Funnell, N. P.; Goodwin, A. L., Flexibility transition and guest-driven reconstruction in a ferroelastic metal-organic framework. *CrystEngComm* **2015,** *17*, 361-369.

65. Pang, J.; Yuan, S.; Qin, J.; Liu, C.; Lollar, C.; Wu, M.; Yuan, D.; Zhou, H. C.; Hong, M., Control the Structure of Zr-Tetracarboxylate Frameworks through Steric Tuning. *J Am Chem Soc* **2017,** *139* (46), 16939-16945.

66. Ortiz, A. U.; Boutin, A.; Fuchs, A. H.; Coudert, F. X., Metal-organic frameworks with wine-rack motif: what determines their flexibility and elastic properties? *J Chem Phys* **2013,** *138* (17), 174703.

67. Redfern, L. R.; Farha, O. K., Mechanical properties of metal–organic frameworks. *Chemical Science* **2019,** *10* (46), 10666-10679.

68. Ding, M.; Cai, X.; Jiang, H.-L., Improving MOF stability: approaches and applications. *Chemical Science* **2019,** *10* (44), 10209-10230.

69. Li, J.-R.; Sculley, J.; Zhou, H.-C., Metal-Organic Frameworks for Separations. *Chem. Rev.* **2011,** *112*, 869-932.

70. Banerjee, D.; Simon, C. M.; Plonka, A. M.; Motkuri, R. K.; Liu, J.; Chen, X.; Smit, B.; Parise, J. B.; Haranczyk, M.; Thallapally, P. K., Metal-organic framework with optimally selective xenon adsorption and separation. *Nature Communications* **2016,** *7*, 11831-11838.

71. Ramaswamy, P.; Wong, N. E.; Shimizu, G. K., MOFs as proton conductors--challenges and opportunities. *Chem Soc Rev* **2014,** *43* (16), 5913-32.

72. Eddaoudi, M.; Kim, J.; Rosi, N.; Vodak, D.; Wachter, J.; O'Keeffe, M.; Yaghi, O. M., Systematic Design of Pore Size and Functionality in Isoreticular MOFs and Their Application in Methane Storage. *Science* **2002,** *295* (5554), 469-472.

73. Wang, K.; Lv, X. L.; Feng, D.; Li, J.; Chen, S.; Sun, J.; Song, L.; Xie, Y.; Li, J. R.; Zhou, H. C., Pyrazolate-Based Porphyrinic Metal-Organic Framework with Extraordinary Base-Resistance. *J Am Chem Soc* **2016,** *138* (3), 914-9.

74. Bosch, M.; Zhang, M.; Zhou, H.-C., Increasing the Stability of Metal-Organic Frameworks. *Advances in Chemistry* **2014,** *2014*, 1-8.

75. Burtch, N. C.; Jasuja, H.; Walton, K. S., Water stability and adsorption in metal-organic frameworks. *Chem Rev* **2014,** *114* (20), 10575-612.

76. Pearson, R. G., Hard and Soft Acids and Bases. *J Am Chem Soc* **1963,** *85* (22), 3533-3539.

77. Feng, D.; Wang, K.; Wei, Z.; Chen, Y. P.; Simon, C. M.; Arvapally, R. K.; Martin, R. L.; Bosch, M.; Liu, T. F.; Fordham, S.; Yuan, D.; Omary, M. A.; Haranczyk, M.; Smit, B.; Zhou, H. C., Kinetically tuned dimensional augmentation as a versatile synthetic route towards robust metal-organic frameworks. *Nat Commun* **2014,** *5*, 5723.

78. Barnard, R. A.; Dutta, A.; Schnobrich, J. K.; Morrison, C. N.; Ahn, S.; Matzger, A. J., Two-dimensional crystals from reduced symmetry analogues of trimesic acid. *Chemistry* **2015,** *21* (15), 5954-61.

79. Dutta, A.; Ma, J.; Wong-Foy, A. G.; Matzger, A. J., A non-regular layer arrangement of a pillared-layer coordination polymer: avoiding interpenetration via symmetry breaking at nodes. *Chem Commun (Camb)* **2015,** *51* (71), 13611-4.

80. Pang, J.; Yuan, S.; Qin, J.; Wu, M.; Lollar, C. T.; Li, J.; Huang, N.; Li, B.; Zhang, P.; Zhou, H. C., Enhancing Pore-Environment Complexity Using a Trapezoidal

Linker: Toward Stepwise Assembly of Multivariate Quinary Metal-Organic Frameworks. *J Am Chem Soc* **2018,** *140* (39), 12328-12332.

81. Schaate, A.; Roy, P.; Godt, A.; Lippke, J.; Waltz, F.; Wiebcke, M.; Behrens, P., Modulated synthesis of Zr-based metal-organic frameworks: from nano to single crystals. *Chemistry* **2011,** *17* (24), 6643-51.

82. Wisemann, G.; Schaate, A.; Lilienthal, S.; Bremer, I.; Schneider, A. M.; Behrens, P., Modulated synthesis of Zr-fumarate MOF. *Microporous and Mesoporous Materials* **2012,** *152*, 64-70.

83. Tsuruoka, T.; Furukawa, S.; Takashima, Y.; Yoshida, K.; Isoda, S.; Kitagawa, S., Nanoporous nanorods fabricated by coordination modulation and oriented attachment growth. *Angew Chem Int Ed Engl* **2009,** *48* (26), 4739-43.

84. World Fertilizer Trends and Outlook 2022. FAO, Ed. Food & Agriculture Organization of United Nations: Rome, 2019.

85. *More people, more food, worse water? a global review of water pollution from agriculture*. the Food and Agriculture Organization of the United Nations and the International Water Management Institute on behalf of the Water Land and Ecosystems research program of the CGIAR: Rome and Colombo, 2018.

86. Hart, M. R.; Quinn, B. F.; Nguyen, M. L., Phosphorus Runoff from Agricultural Land and Direct Fertilizer Effects: A Review. *J. Environ. Qual.* **2004,** *33*, 1954-1972.

87. Savci, S., An Agricultural Pollutant: Chemical Fertilizer. *International Journal of Environmental Science and Development* **2012,** *3*, 77-80.

88. Zhu, Z. L.; Chen, D. L., Nitrogen fertilizer use in China – Contributions to food production, impacts on the environment and best management strategies. *Nutrient Cycling in Agroecosystems* **2002,** *63*, 117-127.

89. Niu, G.; Cabrera, R. I., Growth and Physiological Responses of Landscape Plants to Saline Water Irrigation: A Review. *HortScience* **2010,** *45* (11), 1605-1609.

90. Wu, L.; Guo, X.; Harivandi, A., Salt Tolerance and Salt Accumulation of Landscape Plants Irrigated by Sprinkler and Drip Irrigation Systems. *Journal of Plant Nutrition* **2001,** *24* (9), 1473-1490.

91. Helmers, M. J.; Isenhart, T.; Dosskey, M.; Dabney, S.; Strock, J., Buffers and Vegetative Filter Strips. In *Final Report: Gulf Hypoxia and Local Water Quality Concerns Workshop*, American Society of Agricultural and Biological Engineers: St. Joseph, MI, 2008; pp 43-58.

92. Ramli, R. A., Slow release fertilizer hydrogels: a review. *Polymer Chemistry* **2019,** *10*, 6073-6090.

93. Milani, P.; Franca, D.; Balieiro, A. G.; Faez, R., Polymers and its applications in agriculture. *Polimeros* **2017,** *27* (3), 256-266.

94. Sempeho, S. I.; Kim, H. T.; Mubofu, E.; Hilonga, A., Meticulous Overview on the Controlled Release Fertilizers. *Advances in Chemistry* **2014,** *2014*.

95. Azeem, B.; KuShaari, K.; Man, Z. B.; Basit, A.; Thanh, T. H., Review on materials & methods to produce controlled release coated urea fertilizer. *Journal of Controlled Release* **2014,** *181*, 11-21.

96. Sarkar, D. J.; Singh, A.; Mandal, P.; Kumar, A.; Parmar, B. S., Synthesis and Characterization of Poly(CMC-g-cl-PAam/Zeolite) Superabsorbent Composites for Controlled Delivery of Zinc Micronutrient: Swelling and Release Behavior. *Polymer-Plastics Technology and Engineering* **2014,** *54* (4), 357-367.

97. Leon, O.; Munoz-Bonilla, A.; Soto, D.; Ramirez, J.; Marquez, Y.; Colina, M.; Fernandez-Garcia, M., Preparation of Oxidized and Grafted Chitosan Superabsorbents for Urea Delivery. *J Polym Environ* **2018,** *26*, 728-739.

98. Xiao, X.; Yu, L.; Xie, F.; Bao, X.; Liu, H.; Ji, Z.; Chen, L., One-step method to prepare starch-based superabsorbent polymerfor slow release of fertilizer. *Chemical Engineering Journal* **2017,** *309*, 607-616.

99. Wen, P.; Wu, Z.; He, Y.; Ye, B.-C.; Han, Y.; Guan, X.; Wang, J., Microwave-assisted one-step synthesis and characterization of a slow release nitrogen fertilizer with inorganic and organic composites. *RSC Advances* **2016,** *6*, 37337-37346.

100. Hill, M. R.; Konstas, K.; Andreas, S. Fertiliser Composition. 2016.

101. Wu, K.; Du, C.; Ma, F.; Shen, Y.; Liang, D.; Zhou, J., Degradation of Metal-Organic Framework Materials as Controlled-Release Fertilizers in Crop Fields. *Polymers* **2019,** *11*, 947-960.

102. Anstoetz, M.; Sharma, N.; Clark, M.; Yee, L. H., Characterization of an oxalate-phosphate-amine metal–organic framework (OPA-MOF) exhibiting properties suited for innovative applications in agriculture. *Journal of Materials Science* **2016,** *51* (20), 9239-9252.

103. Usman, K. A. S.; Buenviaje, S. C. J.; Edanol, Y. D. G.; Conato, M. T.; Payawan, L. M. J., Facile Fabrication of a Potential Slow-Release Fertilizer Based on Oxalate-Phosphate-Amine Metal-Organic Frameworks (OPA-MOFs). *Materials Science Forum* **2018,** *936*, 14-19.

104. Anstoetz, M.; Rose, T. J.; Clark, M. W.; Yee, L. H.; Raymond, C. A.; Vancov, T., Novel Applications for Oxalate-Phosphate-Amine Metal-Organic-Frameworks (OPA-MOFs)- Can an Iron-Based OPA-MOF Be Used as Slow-Release Fertilizer. *PLOS ONE* **2015,** *10*.

105. Bansiwal, A. K.; Rayalu, S. S.; Labhasetwar, N. K.; Juwarkar, A. A.; Devotta, S., Surfactant-Modified Zeolite as a Slow Release Fertilizer for Phosphorus. *J. Agric. Food Chem.* **2006,** *54*, 4773-4779.

106. Liu, C.; Wang, P.; Liu, X.; Yi, X.; Zhou, Z.; Liu, D., Multifunctional β-Cyclodextrin MOF-Derived Porous Carbon as Efficient Herbicides Adsorbent and Potassium Fertilizer. *ACS Sustainable Chem. Eng.* **2019,** *7*, 14479-14489.

107. Abdelhameed, R. M.; Abdelhameed, R. E.; Kamel, H. A., Iron-based metal-organic-frameworks as fertilizers for hydroponically grown Phaseolus vulgaris. *Materials Letters* **2019,** *237*, 72-79.

108. Forget, F., The present and past climates of planet Mars. *The European Physical Journal Conferences* **2009,** *1*, 235-248.

109. Franz, H. B.; Trainer, M. G.; Malespin, C. A.; Mahaffy, P. R.; Atreya, S. K.; Becker, R. H.; Benna, M.; Conrad, P. G.; Eigenbrode, J. L.; Freissinet, C.; Manning, H. L. K.; Prats, B. D.; Raaen, E.; Wong, M. H., Initial SAM calibration gas

experiments on Mars: Quadrupole mass spectrometer results and implications. *Planetary and Space Science* **2017,** *138*, 44-54.

110. He, C.; Davies, F. T., Jr.; Lacey, R. E., Separating the effects of hypobaria and hypoxia on lettuce: growth and gas exchange. *Physiol Plant* **2007,** *131* (2), 226-40.

111. He, C.; Davies, F. T.; Lacey, R. E., Hypobaria, hypoxia, and light affect gas exchange and the CO2 compensation and saturation points of lettuce (Lactuca sativa)This paper is one of a selection published in a Special Issue comprising papers presented at the 50th Annual Meeting of the Canadian Society of Plant Physiologists (CSPP) held at the University of Ottawa, Ontario, in June 2008. *Botany* **2009,** *87* (7), 712-721.

112. Maggi, F.; Pallud, C., Martian base agriculture: The effect of low gravity on water flow, nutrient cycles, and microbial biomass dynamics. *Advances in Space Research* **2010,** *46* (10), 1257-1265.

113. Feng, D.; Wang, K.; Wei, Z.; Chen, Y.-P.; Simon, C. M.; Arvapally, R. K.; Martin, R. L.; Bosch, M.; Liu, T.-F.; Fordham, S.; Yuan, D.; Omary, M. A.; Haranczyk, M.; Smit, B.; Zhou, H.-C., Kinetically tuned dimensional augmentation as a versatile synthetic route towards robust metal–organic frameworks. *Nature Communications* **2014,** *5*, 5723-5731.

114. Chen, Y.; Qiao, Z.; Huang, J.; Wu, H.; Xiao, J.; Xia, Q.; Xi, H.; Hu, J.; Zhou, J.; Li, Z., Unusual Moisture-Enhanced CO2 Capture within Microporous PCN-250 Frameworks. *ACS Appl Mater Interfaces* **2018,** *10* (44), 38638-38647.

115. Chen, Y.; Qiao, Z.; Wu, H.; Lv, D.; Shi, R.; Xia, Q.; Zhou, J.; Li, Z., An ethane-trapping MOF PCN-250 for highly selective adsorption of ethane over ethylene. *Chemical Engineering Science* **2018,** *175*, 110-117.

116. Fang, Y.; Banerjee, S.; Joseph, E. A.; Day, G. S.; Bosch, M.; Li, J.; Wang, Q.; Drake, H.; Ozdemir, O. K.; Ornstein, J. M.; Wang, Y.; Lu, T. B.; Zhou, H. C., Incorporating Heavy Alkanes in Metal-Organic Frameworks for Optimizing Adsorbed Natural Gas Capacity. *Chemistry* **2018,** *24* (64), 16977-16982.

117. Kirchon, A.; Li, J.; Xia, F.; Day, G. S.; Becker, B.; Chen, W.; Sue, H. J.; Fang, Y.; Zhou, H. C., Modulation versus Templating: Fine-Tuning of Hierarchally Porous PCN-250 Using Fatty Acids To Engineer Guest Adsorption. *Angew Chem Int Ed Engl* **2019,** *58* (36), 12425-12430.

118. Yuan, S.; Sun, X.; Pang, J.; Lollar, C.; Qin, J.-S.; Perry, Z.; Joseph, E.; Wang, X.; Fang, Y.; Bosch, M.; Sun, D.; Liu, D.; Zhou, H.-C., PCN-250 under Pressure: Sequential Phase Transformation and the Implications for MOF Densification. *Joule* **2017,** *1* (4), 806-815.

119. Kirchon, A.; Day, G. S.; Fang, Y.; Banerjee, S.; Ozdemir, O. K.; Zhou, H. C., Suspension Processing of Microporous Metal-Organic Frameworks: A Scalable Route to High-Quality Adsorbents. *iScience* **2018,** *5*, 30-37.

120. Li, H.; Martinez, M. R.; Perry, Z.; Zhou, H. C.; Falcaro, P.; Doblin, C.; Lim, S.; Hill, A. J.; Halstead, B.; Hill, M. R., A Robust Metal-Organic Framework for Dynamic Light-Induced Swing Adsorption of Carbon Dioxide. *Chemistry* **2016,** *22* (32), 11176-9.

121. Sarango-Ramirez, M. K.; Lim, D. W.; Kolokolov, D. I.; Khudozhitkov, A. E.; Stepanov, A. G.; Kitagawa, H., Superprotonic Conductivity in Metal-Organic Framework via Solvent-Free Coordinative Urea Insertion. *J Am Chem Soc* **2020,** *142* (15), 6861-6865.

122. Permyakova, A.; Wang, S.; Courbon, E.; Nouar, F.; Heymans, N.; D'Ans, P.; Barrier, N.; Billemont, P.; De Weireld, G.; Steunou, N.; Frère, M.; Serre, C., Design of salt–metal organic framework composites for seasonal heat storage applications. *Journal of Materials Chemistry A* **2017,** *5* (25), 12889-12898.

123. Seth, S.; Vaid, T. P.; Matzger, A. J., Salt loading in MOFs: solvent-free and solvent-assisted loading of NH4NO3 and LiNO3 in UiO-66. *Dalton Trans* **2019,** *48* (35), 13483-13490.